
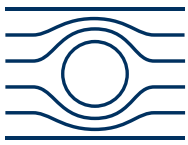


Technische Universität München

Walther-Meissner-Institut

Bayerische Akademie der Wissenschaften

Unidirectional Spin Wave Propagation in Magnetic Nanograting/Thin Film Heterostructures

Master's thesis

Christian Mang

Supervisor: Prof. Dr. Rudolf Gross

Advisor: Dr. Stephan Geprägs, Monika Scheufele

Garching – April 14, 2023

Contents

Chapter 1

Motivation

Unidirectional transport of information is an essential tool in various fields including optics, microwave technology, and logic devices [1–3]. In optics, the non-reciprocal behavior of an optical diode can be used in a resonator such as a laser cavity to transmit light out of the resonator while blocking reflected light from reentering the system [4]. In microwave technology, the capability to inhibit signal flow in one direction while enabling it in the opposite direction is essential in applications such as radar or, more recently, quantum technology, where the quantum state of a qubit needs to be protected from outside noise. For microwave applications, the non-reciprocity is often based on the gyrotropic nature of ferrite materials, where an anisotropic permittivity results in a difference in phase velocity depending on the propagation direction of the microwave [5]. With dimensions in the range of centimeters, these devices are comparatively large and costly to fabricate [6]. Therefore, new approaches for unidirectional transport that allow for miniaturization and on-chip integration of non-reciprocal devices such as circulators and isolators are crucial to enable scaling-up quantum computers.

A promising field for future non-reciprocal devices involves the field of magnonics, where collective excitations in magnetically ordered materials, called spin waves (SWs), are used to transport information. Since SWs propagate without the motion of electrons, they allow for the implementation of logic devices without the inherent drawbacks of modern electronics such as dissipation of energy due to Joule heating induced by charge transport [7]. Non-reciprocity in a magnonic device can be realized by exciting unidirectional SWs. Several methods to generate unidirectional SWs have been demonstrated in the past. For instance, the dynamics of magnetostatic surface SWs in thick magnetic films or the interfacial Dzyaloshinskii–Moriya interaction (iDMI) in magnetic multilayer systems can both lead to the unidirectional propagation of SWs [8–11]. In the former case, SWs propagating in opposite directions are located at opposite surfaces of the magnetic film. Their amplitudes decay exponentially from the respective surface along the film thickness direction. The latter approach is characterized by an asymmetric dispersion relation induced by iDMI, which leads to the non-reciprocal propagation of SWs in the frequency domain.

This work focuses on the approach of exciting unidirectional SWs through dipolar coupling to a local magnetic transducer proposed in Ref. [12]. Thereby, an array of magnetic nanowires, a so called nanograting, is used to induce non-reciprocal SW modes in the underlying thin film. The propagation direction of the unidirectional SWs can then

be controlled by the direction of the thin film and nanowire magnetizations, i.e., by the external magnetic field. This method is especially interesting, as it should enable non-reciprocal excitation of short-wavelength SWs with high group velocities, which is beneficial for possible applications in magnonic logic devices with fast switching times [13, 14]. To this end, different material systems for the realization of SW propagation devices with magnetic nanogratings are explored in this work, including an all-metallic system that provides good compatibility with silicon based technology.
This thesis starts with the discussion of the theoretical concepts in Ch. 2 including ferromagnetic resonance (FMR), its experimental implementation and the necessary data processing of the obtained measurement results. In addition, the basics of SWs are covered together with the experimental setup used to excite and detect SWs. Lastly, various methods to excite unidirectional SWs are discussed with a focus on excitation of unidirectional SWs with a magnetic nanograting.
Chapter 3 details the optimization of the fabrication process. The magnetic materials used for the fabrication of SW propagation devices are optimized for their structural and magnetic properties. To this end, optimized multilayer stacks for the fabrication of $Co_{25}Fe_{75}$ (CoFe) and $Ni_{75}Fe_{25}$ (Py) are presented. Furthermore, an optimal resist recipe for the fabrication of magnetic nanogratings via electron-beam lithography is developed and discussed. In addition, the magnetization dynamics of the optimized CoFe and Py nanogratings are investigated by broadband FMR measurements.
In Chs. 4 and 5, SW propagation devices are studied with focus on unidirectional transport. First, devices with $Y_3Fe_5O_{12}$ (YIG) as the SW medium and CoFe nanogratings as the local magnetic transducer are discussed in Ch. 4. The SW propagation in all-metallic devices consisting of CoFe waveguides and Py nanogratings is then thematically covered in Ch. 5. The work is concluded with a summary and an outlook in Ch. 6.

Chapter 2

Theory

This chapter covers the theoretical concepts necessary to describe the experimental findings in Chs. 3, 4 and 5. First, the macrospin model is introduced in Sec. 2.1 and the basics of ferromagnetic resonance (FMR) are described in Sec. 2.2. Then the experimental implementation of FMR spectroscopy and the necessary data processing are covered in Secs. 2.3 and 2.4. Furthermore, key aspects of spin waves (SWs) and SW propagation measurements are outlined in Sec. 2.5. In Sec. 2.6 different mechanisms that lead to unidirectional propagation of SWs are discussed. For this, SW unidirectionality in thick magnetic films, thin magnetic films and chiral pumping by local magnetic transducers is described.

2.1 Macrospin model of a ferromagnetic solid

The microscopic magnetic moments $\boldsymbol{\mu}_i$ in the volume V of a ferromagnetic solid, which are ferromagnetically exchange coupled by Heisenberg interaction, can be collectively described by the measurable macroscopic quantity of the magnetization $\mathbf{M}$:

$$\mathbf{M} = \frac{1}{V} \sum_{\boldsymbol{\mu}_i \in V} \boldsymbol{\mu}_\mathbf{i}, \tag{2.1}$$

where the length of $\mathbf{M}$ corresponds to the saturation magnetization M_S of the ferromagnet. The direction of $\mathbf{M}$ is influenced by the external magnetic field $\mathbf{H}_\mathrm{ext}$ and internal fields, such as the demagnetization field $\mathbf{H}_\mathrm{de}$ or the anisotropy field $\mathbf{H}_\mathrm{ani}$ (a detailed discussion of the internal fields is found in textbooks [15, 16]). The demagnetization field is related to the magnetization via the demagnetization tensor $\hat{\mathbf{N}}$. To summarize these contributions and assuming a spatially homogeneous magnetization with parallel magnetic moments, an effective magnetic field $\mathbf{H}_\mathrm{eff}$ can be defined as [17]

$$\mathbf{H}_\mathrm{eff} = \mathbf{H}_\mathrm{ext} + \mathbf{H}_\mathrm{de} + \mathbf{H}_\mathrm{ani} = \mathbf{H}_\mathrm{ext} - \hat{\mathbf{N}}\mathbf{M} + \mathbf{H}_\mathrm{ani}. \tag{2.2}$$

In thermal equilibrium with external magnetic fields larger than the saturation field, the magnetization is aligned with $\mathbf{H}_\mathrm{eff}$. By perturbing the system, a finite angle between the magnetization $\mathbf{M}$ and the effective magnetic field $\mathbf{H}_\mathrm{eff}$ can be introduced. This leads to a torque $\mathbf{T}$ acting on the magnetization $\mathbf{M}$, which is equal to the time derivative of the

angular momentum $\mathbf{J}$ and is given by

$$\mathbf{T} = \frac{\mathrm{d}\mathbf{J}}{\mathrm{d}t} = -V\mu_0\mathbf{M} \times \mathbf{H}_{\mathrm{eff}}. \tag{2.3}$$

Furthermore, the magnetization $\mathbf{M}$ can be expressed in terms of its angular momentum $\mathbf{J}$ by

$$\mathbf{M} = -\gamma\frac{\mathbf{J}}{V}, \tag{2.4}$$

where $\gamma = g\mu_{\mathrm{B}}\hbar$ is the gyromagnetic ratio, g the Landé-factor and μ_{B} the Bohr magneton. Combining Eqs. (2.3) and (2.4) leads to the Landau-Lifshitz equation [18]

$$\frac{\mathrm{d}\mathbf{M}}{\mathrm{d}t} = -\gamma\mu_0\mathbf{M} \times \mathbf{H}_{\mathrm{eff}}, \tag{2.5}$$

which describes the precession of magnetization around the effective magnetic field with the frequency

$$\omega_L = \gamma\mu_0|\mathbf{H}_{\mathrm{eff}}|. \tag{2.6}$$

In reality, a relaxation of the precession motion is observed, as various loss channels such as the induction of eddy currents are present [19]. Therefore, a phenomenological damping term was introduced by Gilbert leading to the Landau-Lifshitz-Gilbert (LLG) equation [20]

$$\frac{\mathrm{d}\mathbf{M}}{\mathrm{d}t} = -\gamma\mu_0\mathbf{M} \times \mathbf{H}_{\mathrm{eff}} + \frac{\alpha}{M_{\mathrm{S}}}\mathbf{M} \times \frac{\mathrm{d}\mathbf{M}}{\mathrm{d}t}, \tag{2.7}$$

where α is the Gilbert damping parameter. The second term in the LLG equation leads to an alignment of the magnetization vector to the equilibrium position parallel to the effective magnetic field after a finite time interval. Equation (2.7) is equivalent to the description of a damped harmonic oscillator. By introducing a periodically oscillating magnetic field perpendicular to the effective field in the next section, a resonance condition can be deduced just as for the driven harmonic oscillator in classical mechanics.

2.2 Ferromagnetic resonance

An oscillating driving field $\mathbf{h}_{\mathrm{rf}}$ directed perpendicular to $\mathbf{H}_{\mathrm{eff}}$ is introduced to the system. As shown in Fig. 2.2.1 (a), the driving field leads to an additional torque acting on the magnetization that counteracts the damping torque. By matching the frequency of $\mathbf{h}_{\mathrm{rf}}$ to the precession frequency of the magnetization, the torque generated by $\mathbf{h}_{\mathrm{rf}}$ fully compensates the damping torque, enabling a sustained precession motion of the magnetization around the effective field. In the following, the resonance condition is derived. The effective magnetic field is directed along the z-axis of the coordinate system and the oscillating driving field $\mathbf{h}_{\mathrm{rf}}$ lies in the x-y-plane. An ellipsoidal sample geometry with the symmetry axes directed along the coordinate axes is assumed, which eliminates all off-diagonal elements of the demagnetization tensor $\hat{\mathbf{N}}$. Furthermore, the magnetocrystalline anisotropy is neglected here for didactic reasons. The oscillating driving field is

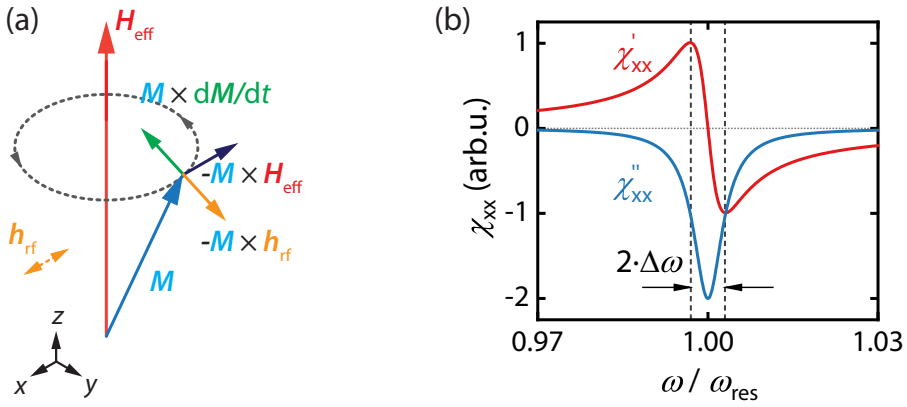

Figure 2.2.1: (a) Schematic of the magnetization vector $\mathbf{M}$ precessing around the effective magnetic field $\mathbf{H}_{\text{eff}}$. The driving field $\mathbf{h}_{\text{rf}}$ generates an additional torque compensating the damping torque $\mathbf{M} \times \mathrm{d}\mathbf{M}/\mathrm{dt}$. (b) Real part χ'_{xx} (red line) and imaginary part χ''_{xx} (blue line) of the Polder susceptibility in Eq. (2.11). Taken from Ref. [17].

added to the effective field leading to

$$\mathbf{H}_{\text{eff}} = \mathbf{H}_{\text{ext}} + \mathbf{H}_{\text{de}} + \mathbf{h}_{\text{rf}}(\mathbf{t}) = \mathbf{H}_{\text{ext}} - \hat{\mathbf{N}}\mathbf{M} + \mathbf{h}_{\text{rf}}(\mathbf{t}) = \begin{bmatrix} -N_{xx}M_x(t) \\ -N_{yy}M_y(t) \\ H_{\text{ext}} - N_{zz}M_{\text{S}} \end{bmatrix} + \begin{bmatrix} h_{\text{rf},x}(t) \\ h_{\text{rf},y}(t) \\ 0 \end{bmatrix}, \quad (2.8)$$

where additional anisotropy contributions besides the shape anisotropy are neglected. In the linear response regime, where $|\mathbf{h}_{\text{rf}}| \ll |\mathbf{H}_0|$ and $M_x, M_y \ll M_z$, the following ansatz for the time dependency of the driving field and the x- and y-component of the magnetization vector is used:

$$\begin{aligned} \mathbf{h}_{\text{rf},i}(t) &= h_{\text{rf},i} \cdot e^{i\omega t} \\ \mathbf{M}_i(t) &= M_i \cdot e^{i\omega t} \end{aligned} \qquad \text{with } i \in \{x, y\}. \quad (2.9)$$

Inserting Eqs. (2.8) and (2.9) into the LLG equation yields a system of two differential equations for the time dependent x- and y-coordinate of the magnetization vector, that can be written in matrix form:

$$\begin{bmatrix} h_{\text{rf},x} \\ h_{\text{rf},y} \end{bmatrix} = \hat{\chi}^{-1} \begin{bmatrix} M_x \\ M_y \end{bmatrix}. \quad (2.10)$$

By inverting the matrix $\hat{\chi}^{-1}$ the Polder susceptibility [21]

$$\hat{\chi} = \frac{\mu_0 M_{\text{S}}}{\text{Det}(\hat{A})}\hat{A} = \frac{\mu_0 M_{\text{S}}}{\text{Det}} \begin{bmatrix} A_{11} & -\frac{i\omega}{\gamma\mu_0} \\ \frac{i\omega}{\gamma\mu_0} & A_{22} \end{bmatrix} \quad (2.11)$$

is obtained, where the diagonal tensor entries are given by

$$\begin{aligned} A_{11} &= H_{\text{ext}} + (N_{xx} - N_{zz})M_{\text{S}} + \frac{i\omega}{\gamma\mu_0}, \\ A_{22} &= H_{\text{ext}} + (N_{yy} - N_{zz})M_{\text{S}} + \frac{i\omega}{\gamma\mu_0}. \end{aligned} \tag{2.12}$$

The susceptibility tensor determines the linear response of the magnetization to the small external perturbation $\mathbf{h}_{\text{rf}}$. The typical line shape of the real χ' and imaginary χ'' part of the first diagonal entry is shown in Fig. 2.2.1 (b) with $N_{xx} = N_{yy} = 0$ and $N_{zz} = 1$. The real part of the susceptibility χ' describes the dissipation of the system with the typical dispersive line shape, while the imaginary part χ'' follows a Lorentzian characterizing the absorption of the system.
The resonance condition is fulfilled for $\text{Det}(\hat{\chi}) = 0$. Solving this condition for ω and taking the real part of the solution returns the resonance frequency, which is known as the Kittel equation [22]

$$\omega_{\text{res}} = \gamma\mu_0\sqrt{[H_{\text{ext}} + (N_{xx} - N_{zz})M_{\text{S}}] \cdot [H_{\text{ext}} + (N_{yy} - N_{zz})M_{\text{S}}]}. \tag{2.13}$$

Depending on the demagnetization coefficients N_{ii} ($i \in \{x, y, z\}$) and therefore the geometry of the sample, the Kittel equation can be further simplified in some special cases. In this work, mostly thin film samples with a thickness of a few nanometers are studied, where the Kittel equation takes the following form:

- **Thin film, in-plane** (IP) geometry: The external magnetic field lies in the sample plane of the thin film and the z-direction points perpendicular to the sample plane. As the thickness of the film is much smaller than its lateral dimensions, the demagnetization coefficients are approx. $N_{xx} = 1$, $N_{yy} = N_{zz} = 0$. The Kittel equation then simplifies to

$$\omega_{\text{res}} = \gamma\mu_0\sqrt{H_{\text{ext}}(H_{\text{ext}} + M_{\text{S}})}. \tag{2.14}$$

- **Thin film, out-of-plane** (OOP) geometry: Here, the external magnetic field is directed perpendicular to the sample plane of the thin film. The demagnetization coefficients then are approximated by $N_{xx} = N_{yy} = 0$ and $N_{zz} = 1$. Therefore the Kittel equation becomes

$$\omega_{\text{res}} = \gamma\mu_0(H_{\text{ext}} - M_{\text{S}}). \tag{2.15}$$

Note that the equations of the resonance frequencies are modified when taking anisotropy contributions into account [23]. While the Kittel equation is obtained from the real part of the resonance condition, the linewidth of the resonance is determined by the imaginary part of the solution. The full-width-half-maximum (FWHM) of the resonance in both

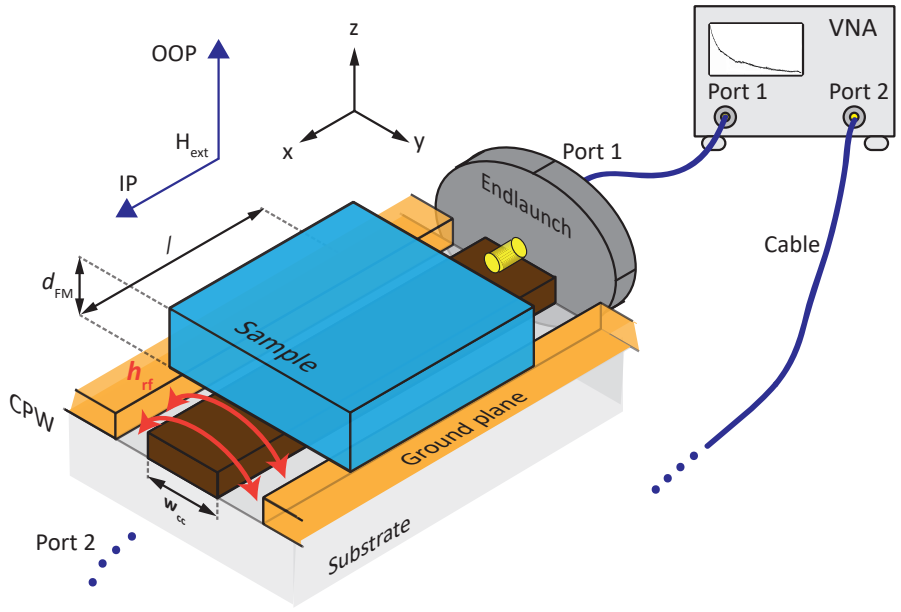

Figure 2.3.1: Sample mounted on a coplanar waveguide (CPW). The endlaunches of the CPW are connected to the ports of a vector network analyzer (VNA) via microwave cables. The AC signal from the VNA generates the driving field $\mathbf{h}_{\mathrm{rf}}$ around the center conductor of the CPW. The external magnetic field stemming from the electromagnet not depicted here, is either directed in the sample plane (IP) or perpendicular to the sample plane (OOP). Taken from [25].

the IP and OOP geometry is given by

$$\Delta H(\omega) = 2\frac{\alpha\omega}{\mu_0\gamma}. \tag{2.16}$$

Therefore, by determining the linewidth in relation to the resonance frequency, the phenomenological damping parameter α of the sample can be obtained. In experiments, a deviation of the linewidth function $\Delta H(\omega)$ from this relation might be observed. This can be related to long-range magnetic inhomogeneities in the sample, setup misalignments and two-magnon scattering processes [24]. To take these effects into account, Eq. (2.16) is modified by including the inhomogeneous line width broadening ΔH_{inh}:

$$\Delta H(\omega) = \Delta H_{\mathrm{inh}} + 2\frac{\alpha\omega}{\mu_0\gamma}. \tag{2.17}$$

The next section focuses on the technical implementation of the FMR experiments performed in this work.

2.3 Broadband ferromagnetic resonance spectroscopy

The dynamic magnetic susceptiblity of the samples is measured by broadband ferromagnetic resonance spectroscopy at room temperature. The experimental setup consist of a vector network analyzer (VNA), a coplanar waveguide (CPW) and an electromagnet. A schematic depiction of the setup is shown in Fig. 2.3.1. The electromagnet is used to generate a homogeneous external magnetic field either in IP- or OOP-direction. The sample is placed face-down on the center conductor (CC) of a CPW. The endlaunches of the CPW are connected to the ports of a VNA with microwave coaxial cables. The VNA generates an alternating current that induces the driving field $\mathbf{h}_{\mathrm{rf}}$ around the CC of the CPW. Subsequently, the microwave energy absorbed by the sample is recorded as a function of the microwave frequency and external magnetic field with the VNA. When the resonance condition is met, the sample absorbs power from the electromagnetic field of the CC, resulting in a dip in the transmission signal. In the following, the theoretical description of the data obtained from the bbFMR measurements is outlined. A more detailed discussion is found in Ref. [26].
The coordinate system is defined as shown in Fig. 2.3.1, with the CPW in the x-y-plane and the center of the signal line at $y = 0$. The driving field induced by a microwave current I flowing along the x-direction in the CC with the width w_{cc} is given by the Karlqvist equations [27]

$$\begin{aligned} h_y(y,z) &= \frac{1}{\pi}\frac{I}{2w_{\mathrm{cc}}}\left(\arctan\left(\frac{y+w_{\mathrm{cc}}/2}{z}\right)-\arctan\left(\frac{y-w_{\mathrm{cc}}/2}{z}\right)\right) \\ h_z(y,z) &= \frac{1}{2\pi}\frac{I}{2w_{\mathrm{cc}}}\ln\left(\frac{(y+-w_{\mathrm{cc}}/2)^2+z^2}{(y-w_{\mathrm{cc}}/2)^2+z^2}\right). \end{aligned} \tag{2.18}$$

The coupling between the magnetic field of the CPW and the magnetization of the sample results in changes of the magnetic flux Φ. According to Faraday's law of induction, these changes in magnetic flux induce a detectable voltage in the CPW given by

$$V_{\mathrm{ind}} = -\frac{\partial\Phi}{\partial t}. \tag{2.19}$$

The discussion can be restricted to the dynamic part of the flux, which depends on the local response of the sample to the driving field $\mathbf{h}(y,z)$ and is therefore related to the susceptibility $\hat{\chi}$ by

$$\begin{aligned} \Phi_{\mathrm{dyn}} &= \frac{\mu_0}{I}\iiint_V \mathbf{h}(y,z)\cdot\hat{\chi}\cdot\,\mathbf{h}(y,z)\,\mathrm{d}x\,\mathrm{d}y\,\mathrm{d}z = \\ &= \frac{\mu_0}{I}\iiint_V \chi_{yy}h_y^2+(\chi_{yz}+\chi_{zy})h_yh_z+\chi_{zz}h_z^2\,\mathrm{d}x\,\mathrm{d}y\,\mathrm{d}z. \end{aligned} \tag{2.20}$$

For samples which are symmetrical in y-direction, the middle term in the integral cancels out. Moreover, since the thickness t_{FM} of the ferromagnetic layer of the thin film samples studied in this work can be considered to be much smaller than the width w_{cc} of the CC,

the components of the driving field are replaced with $h_y(y,0)$ and $h_z(y,0)$, respectively. In addition, the width of the sample b is assumed to be much larger than w_{cc}, which allows for the integral boundaries in y-direction to be considered infinite. With these approximations the dynamic magnetic flux reduces to

$$\Phi_{\mathrm{dyn}} = \mu_0 I \frac{l \cdot t_{\mathrm{FM}}}{4 w_{\mathrm{cc}}} (\chi_{yy} + \chi_{zz}), \tag{2.21}$$

where l is the length of the sample in x-direction. The magnetic flux is linked to the inductance L of the system, which solely depends on geometric parameters and the magnetic susceptibility of the sample:

$$L = \frac{\Phi_{\mathrm{dyn}}}{I} = \mu_0 \frac{l \cdot t_{\mathrm{FM}}}{4 w_{\mathrm{cc}}} (\chi_{yy} + \chi_{zz}). \tag{2.22}$$

The inductance of the CPW with the mounted sample can in turn be related to the measured quantity of the experiment. The VNA measures the magnitude and phase of the voltage at both ports and calculates the complex transmission parameter S_{21} with

$$S_{21} = \frac{V_2}{V_1} = \frac{|V_2|}{|V_1|} e^{i\phi}, \tag{2.23}$$

where ϕ is the phase difference between the microwave signal at port 1 and port 2. As discussed above, the energy absorbed by the sample changes when the resonance condition is met. Also, the transmission through the microwave setup itself is frequency dependent, leading to the microwave background S_{21}^0. Therefore, the contribution ΔS_{21} to the transmission associated with the sample in a fully impedance-matched circuit is given by

$$\Delta S_{21} = \frac{S_{21} - S_{21}^0}{S_{21}^0}. \tag{2.24}$$

Here, it is assumed that the sample does not have a significant influence on the impedance of the system when placed on the CPW and thus only adds an inductive contribution. The inductance L of the sample and the impedance Z_0 of the empty CPW are described with a voltage divider model where both are connected in series. Therefore, ΔS_{21} can be expressed by

$$\Delta S_{21} = \frac{1}{2} \frac{-i\omega L}{Z_0 - i\omega L} \approx -\frac{i\omega L}{2 Z_0}, \tag{2.25}$$

with the approximation $Z_0 \gg \omega L$. The factor 1/2 is due to the fact that the voltage is measured between the CC and the ground plane of the CPW and not between port 1 and 2 of the VNA. The precise model for the amplitude of ΔS_{21} requires a lengthy derivation (cf. Ref. [26]) and is therefore omitted here. A more trivial expression for the S_{21} parameter can be obtained by inserting Eq. (2.25) into Eq. (2.24) and considering that the inductance of the sample is proportional to the Polder susceptibility $L \propto \chi(\omega, H_{\mathrm{ext}})$.

This leads to

$$S_{21} = S_{21}^0(\omega) + S_{21}^0(\omega)\Delta S_{21} = S_{21}^0(\omega) - iAe^{i\phi}\chi(\omega, H_{ext}) \tag{2.26}$$

with the real-valued amplitude A, that includes all constants and geometry parameters, and the phase ϕ stemming from the microwave background transmission $S_{21}^0(\omega)$. Depending on the geometry of the measurement, the susceptibility is simply the matrix element $\chi_{yy}(\omega, H_{\text{ext}})$ in the OOP-geometry, $\chi(\omega, H_{ext}) = \chi_{xx}(\omega, H_{\text{ext}})$ in the IP-geometry with the magnetic field perpendicular to the CC of the CPW, and $\chi(\omega, H_{\text{ext}}) = 1/2(\chi_{xx}(\omega, H_{\text{ext}}) + \chi_{yy}(\omega, H_{\text{ext}}))$ in the IP-geometry with the magnetic field parallel to the CC.
For the resonance measurement two different experimental approaches can be applied. Either the external magnetic field $\mathbf{H}_{\text{ext}}$ is held at a fixed magnitude while sweeping the microwave frequency f or the excitation frequency is fixed and the external magnetic field is varied. In this thesis only frequency-swept bbFMR measurements are performed. The following section will discuss how the raw data obtained from these measurements is processed to remove the microwave background.

2.4 Data processing of broadband ferromagnetic resonance measurements

To extract important material parameters from the bbFMR measurements, the raw data of S_{21} is fitted with a complex Lorentzian function using a labview routine. Thereby, field slices at a constant frequency around the resonance field are taken from the raw data and fitted with the function

$$\begin{aligned} S_{21}(H_{\text{ext}})|_f &= C_0 + C_1 \cdot H_{\text{ext}} - iAe^{i\phi} \cdot \chi(\omega, H_{\text{ext}}) = C_0 + C_1 \cdot H_{\text{ext}} \\ &-iAe^{i\phi} \cdot \frac{\left(H_{\text{ext}} + \frac{\left(\frac{\omega}{\mu_0\gamma}\right)^2 - H_{\text{res}}^2}{H_{\text{res}}} - i\frac{\Delta H_{\text{FWHM}}}{2}\right)}{\left(H_{\text{ext}} + \frac{\left(\frac{\omega}{\mu_0\gamma}\right)^2 - H_{\text{res}}^2}{H_{\text{res}}} - i\frac{\Delta H_{\text{FWHM}}}{2}\right)\left(H_{\text{ext}} - i\frac{\Delta H_{\text{FWHM}}}{2}\right) - \left(\frac{\omega}{\mu_0\gamma}\right)^2} \end{aligned} \tag{2.27}$$

which is derived in Ref. [26]. Here, H_{res} and ΔH_{FWHM} denote the resonance field and resonance line width, respectively. In Eq. (2.27) the microwave background is modeled by $S_{21}^0 = C_0 + C_1 \cdot H_{\text{ext}}$, with the complex offset C_0 and slope C_1 [28]. For the IP- and OOP-geometry the general fitting formula stays the same, but the amplitude A needs to be adjusted. In Sec. 3.1 the fitting procedure is performed in detail and exemplary plots of the raw data with the respective fits are provided.
The measurements of the transmission parameter $S_{21}(f, H_{\text{ext}})$ are also visualized as colormaps in this work. Thereby the signal associated with the sample needs to be isolated from the dominant microwave background. The frequency dependent microwave background can be mostly eliminated by the so-called "derivative-divide" method. For this

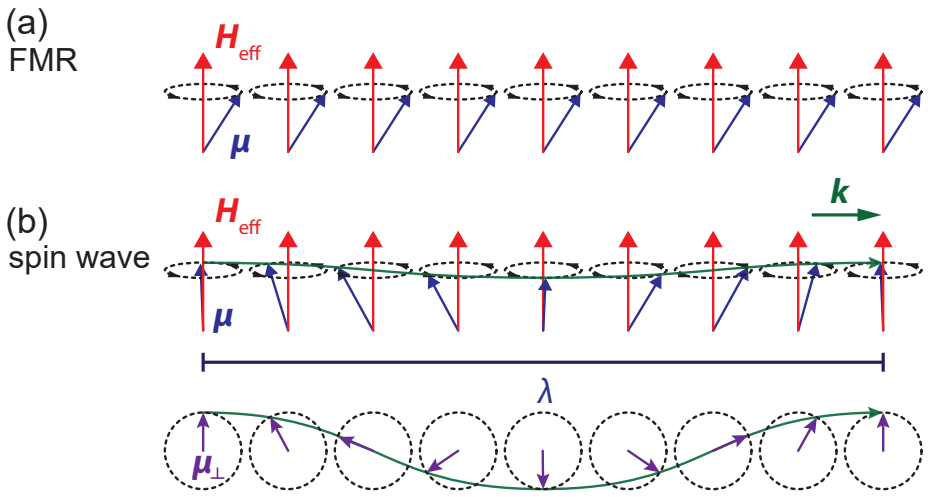

Figure 2.5.1: (a) The uniform precession motion of the magnetic moments $\boldsymbol{\mu}$ around the effective magnetic field $\mathbf{H}_{\text{eff}}$ driven in FMR. (b) Excitation of a propagating spin wave with wavevector $\mathbf{k}$, where neighboring magnetic moments precess with a relative phase difference around the effective field. The top-down view in the lowest panel shows the definition of a full wavelength λ defined by the component $\boldsymbol{\mu}_{\perp}$. Taken from Ref. [17].

background correction method the numerical derivative of the complex transmission parameter S_{21} with respect to the external magnetic field H_{ext} is evaluated [29]:

$$\partial_{\text{D}} S_{21}/\partial H_{\text{ext}} = \frac{S_{21}(\omega, H_{\text{ext}} + \Delta H) - S_{21}(\omega, H_{\text{ext}} - \Delta H)}{S_{21}\Delta H}, \tag{2.28}$$

where ΔH is the finite magnetic field step size. This post processing step alleviates the need of microwave network calibration representing a tedious task, since it is dependent on the repeatability of microwave connections and does not account for a temporal background drift.

2.5 Spin waves in ferromagnetic solids

In Sec. 2.2 the uniform precession motion of the magnetic moments in a ferromagnetic solid state was discussed in the framework of Fig. 2.5.1 (a). Hereby, neighboring magnetic moments exhibit no relative phase difference, which is equivalent to a wave with wavevector $k \to 0$ and wavelength $\lambda \to \infty$.
At finite wavevector, a relative phase difference to the precession motion of neighboring spins has to be taken into account as shown in Fig. 2.5.1 (b), creating a propagating wave that can transport information [7, 30]. The energy of these so called spin waves (SWs), or magnons in the quantized picture, is determined by long-range dipole-dipole interactions and the short-range exchange interaction between the spins [31].

The exchange interaction adds an effective exchange field

$$\mu_0 H_{\mathrm{ex}} = \frac{2A_{\mathrm{ex}}}{M_{\mathrm{S}}} k^2 \tag{2.29}$$

with the exchange stiffness constant A_{ex} to the effective field H_{eff}. This contribution is especially important at larger k-values and is isotropic in contrast to the dipolar interactions. In an in-plane (IP) magnetized thin film of the thickness t_{FM} with $k \cdot t_{\mathrm{FM}} \ll 1$, the dynamic dipolar fields of a SW are given by [32]

$$\begin{aligned} H_x^{\mathrm{dip}} &= M_{\mathrm{S}} \left(1 - \frac{1 - e^{-kt_{\mathrm{FM}}}}{kt_{\mathrm{FM}}}\right) \sin^2(\phi), \\ H_y^{\mathrm{dip}} &= M_{\mathrm{S}} \frac{1 - e^{-kt_{\mathrm{FM}}}}{kt_{\mathrm{FM}}} \end{aligned} \tag{2.30}$$

with the magnetization direction pointing along the z-axis, the surface normal along the y-axis and the x-axis in the sample plane perpendicular to the net magnetization vector. The angle ϕ indicates the IP angle between the $\mathbf{k}$-vector and the magnetization $\mathbf{M}$. This thesis studies SWs propagating parallel to the surface of IP magnetized thin films with the $\mathbf{k}$-vector directed perpendicular to the magnetization direction ($\mathbf{k} \perp \mathbf{M}$, $\phi = 90°$), which is called Damon-Eshbach (DE) geometry. For $\phi = 0$, the SWs propagate parallel to the magnetization direction ($\mathbf{k} \parallel \mathbf{M}$) which are so called backward volume SWs and are, as the name suggests, volume modes. Both special cases of the IP modes are depicted in Fig. 2.5.2 (a). The resonance frequency for IP SWs was defined by Kalinikos and Slavin [32] by

$$\omega = \gamma\mu_0 \sqrt{\left(H_{\mathrm{ext}} + H_{\mathrm{ex}} + H_x^{\mathrm{dip}}\right)\left(H_{\mathrm{ext}} + H_{\mathrm{ex}} + H_y^{\mathrm{dip}}\right)}. \tag{2.31}$$

As in Sec. 2.2, the derivation of this formula assumes an ellipsoidal sample geometry. In the limit of $k \to 0$, the dipolar fields are given by $H_x^{\mathrm{dip}} = M_{\mathrm{S}}$ and $H_y^{\mathrm{dip}} = 0$, therefore, the Kalinikos-Slavin equation becomes $\omega = \gamma\mu_0 \sqrt{H_{\mathrm{ext}} \cdot (H_{\mathrm{ext}} + M_{\mathrm{S}})}$, which is equal to the Kittel equation of the FMR. In the opposite limit of large $\mathbf{k}$-vectors and small wavelengths, the dipolar fields approach zero and the dispersion relation becomes $\omega = \gamma\mu_0(H_{\mathrm{ext}} + H_{\mathrm{ex}})$, which is proportional to k^2 and thus parabolic. The SWs in this regime with wavelengths well below 1 µm are governed by the exchange interaction and are therefore called exchange spin waves [7]. On the other hand, dipolar SWs have wavelengths in the micrometer regime and their dispersion is dominated by their dipolar fields. SWs with a dispersion strongly affected by both interaction are referred to as dipolar-exchange SWs.

Figure 2.5.2 (b) shows the dispersion relation calculated with Eq. (2.31) at a fixed external magnetic field of $\mu_0 H_{\mathrm{ext}} = 50\,\mathrm{mT}$ for 30 nm thick $Co_{25}Fe_{75}$ with $A = 2.6 \times 10^{-11}\,\mathrm{J/m}$, $\mu_0 M_{\mathrm{S}} = 2.36\,\mathrm{T}$ and $\alpha = 0.003$ [17]. The backward volume mode, depicted in green, exhibits a negative group velocity ($v_g = \partial\omega(k)/\partial k$) at small $\mathbf{k}$-vectors and transitions into the exchange dominated parabolic behavior at larger $\mathbf{k}$-vectors. The DE mode (orange) is located at higher frequencies and posses a larger group velocity for smaller k-values.

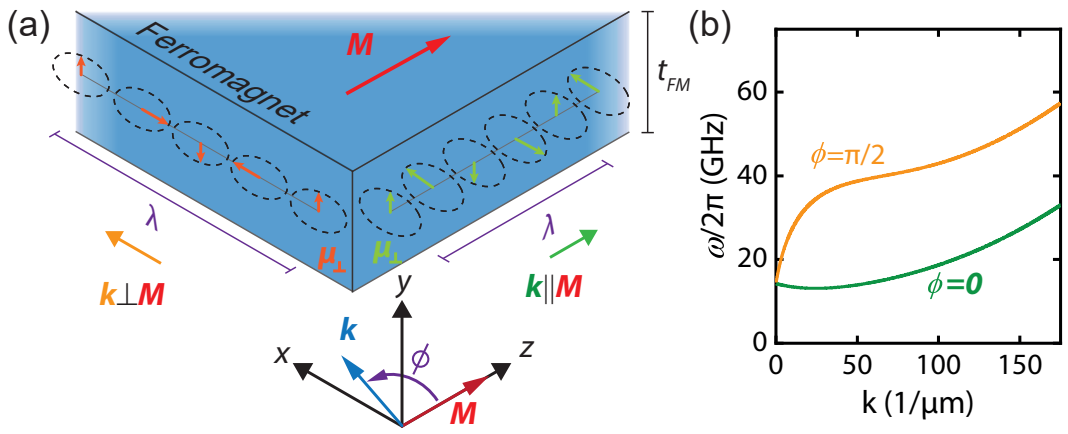

Figure 2.5.2: (a) Damon-Eshbach mode ($\mathbf{k} \perp \mathbf{M}$, $\phi = 90°$) and backward volume mode ($\mathbf{k} \parallel \mathbf{M}$, $\phi = 0$) propagating in a ferromagnet with thickness t_{FM} and magnetization $\mathbf{M}$ directed along the z-axis. The definition of the angle ϕ as the IP angle between the $\mathbf{k}$-vector and the magnetization $\mathbf{M}$ is shown in the coordinate system. (b) Dispersion relation for $\phi = 0$ and $\phi = \pi/2$ obtained from Eq. (2.31) for 30 nm thick $Co_{25}Fe_{75}$ at a fixed external mangetic field of $\mu_0 H_{\mathrm{ext}} = 50\,\mathrm{mT}$. Adapted from Ref. [17].

In Fig. 2.5.3, the experimental setup used in this thesis to excite and detect SWs is schematically depicted. The external magnetic field $\mathbf{H}_{\mathrm{ext}}$ aligns the magnetization of the sample in the plane perpendicular to the SW propagation direction to excite Damon-Eshbach type SWs. Two metallic antennas are structured on top of the sample. One end of each antenna is connected to the port of a VNA while the other end is grounded. This is done by wire bonding the sample to a microwave CPW with an interrupted signal line. The VNA generates a microwave rf-signal with a certain frequency and power, that induces an oscillating magnetic field around the antennas. Through the coupling of the magnetic moments to the oscillating driving field of one antenna a SW can be excited. The SW can propagate within the sample to the opposing antenna, where it induces a measurable current in the antenna and can therefore be detected as an electrical signal. The VNA measures the four entries of the complex scattering matrix $S_{ij} = \frac{|V_i|}{|V_j|} e^{i(\phi_i - \phi_j)}$ with $i, j \in \{1, 2\}$. The diagonal entries measure the complex voltage ratio between the incident and reflected microwave at each port while the off-diagonal elements represent the transmission of the signal through the device from port 1 to port 2 (S_{21}) and vice versa (S_{12}).

2.6 Unidirectional spin waves in ferromagnetic solids

Unidirectional transport of SWs can manifest itself in a difference in amplitude, frequency or group velocity for SWs propagating in opposite directions. This section introduces various mechanisms that can lead to this non-reciprocal behavior.

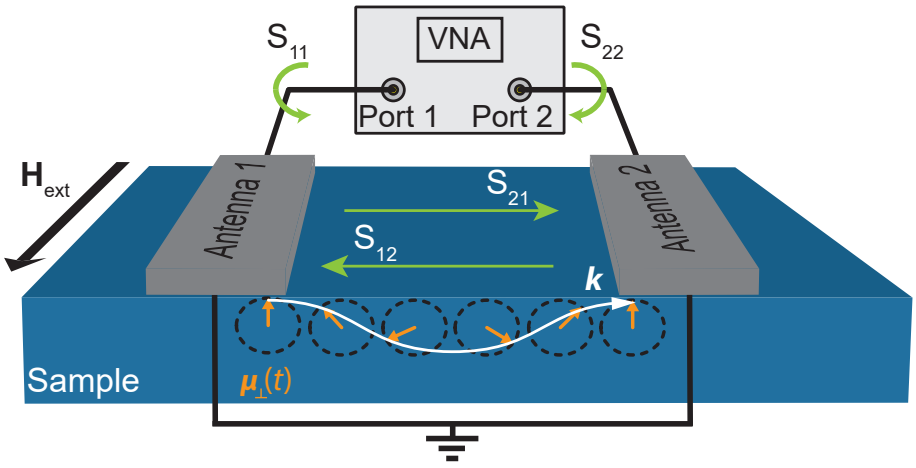

Figure 2.5.3: Schematic depiction of a spin wave propagation device with two antennas connected to a vector network analyzer (VNA). The external magnetic field $\mathbf{H}_{\text{ext}}$ forces the magnetization of the sample in the plane perpendicular to the SW propagation direction. The VNA sends a microwave signal to one of the antennas and measures the response by recording the four S-parameters. The antennas structured on top of the device generate an oscillating magnetic field that can excite SWs in the medium by coupling to the dynamic magnetization. The SWs can be detected at the opposing antenna by inducing a measurable current in the antenna.

2.6.1 Unidirectionality of magnetostatic surface spin waves

Magnetostatic surface spin waves (MSSWs), also referred to as Damon-Eshbach (DE) surface SWs, are non-reciprocal in the dipolar regime in terms of their amplitude [34]. The geometry of the DE mode is shown in Fig. 2.5.2 (a), where the SW propagates in the sample plane along the x-axis, perpendicular to the magnetization vector directed along the z-axis. Depending on the propagation direction, the MSSW is located either at the top or bottom surface of the film, from which the SW amplitude decays exponentially, as indicated by the striped curves in Fig. 2.6.1 (a).
The surface character of the MSSW can be explained by the asymmetry of its dynamic dipolar fields, depicted in Fig. 2.6.1 (b). Thereby, the total magnetization $\mathbf{M}$ of the magnetic film is split into a time independent and a dependent part, defined by the dynamic magnetization $\tilde{\mathbf{m}}$:

$$\mathbf{M} = \begin{bmatrix} 0 \\ 0 \\ M_{\text{S}} \end{bmatrix} + \begin{bmatrix} \tilde{m}_x(t) \\ \tilde{m}_y(t) \\ 0 \end{bmatrix}. \tag{2.32}$$

The x- and y- components $\tilde{m}_x(t)$ and $\tilde{m}_y(t)$ of the dynamic magnetization, indicated by wide arrows in Fig. 2.6.1 (a), induce surface magnetic charges (plus and minus signs) which in turn generate dipolar fields (solid and dashed lines). The dipolar fields stemming from the surface magnetic charges only interfere constructively on one side of the

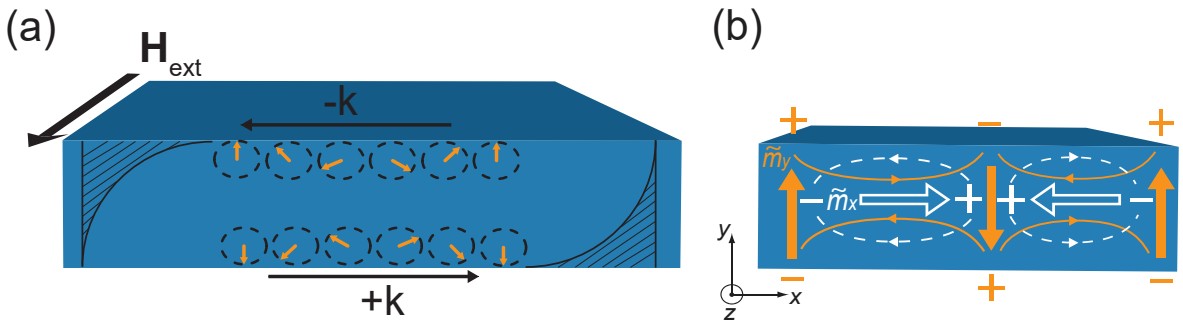

Figure 2.6.1: (a) Magnetostatic surface spin wave (MSSW) propagating in $-k$ direction at the top surface and $+k$ direction at the bottom surface. The amplitude of the SWs decay exponentially in the volume. (b) X- and y-components of the dynamic magnetization $\tilde{\mathbf{m}}(t)$ (wide arrows) stemming from the MSSW propagating in positive x-direction. The induced magnetic poles are represented with plus and minus signs, which in turn generate dipolar fields depicted by the solid and dashed lines. The dipolar fields only add up on one side of the magnetic slab, in this case at the bottom surface. Figure (b) adapted from Ref. [33].

film, which leads to an asymmetry in the resulting total dipolar magnetic field. The dynamic magnetization $\tilde{\mathbf{m}}$ tries to compensate for the asymmetry of the dipolar field by exhibiting a larger amplitude on one side of the film, depending on the propagation direction [33]. Since the dipolar fields of the MSSWs are the cause of their non-reciprocity, high frequency exchange SWs in the DE geometry are in general not unidirectional.
In magnetic films with a thickness much larger than the wavelength of the MSSW ($t_{\mathrm{FM}} \gg \lambda$), the leakage from the opposing surface is virtually zero due to the exponential decay and unidirectional transport is observed. In $Y_3Fe_5O_{12}$ films with a thickness of several micrometers, this has been established a few decades ago [8, 9]. In thin magnetic films the effect is still present, but due to leakage from the counter propagating wave on the opposing surface, the difference in amplitude is limited. In a 20 nm thick $Ni_{80}Fe_{20}$ film the amplitude of MSSWs propagating in opposing directions was found to only differ by a few percent [35]. MSSWs are susceptible to surface roughness scattering and exhibit rather small group velocities, which makes them less interesting for applications [36].

2.6.2 Unidirectionality induced by interfacial Dzyaloshinskii-Moriya interaction

The Dzyaloshinskii-Moriya interaction (DMI) adds an antisymmetric part to the total exchange interaction of a ferromagnetic solid. The DMI between the two neighboring atomic spins $\mathbf{S}_1$ and $\mathbf{S}_2$ is given by

$$\mathcal{H}_{\mathrm{DMI}} = -\mathbf{D}_{12} \cdot (\mathbf{S}_1 \times \mathbf{S}_2), \tag{2.33}$$

where $\mathbf{D}_{12}$ is the DM vector [37]. The DMI can be induced by the lack of inversion symmetry in lattices or by the breaking of inversion symmetry at an interface [38]. The

interfacial DMI (iDMI) is of particular interest here, as it can lead to an asymmetric SW dispersion relation. The iDMI is inversely proportional to the film thickness and can be particularly strong at the interface of a ferromagnet and a heavy metal with a strong spin-orbit coupling such as platinum [39]. A finite iDMI affects the magnetization dynamics of the system by adding an additional term to the effective magnetic field in the Landau-Lifshitz-Gilbert (LLG) equation (cf. Eq. 2.7). In the Damon-Eshbach geometry, the effective field $\mathbf{H}_{\text{eff}}$ is then modified to [39]

$$\mathbf{H}_{\text{eff}} = \nu H_{\text{ext}} \hat{\mathbf{e}}_z + \frac{2A_{\text{ex}}}{\mu_0 M_{\text{S}}^2} \nabla^2 \mathbf{M} - \frac{2D}{\mu_0 M_{\text{S}}^2} \left(\hat{\mathbf{e}}_z \times \frac{d\mathbf{M}}{dt} \right) + \mathbf{H}_{\text{dip}}, \tag{2.34}$$

where $\nu = \pm 1$ indicates the orientation of the external magnetic field along the unit z-vector $\hat{\mathbf{e}}_z$, D the strength of the DMI and A_{ex} the exchange stiffness constant. By inserting the modified effective magnetic field into the LLG equation, the new dispersion relation can be derived (see Ref. [39] for details). By neglecting the nonlocal magnetostatic contribution and the exchange interaction in the limit of small k-values, the dispersion can be written as

$$\omega = \gamma \mu_0 [H_{\text{ext}}(H_{\text{ext}} + M_{\text{S}})]^{\frac{1}{2}} + \frac{M_{\text{S}}^2 |k| t_{\text{FM}}}{4[H_{\text{ext}}(H_{\text{ext}} + M_{\text{S}})]^{\frac{1}{2}}} + \frac{2\nu D}{\mu_0 M_{\text{S}}} k. \tag{2.35}$$

The dispersion is asymmetric under reversal of the propagation direction. Therefore, the iDMI induces a non-reciprocity in the frequency domain. This becomes apparent when plotting the dispersion relation for different values of D as shown in Fig. 2.6.2. Here, the layer thickness $t_{\text{FM}} = 1\,\text{nm}$, saturation magnetization $M_{\text{S}} = 800\,\text{kA/m}$ and exchange constant $A = 1.3 \times 10^{-11}\,\text{J/m}$ are used in the calculation [39].

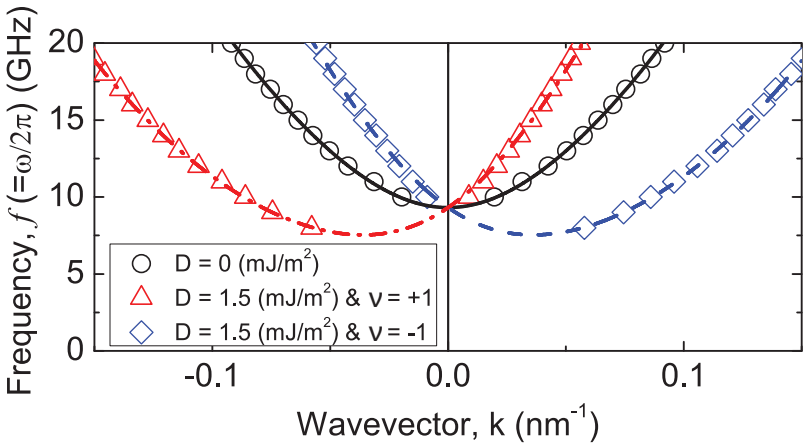

Figure 2.6.2: Spin wave dispersion of the Damon-Eshbach mode for different values of the Dzyaloshinskii-Moriya interaction (DMI) constant D. In the presence of a finite interfacial DMI (red and blue curve), the dispersion is asymmetric under reversal of $\mathbf{k}$. The value of $\nu = \pm 1$ determines the orientation of the external magnetic field along the z-axis. Taken from Ref. [39].

A frequency non-reciprocity induced by an iDMI has been observed with Brillouin spectroscopy in a Pt/Co/Ni multilayer as well as in Pt/CoFeB films [10, 40]. The iDMI can also lead to non-reciprocal group velocities of SWs traveling in opposite directions, which was reported in Ref. [11] for a 7 nm thick $Y_3Fe_5O_{12}$ grown on a gadolinium gallium garnet substrate.
The experimental realization of unidirectional SW transport in a device induced by the iDMI proves to be a difficult task, as such a system requires both a large iDMI and a low damping parameter [41].

2.6.3 Unidirectionality by chiral pumping via a local magnetic transducer

By placing local magnetic transducers, such as nanowires, on top of a magnetic film, unidirectional SWs can be excited in the film by the dipolar coupling to the nanowires [12]. Thereby, dipolar-exchange SWs of the DE mode are "pumped" into the ultrathin (tens of nanometers) magnetic film by a microwave. The generated SWs only propagate perpendicular to the nanowires in one direction, depending on the orientation of the magnetization in the film, which makes this mode chiral. The periodicity s of the nanowires thereby defines the possible in-plane wave vectors $k^{(n)} = n\pi/s$ of the excited SWs, with n an even integer. Therefore, this effect is referred to as chiral pumping. Since the magnetic film exhibits a thickness of only a few nanometers, the inherent chirality present in the DE mode (cf. Sec. 2.6.1) is negligible here.
Figure 2.6.3 (a) shows an array of nanowires on top of a magnetic thin film, with the external magnetic field applied along the z-axis. The dimensions of the wires and the thin film are defined as shown Fig. 2.6.3. In the following, the theoretical description of the dipolar coupling between the wires and the SWs in the magnetic film is outlined. Here, the exchange interaction is neglected as a nonmagnetic spacer (depicted in yellow in Fig. 2.6.3 (a)) is introduced between the nanowires and the magnetic film. However, the chiral pumping of SWs is still possible in the presence of a finite exchange coupling as shown in Ref. [42]. Further experimental data revealed that the addition of a nonmagnetic spacer suppresses the chiral pumping effect, which confirms that the mechanism is dominated by dipolar interactions [13].
In the experiment, a microwave antenna is fabricated on top of the nanowires to excite the Kittel mode of the nanowires through an oscillating field as discussed in Sec. 2.2. Hereby, the magnetization of the wires with amplitude $(M^{\mathrm{K}}_{0,x}, M^{\mathrm{K}}_{0,y})$ precesses with ω_{K} around the equilibrium position directed along the z-axis. Due to the strong shape anisotropy and large magnetization, the FMR frequency of the nanowires is much higher than that of the underlying thin film [43]. The x- and y-component of the magnetization vector are then given by

$$\begin{pmatrix} M^{\mathrm{K}}_x(\mathbf{r},t) \\ M^{\mathrm{K}}_y(\mathbf{r},t) \end{pmatrix} = \Theta(h-x)\Theta(x) \sum_{n\geq 0}^{\text{even}} 2 f_n \cos\left(k_y^{(n)} y\right) \cdot \begin{pmatrix} M^{\mathrm{K}}_{0,x} \cos(\omega_{\mathrm{K}} t) \\ M^{\mathrm{K}}_{0,y} \sin(\omega_{\mathrm{K}} t) \end{pmatrix} \tag{2.36}$$

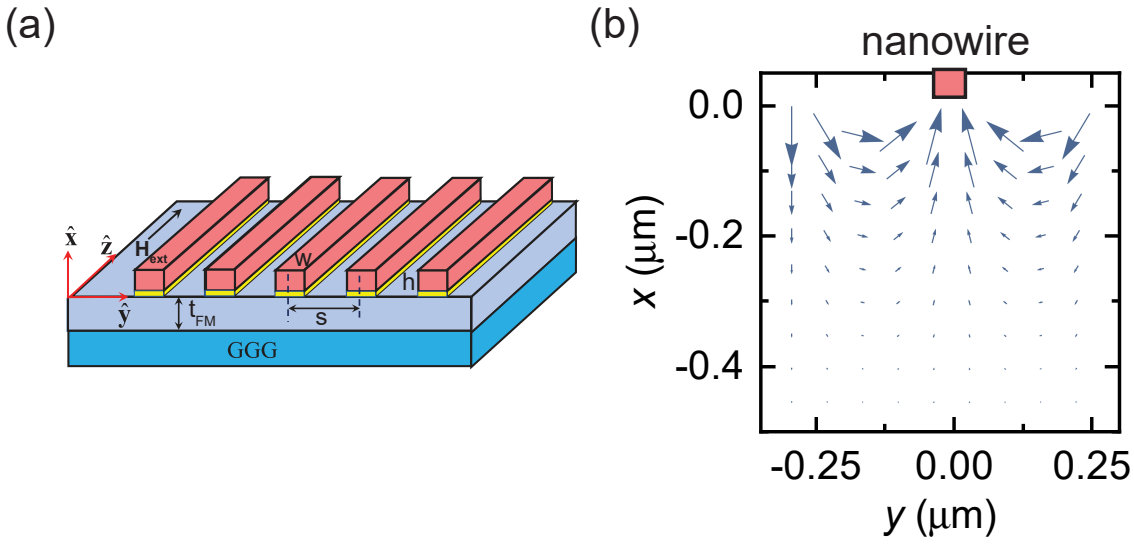

Figure 2.6.3: (a) Array of nanowires on a magnetic film with the thickness t_{FM}. The wires with the width w and height h are placed with the periodicity s along the y-axis. The external magnetic field $\mathbf{H}_{\mathrm{ext}}$ is directed along the z-axis. (b) Dipolar field below a nanowire indicated by a red square located at $x = 0$ and $y = 0$. The long axis of the wire continues into the drawing plane. Figure (a) taken from Ref. [42].

where $\Theta(x)$ is the Heaviside step function and

$$f_n = \left(1 - \frac{1}{2}\delta_{n0}\right) \frac{2}{\pi n} \sin\left(\frac{w}{2} k_y^{(n)}\right). \tag{2.37}$$

The in-phase precession motion of the magnetization in the nanowires generates a dipolar field that is periodic in the direction perpendicular to the wires. With the general formula of the dipolar field

$$h_\beta^{\mathrm{D}}(\mathbf{r}, t) = \frac{1}{4\pi} \partial_\beta \int d\mathbf{r}' \frac{\partial_\alpha M_\alpha^{\mathrm{K}}(\mathbf{r}', t)}{|\mathbf{r} - \mathbf{r}'|}, \qquad \alpha, \beta = \{x, y\} \tag{2.38}$$

and the expression for the magnetization in Eq. (2.36), the dipolar field of the wires can be written as

$$\begin{pmatrix} h_x^{\mathrm{D}}(\mathbf{r}) \\ h_y^{\mathrm{D}}(\mathbf{r}) \end{pmatrix} = \sum_{n\geq 0}^{\text{even}} F_n e^{\left|k_y^{(n)}\right| x} \left[M_{0,\mathrm{R}}^{\mathrm{K}} \begin{pmatrix} \cos\left(-k_y^{(n)} y - \omega_{\mathrm{K}} t\right) \\ \sin\left(-k_y^{(n)} y - \omega_{\mathrm{K}} t\right) \end{pmatrix} + M_{0,\mathrm{L}}^{\mathrm{K}} \begin{pmatrix} \cos\left(k_y^{(n)} y - \omega_{\mathrm{K}} t\right) \\ -\sin\left(k_y^{(n)} y - \omega_{\mathrm{K}} t\right) \end{pmatrix} \right] \tag{2.39}$$

with the form factor

$$F_n = f_n \left(1 - e^{-\left|k_y^{(n)}\right| h}\right). \tag{2.40}$$

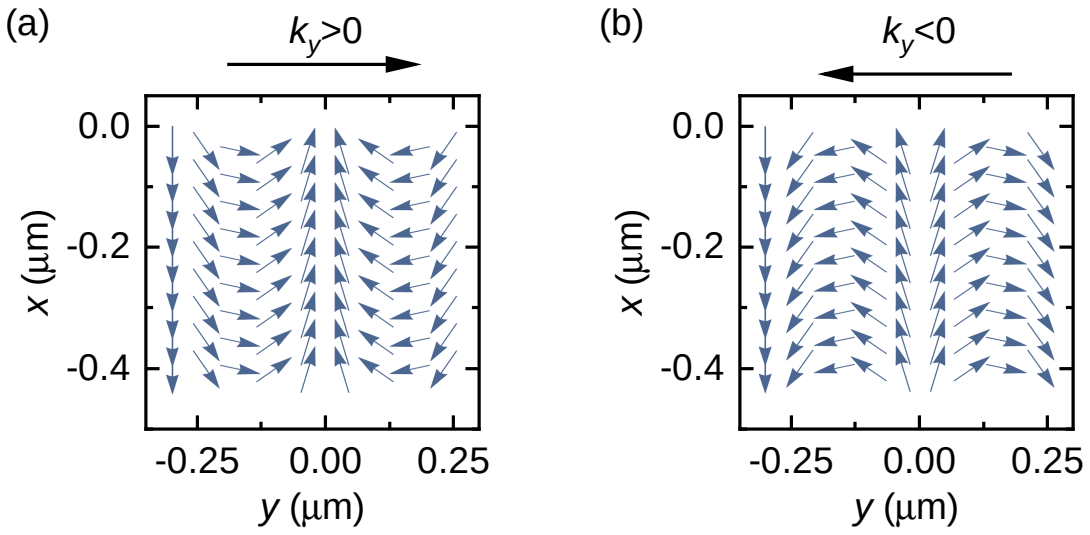

Figure 2.6.4: Components of the thin film magnetization $\mathbf{M}$ in the x-y-plane at $t = 0$ for (a) a fully right circularly polarized spin wave (SW) propagating in positive y-direction ($k_y > 0$) and (b) an equivalent SW traveling in negative y-direction ($k_y < 0$).

Here, the magnetization of the wires is decomposed into the right and left circularly polarized components $(M_\mathrm{x}^\mathrm{K}, M_\mathrm{y}^\mathrm{K})^T = M_\mathrm{R}^\mathrm{K}(1,1)^T + M_\mathrm{L}^\mathrm{K}(1,-1)^T$ and interwire dipolar interactions are disregarded. The dipolar field of the wires at the time $t = 0$ is depicted in Fig. 2.6.3 (b) for the parameters $n = 2$, $h = 30\,\mathrm{nm}$, $w = 110\,\mathrm{nm}$, $s = 600\,\mathrm{nm}$ and $t_\mathrm{FM} = 20\,\mathrm{nm}$ utilized in Ref. [13]. The dipolar field of the nanowires couples to the magnetic moments in the film. Comparing the magnetization dynamics of SWs propagating in $+y$ and $-y$-direction to the dipolar field generated by the nanowires gives insight on why their coupling is chiral. The SWs in the magnetic film with precession frequency ω propagate along the y-axis and can be described by the magnetization components

$$\begin{pmatrix} M_x^\mathrm{SW}(\mathbf{r}) \\ M_y^\mathrm{SW}(\mathbf{r}) \end{pmatrix} = M_\mathrm{0,R}^\mathrm{SW}(x) \begin{pmatrix} \cos(k_y y - \omega t) \\ -\sin(k_y y - \omega t) \end{pmatrix} + M_\mathrm{0,L}^\mathrm{SW}(x) \begin{pmatrix} \cos(k_y y - \omega t) \\ \sin(k_y y - \omega t) \end{pmatrix}, \tag{2.41}$$

where M_R^SW and M_L^SW are the right and left circularly polarized components of the continuous thin film. For a fixed time $t = 0$ the x- and y-components of $\mathbf{M}^\mathrm{SW}$ of a fully right circularly polarized SW propagating in $+y$ and $-y$-direction are depicted in Fig. 2.6.4 (a) and (b), respectively. In this case, the dipolar field of the nanowires in Fig. 2.6.3 (b) matches the precession of the SW with $k_y > 0$ in Fig. 2.6.4 (a) and therefore couples more strongly to SWs propagating in $+y$-direction.
Due to the large shape anisotropy of the nanowires, the underlying magnetic film is magnetically much softer. Therefore, the magnetization of the continuous thin film can be aligned antiparallel to the wire magnetization by reversing the direction of the external magnetic field. The reversal of the magnetization direction in the magnetic film leads to the exact opposite case as depicted in Fig. 2.6.4. The SW with matching rotation

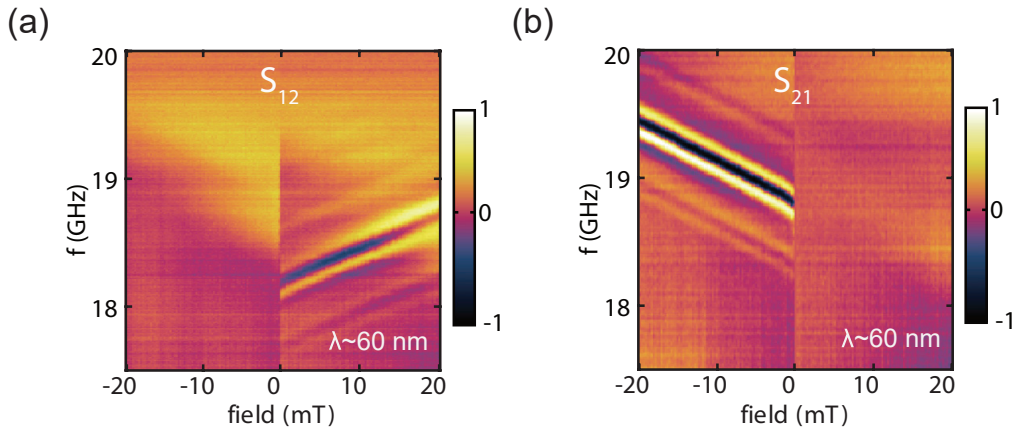

Figure 2.6.5: S_{12} and S_{21} transmission spectra for a SW propagation device with a $Y_3Fe_5O_{12}$ thin film as the SW medium and cobalt nanowires as local magnetic transducers. The transmission spectra show short wavelength unidirectional SW modes. The SW propagation direction can be reversed by changing the orientation of the external magnetic field. Taken from [13].

direction in regards to the dipolar field of the wires is then the SW with $k_y < 0$ traveling in $-y$-direction. Thus, the propagation direction of the SWs can be controlled by the orientation of the external magnetic field.

The excitation of unidirectional exchange spin waves by a magnetic nanograting was demonstrated by Chen *et al.* in 2019 [13]. In this experiment, an array of cobalt (Co) nanowires was placed on a $Y_3Fe_5O_{12}$ (YIG) thin film with a thickness of 20 nm. The 110 nm wide and 30 nm thick Co nanowires were fabricated with a period of 600 nm. Two microwave antennas are structured at a distance of 9.5 µm on top of the nanograting. Figure 2.6.5 (a) and (b) show the transmission spectra S_{12} and S_{21} for such a device above 17 GHz. Unidirectional exchange SWs with a wavelength of 60 nm are excited. The large demagnetization field of the nanowires enables the switching between the parallel and antiparallel configuration of the film and wire magnetization by sweeping the magnetic field. The transition from the parallel to the antiparallel state reverses the SW propagation direction. This manifests in S_{12} showing SW modes only for positive magnetic fields whereas the transmission in the opposing direction, S_{21}, exhibits SW modes at negative magnetic fields. The frequency of the observed SW modes coincide well with the frequency of the Kittel mode of the Co nanograting, which is in line with the theory on chiral pumping predicting a strong enhancement of the SW modes in the magnetic film through the Kittel mode of the nanograting.

The excitation of short wavelength with high group velocities and the robust switching of the SW propagation direction makes this method especially promising for future unidirectional microwave devices. Therefore, this work focuses on SW propagation devices with magnetic nanogratings.

Chapter 3

Fabrication Optimization

The fabrication of spin wave (SW) propagation devices with magnetic nanogratings pose several challenges. The SW propagation length of the material used as a SW medium needs to be sufficient enough to allow the SWs to travel across the distance between the two antennas used for SW excitation and detection. Moreover, to be able to excite unidirectional spin waves at all, the Kittel mode of the magnetic nanograting has to be driven efficiently. Therefore, the nanograting material also needs to be optimized for its magnetic properties. Additionally, the patterning process of the nanowires is a major challenge as it requires sub-micrometer precision over a large surface area with a dense pattern structure. Thus, in the following the structural and magnetic properties of the utilized materials in form of $Co_{25}Fe_{75}$ and $Ni_{80}Fe_{20}$ thin film structures are investigated in Sec. 3.1. Afterwards, the fabrication of magnetic nanogratings is extensively discussed in Sec. 3.2. The chapter excludes the characterization of YIG thin films used in Ch. 4, as they are sourced externally and not fabricated in this work.

3.1 $Co_{25}Fe_{75}$ and $Ni_{80}Fe_{20}$ thin film optimization

The following sections 3.1.1 and 3.1.2 focus on the optimization of the magnetic properties of both $Co_{25}Fe_{75}$ (CoFe) and $Ni_{80}Fe_{20}$ (Py) thin films. The structural properties are investigated by high resolution X-ray diffraction measurements and the magnetization dynamics by broadband ferromagnetic resonance (bbFMR) spectroscopy. Finally, the magnetization dynamics of multilayer stacks used for SW devices in Ch. 4, consisting of optimized CoFe, aluminum nitride (AlN) and Py thin films are discussed in Sec. 3.1.3.

3.1.1 Characterization of $Co_{25}Fe_{75}$ multilayer stacks

In this thesis, CoFe is used as a nanograting material in order to excite unidirectional SWs in underlying YIG films and as a propagation medium for SWs in CoFe/AlN/Py structures. Hence, it is essential to improve the damping properties of CoFe thin films by fabricating CoFe multilayer stacks on thermally oxidized silicon (Si) substrates via magnetron sputter deposition (for details see Appendix A.1.3). A series consisting of four different multilayer stacks (see Fig. 3.1.1) is therefore fabricated in-situ. Based on Ref. [23], the effects of a 3 nm thick platinum (Pt) seed layer and a 3 nm thick copper (Cu) buffer layer on the structural and magnetic properties of a 35 nm CoFe thin film

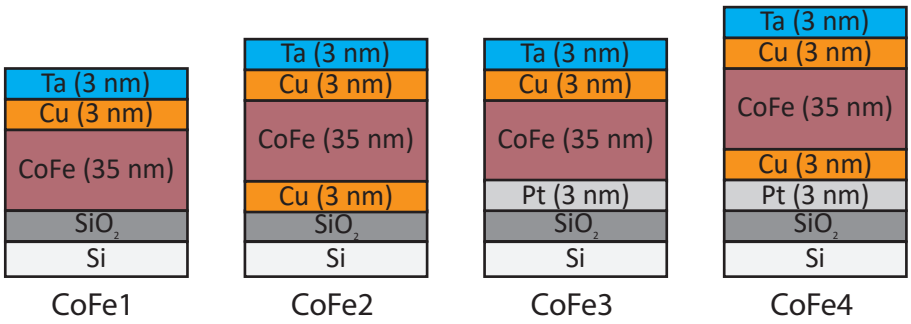

Figure 3.1.1: Stacking sequences of the four $Co_{25}Fe_{75}$ multilayer sample types (CoFe1 - CoFe4) investigated within this thesis. The multilayers are grown on thermally oxidized Si-substrates.

are studied. To reduce oxidation of the CoFe thin films, all samples are capped with a 3 nm thick Cu and a 3 nm thick tantalum (Ta) layer.

The crystalline properties of the CoFe thin films are analyzed by high-resolution X-ray diffraction (HR-XRD, for details see Appendix A.1.6). Figure 3.1.2 shows the 2θ-ω scans of all four multilayer sample types (CoFe1-CoFe4) over a 2θ-range from 34° to 48°. Additionally, a second scan from $2\theta = 68°$ to $2\theta = 70°$ was performed, to normalize the intensities to the Si (004) substrate reflection located at $2\theta = 69.12°$ and thus making the 2θ-ω scans comparable to each other. All multilayers show a reflection at approximately $2\theta = 44.9°$ that can be attributed to the CoFe (110) reflection [44]. The two samples with a Pt seed layer (blue and orange lines) exhibit a broad peak at around $2\theta = 39.8°$, which can be identified as the (111) reflection of Pt. The high intensities of the CoFe (110) reflections of sample type CoFe3 and CoFe4 clearly reveal that Pt seed layers lead to (110)-textured CoFe thin films, while Cu buffer layer further enhance this texturization.

The dynamic magnetic properties of the CoFe multilayer stacks are investigated by performing broadband ferromagnetic resonance (bbFMR, for details on FMR see Sec. 2.2) measurements at room temperature with the external magnetic field $\mu_0 H_{\text{ext}}$ applied in the sample plane.

Figure 3.1.3 depicts the in-plane bbFMR data for all four multilayer sample types (cf. insets in Fig. 3.1.3 for the corresponding stacking sequences). Before the respective bbFMR measurements the magnetizations of the multilayer stacks has been fully saturated at a magnetic field of 1.8 T. The real part of the background corrected S_{21} parameter, $\text{Re}(dS_{21}/dH)$, is plotted as a function of $\mu_0 H_{\text{ext}}$ and f (see Sec. 2.4 and Ref. [29] for details on the background correction method). The fundamental FMR mode of the CoFe layer is visible for all samples. Additionally, in Fig. 3.1.3 (b)-(d), a higher order mode can be seen for the three sample types with Pt and/or Cu layers between the Si substrates and the CoFe thin films.

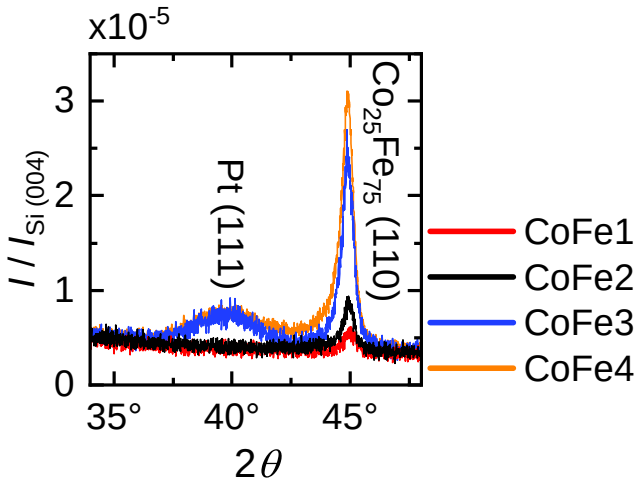

Figure 3.1.2: 2θ-ω scans of different CoFe multilayer samples revealing pronounced CoFe (110) as well as the Pt (111) reflections for multilayer samples with a Pt seed layer. The intensity I is normalized to the Si (004) reflection located at $2\theta = 69.12°$ (not shown here).

From the bbFMR measurements, important material parameters of the CoFe thin films can be extracted. In the following, this will be exemplarily shown in detail for the Pt/Cu/CoFe/Cu/Ta multilayer stack (sample type CoFe4).

Figure 3.1.4 (a) and (b) show raw data of the real and imaginary part of the complex microwave transmission parameter S_{21} around the resonance field $\mu_0 H_{\mathrm{res}}$ obtained by taking a field slice of S_{21} at a constant microwave frequency f. Magnetic field slices of the measurement across a frequency range from 10 GHz to 50 GHz are taken and subsequently fitted with Eq. (2.27). By extracting the resonance field $\mu_0 H_{\mathrm{res}}$ and the linewidth $\mu_0 \Delta H$ from every fit, both can be plotted as a function of the frequency and in turn be fitted with Eqs. (2.14) and (2.17), respectively. These fits shown in Fig. 3.1.4 (c) and (d) then yield material parameters of the CoFe thin film such as the Gilbert damping α, the effective magnetization M_{eff}, the Landé factor g and the magnetic anisotropy H_{ani} as described in Sec. 2.2. Since the applied magnetic field is oriented in the CoFe thin film plane, two-magnon scattering can lead to a nonlinear behavior of $\mu_0 \Delta H$ and an increased damping of the CoFe magnetization compared to out-of-plane bbFMR measurements [23]. This most probably explains the deviation of the measured data from the linear fit function of $\mu_0 \Delta H(f)$ in Fig. 3.1.4 (d).

As described in the previous paragraph, the important material parameters of the CoFe thin films can be extracted from the bbFMR measurements and are listed in Table 3.1.1. Both the Pt seed layer and the Cu buffer layer lead to a reduced Gilbert damping parameter α and an increased effective magnetization $\mu_0 M_{\mathrm{eff}}$. The Pt/Cu/CoFe/Cu/Ta thin film stack exhibits the smallest damping parameter $\alpha = 3.58 \cdot 10^{-3}$ and largest effective magnetization $\mu_0 M_{\mathrm{eff}} = 2.284\,\mathrm{T}$. These parameters are in agreement with previous

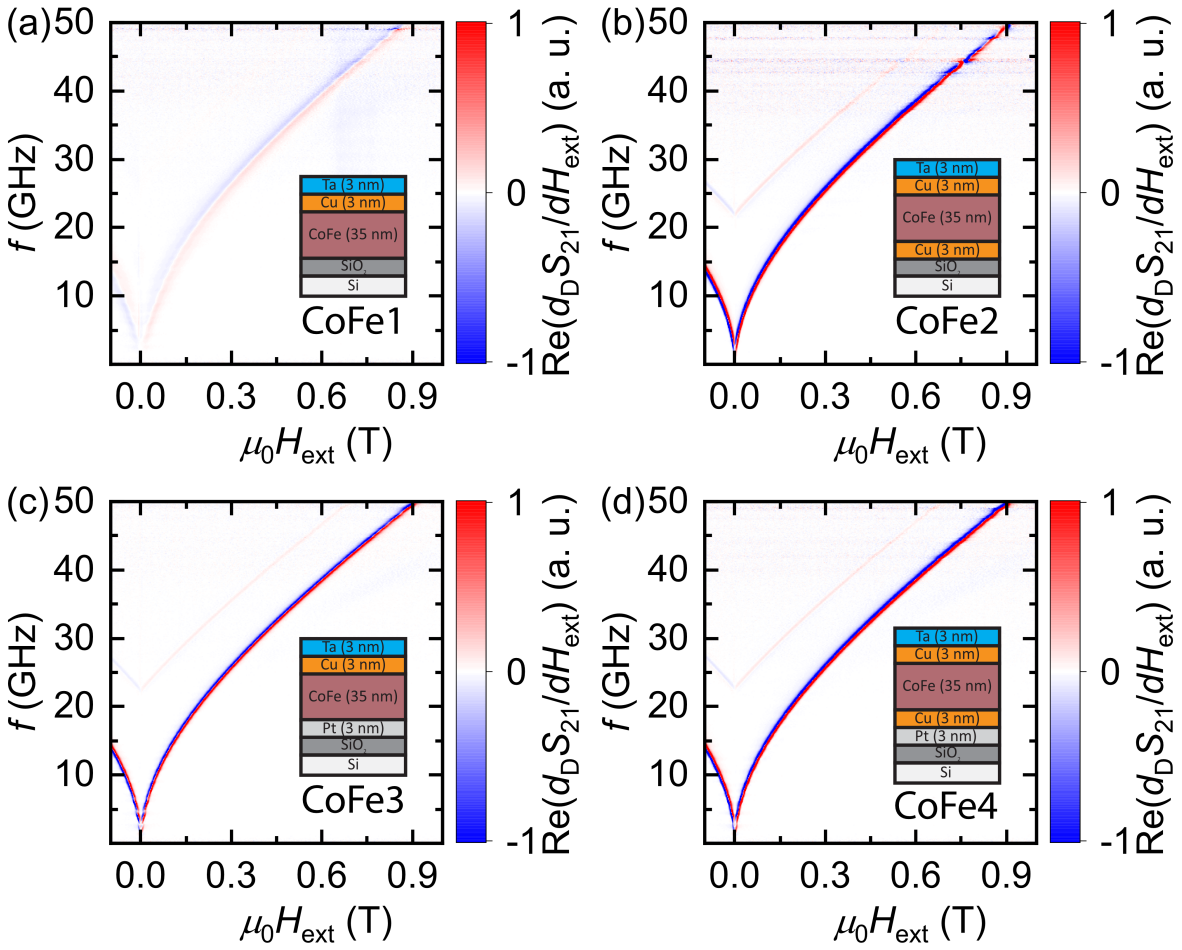

Figure 3.1.3: Real part of the background corrected S_{21} parameter $\mathrm{Re}(d_\mathrm{D} S_{21}/dH_\mathrm{ext})$ as a function of the frequency f and external magnetic in-plane field $\mu_0 H_\mathrm{ext}$ for different CoFe multilayer sample types CoFe1-CoFe4 (see insets in (a)-(d)). Compared to (a), the insertion of Pt seed and Cu buffer layers in (b)-(d) strongly improves the damping properties indicated by the smaller FMR linewidths.

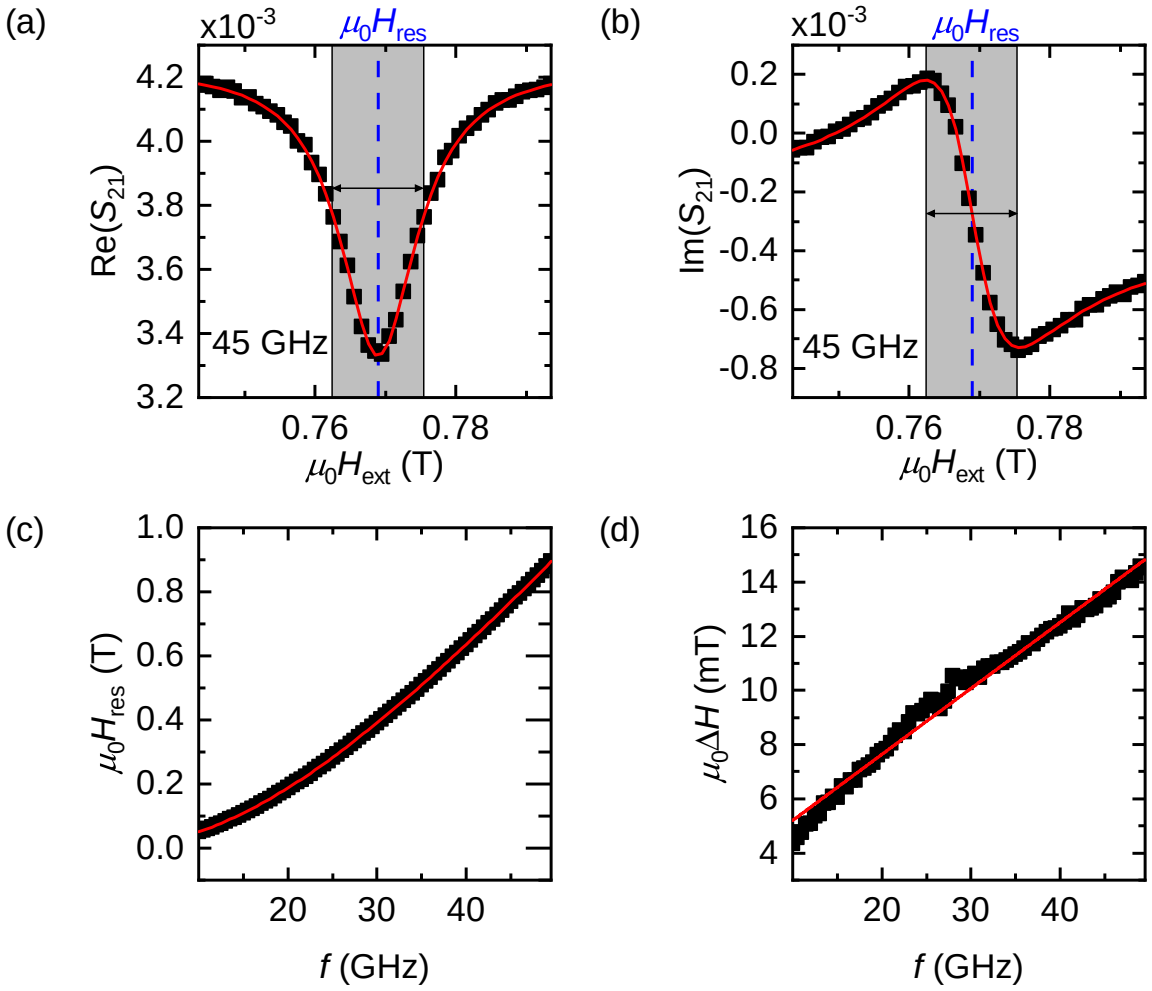

Figure 3.1.4: BbFMR data (black symbols) of the CoFe resonance expemplarily shown for the Pt/Cu/CoFe/Cu/Ta multilayer stack (CoFe4 sample type) measured at room temperature. (a), (b) Raw data of the real and imaginary part of the microwave transmission parameter S_{21} as a function of the in-plane applied magnetic field $\mu_0 H_{\text{ext}}$ measured at the microwave frequency $f = 45$ GHz. The red lines are fits to the real and imaginary part of Eq. (2.27), respectively. The resonance field $\mu_0 H_{\text{res}}$ is indicated as a dashed blue line and the linewidth $\mu_0 \Delta H$ as a black arrow. (c), (d) $\mu_0 H_{\text{res}}$ and $\mu_0 \Delta H$ as a function of f, extracted from the fits to the bbFMR raw data as exemplary shown in (a) and (b). The red lines are fits to Eqs. (2.14) and (2.17), respectively. The deviation of the data from the linear fit curve in (d) is most probably caused by two-magnon scattering (cf. Ref. [23]).

results of $\alpha = 4.78 \cdot 10^{-3}$ and $\mu_0 M_{\text{eff}} = 2.29\,\text{T}$ [23].
The low Gilbert damping and large effective magnetization of the Pt/Cu/CoFe/Cu/Ta multilayer stack enable efficient excitation of the Kittel mode when using this stack as a magnetic nanograting material, while also resulting in a high spin propagation length of approximately 20 µm as reported in Ref. [23]. Therefore, this multilayer recipe was used for both the fabrication of low damping magnetic nanogratings in Ch. 4 and as the SW medium in Ch. 5.

Sample name	$\alpha\,(10^{-3})$	$\mu_0 M_{\text{eff}}$ (T)	g	$\mu_0 H_{\text{ani}}$ (mT)
CoFe1	38.93±1.39	1.865±0.086	2.326±0.042	1.89±0.73
CoFe2	4.40±0.03	2.243±0.002	2.096±0.001	-1.05±0.02
CoFe3	3.74±0.05	2.277±0.006	2.099±0.002	-1.08±0.07
CoFe4	3.58±0.05	2.284±0.002	2.099±0.001	-0.47±0.03

Table 3.1.1: Material parameters of different CoFe thin film sample types extracted from the in-plane bbFMR measurements shown in Fig. 3.1.3. The multilayer stack Pt/Cu/-CoFe/Cu/Ta (sample type CoFe4) exhibits the smallest magnetic damping parameter α and the largest effective magnetization $\mu_0 M_{\text{eff}}$.

3.1.2 Characterization of $Ni_{80}Fe_{20}$ on AlN

In case of the devices utilizing CoFe as the SW propagation medium, $Ni_{80}Fe_{20}$ (Py) is used as material for the nanogratings. To impede an electrical contact between the antennas in these all metallic devices, an insulating layer made of aluminum nitride (AlN) is introduced between the CoFe thin film and the Py nanogratings. Thus, it is essential to ensure that Py keeps its relatively low damping properties when deposited on top of AlN. Therefore, a thin film stack consisting of 35 nm AlN and 30 nm Py (cf. Fig. 3.1.5) is fabricated by magnetron sputter deposition on a thermally oxidized Si substrate. As a reference sample a 30 nm thick Py thin film is deposited onto a thermally oxidized Si substrate without an AlN interlayer. The Py layer in both samples is grown on a 3 nm thick Cu seed layer and capped with a 3 nm Cu and 3 nm thick Ta layer to impede oxidation of the Py. The properties of the Py layers of both samples are compared in the following.

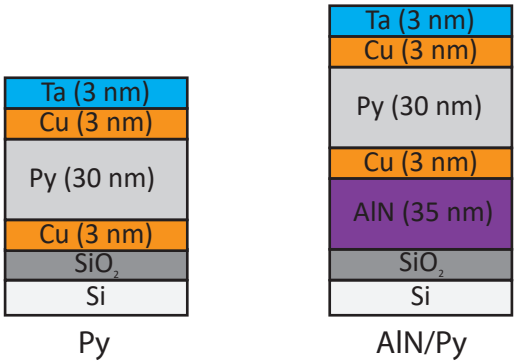

Figure 3.1.5: Stacking sequences of the $Ni_{80}Fe_{20}$ (Py) and AlN/Py multilayer samples investigated in this section. The multilayers are grown on thermally oxidized Si-substrates.

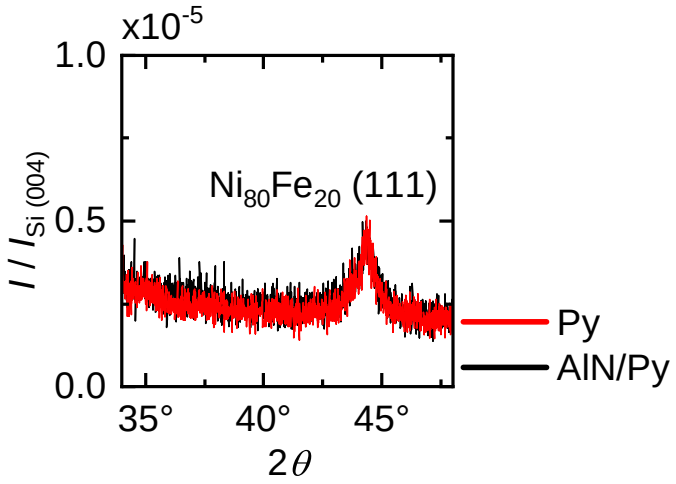

Figure 3.1.6: 2θ-ω scans of the Py thin film and the AlN/Py stack around the Py (111) reflection with approximately the same intensity. The intensity I is normalized to the Si (004) reflection located at $2\theta = 69.12°$ (not shown here).

The crystalline quality of the Py and the AlN/Py thin film stack is investigated by high-resolution X-ray diffraction as shown in Fig. 3.1.6. The intensities are again normalized to the Si (004) substrate reflection. The reflection located at $2\theta = 44.4°$ can be identified as the (111) reflection of Py. Approximately the same intensity of this reflection is observed for both samples, indicating that there is no change in the structural quality of the Py thin film when deposited on AlN.

The dynamic magnetic properties of both Py thin films are investigated by bbFMR measurements at room temperature, where the external, static magnetic field $\mu_0 H_{\text{ext}}$ is applied in the thin film plane. The Py thin films were fully magnetized before the respective bbFMR measurement. The real part of the background corrected S_{21} parameter is

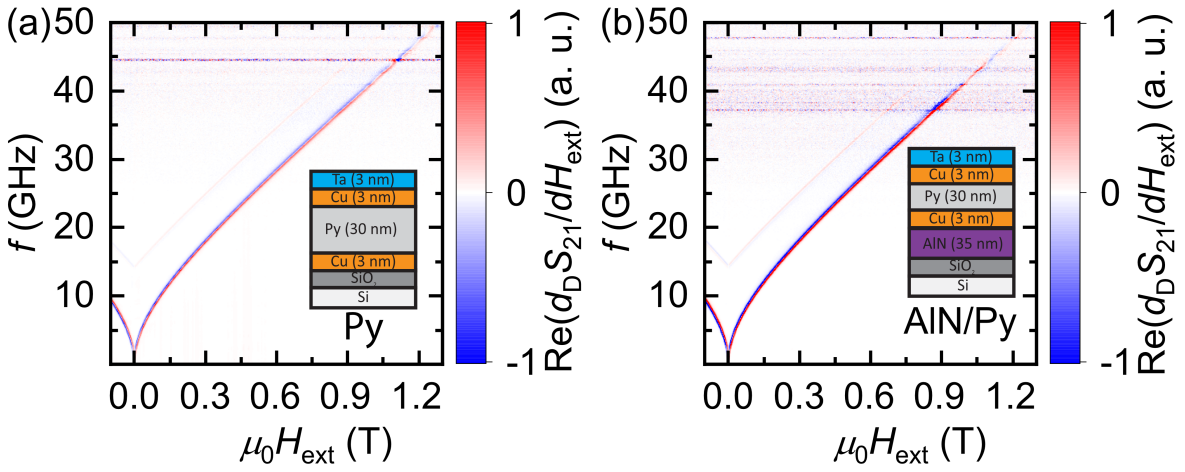

Figure 3.1.7: Real part of the background corrected S_{21} parameter as a function of the frequency f and the in-plane magnetic field $\mu_0 H_{\text{ext}}$ for (a) the Py thin film and (b) the AlN/Py stack measured at room temperature. Next to the fundamental FMR modes, both thin film stacks show a higher order mode and no apparent difference in linewidth as confirmed by the extracted material parameters in Tab. 3.1.2.

plotted as a function of $\mu_0 H_{\text{ext}}$ and f in Fig. 3.1.7. Both Py samples show the fundamental Py mode and a higher order mode with no apparent differences in linewidth or slope when comparing the two plots. This is confirmed by the extracted material parameters listed in Tab. 3.1.2. There is no significant difference in the Gilbert damping parameter α between the two samples and even a slight increase in the effective magnetization $\mu_0 M_{\text{eff}}$ for the Py deposited on the AlN layer. The obtained values for α and $\mu_0 M_{\text{eff}}$ are comparable to previous results of $\alpha = 9.5 \cdot 10^{-3}$ and $\mu_0 M_{\text{eff}} = 0.87\,\text{T}$ [45].
Therefore, it can be concluded that Py keeps its favorable damping characteristics when sputtered on AlN and is suitable to be used as a nanograting material in combination with an insulating layer of AlN.

Stack	$\alpha\,(10^{-3})$	$\mu_0 M_{\text{eff}}$ (T)	g	$\mu_0 H_{\text{ani}}$ (mT)
Py	6.82±0.06	0.941±0.001	2.110±0.001	0.07±0.06
AlN/Py	6.78±0.36	0.958±0.002	2.110±0.001	0.17±0.14

Table 3.1.2: Material parameters of the Py and the AlN/Py thin film stacks extracted from the in-plane bbFMR measurements shown in Fig. 3.1.7.

3.1.3 Characterization of $Co_{25}Fe_{75}$/AlN/$Ni_{80}Fe_{20}$ multilayer stacks

As mentioned in the previous section 3.1.2, for SW propagation devices using CoFe thin films as the propagation medium, Py nanogratings and an insulating AlN layer between the CoFe thin films and the Py nanogratings is employed. To analyze the magnetic prop-

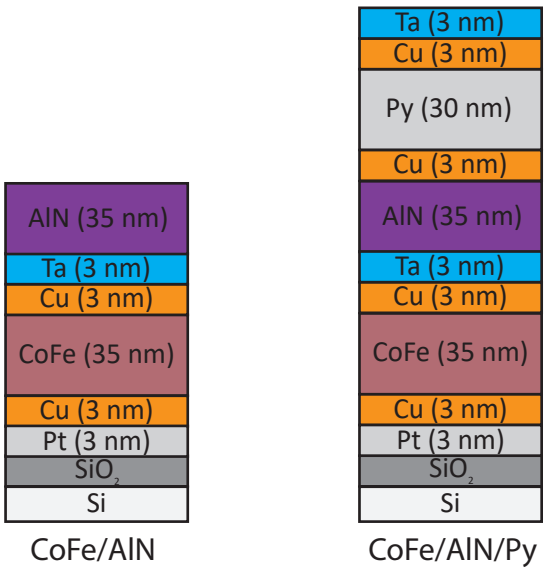

Figure 3.1.8: Stacking sequences of the CoFe/AlN and CoFe/AlN/Py multilayer samples investigated in this section. The multilayers are grown on thermally oxidized Si-substrates.

erties of CoFe and Py thin films combined in one stacking sequence, a CoFe/AlN/Py thin film stack and a CoFe/AlN reference stack are fabricated by magnetron sputtering on thermally oxidized Si substrates. For both samples the earlier optimized seed-, buffer- and capping layers are utilized (see Secs. 3.1.1 and 3.1.2) and the layer thicknesses of the CoFe, AlN and Py remain unchanged at 35 nm, 35 nm and 30 nm, respectively.

To investigate the crystalline quality of these thin film stacks, high-resolution X-ray diffraction measurements were performed (cf. Fig. 3.1.9). Both samples exhibit a reflection peak at approximately $2\theta = 44.9°$, which can be identified as the (110) reflection of CoFe. The higher intensity of the CoFe/AlN/Py sample at this angle can be associated with the additional Py (111) reflection located at $2\theta = 44.4°$ and might also indicate a reduced oxidation of the CoFe layer due to the additional Py layer. As Pt is used as a seed layer for the CoFe thin films, a broad peak stemming from the Pt (111) reflection is visible in both scans at around $2\theta = 39.8°$. The CoFe/AlN/Py sample additionally exhibits a reflection at $2\theta = 36.1°$, which can be ascribed to the (0002) reflection of AlN [46]. The much smaller intensity of this reflection for the CoFe/AlN stack can be explained by the deterioration of AlN over time when exposed to atmosphere and thus further indicates that the Py of the CoFe/AlN/Py stack hinders oxidation of the layers underneath.

In-plane bbFMR measurements are performed for both samples at room temperature and the real part of the background corrected S_{21} parameter is plotted as a function of $\mu_0 H_{\text{ext}}$ and f in Fig. 3.1.10. Both stacks exhibit the fundamental CoFe mode and a higher order CoFe mode. The plot of the CoFe/AlN/Py stack additionally shows the funda-

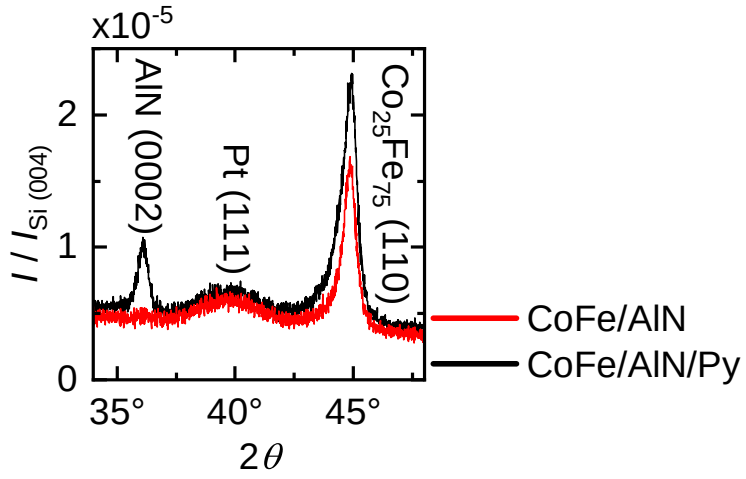

Figure 3.1.9: 2θ-ω scans performed on the CoFe/AlN and CoFe/AlN/Py multilayer stacks revealing CoFe (110) reflections at $2\theta = 44.4°$ and broad Pt (111) reflections at $2\theta = 39.8°$ stemming from the Pt seed layer of the CoFe thin films. The intensity I is normalized to the Si (004) reflection located at $2\theta = 69.12°$ (not shown here). The underlying Py (111) reflection at $2\theta = 44.4°$ and possibly reduced oxidation of the CoFe layer lead to a higher intensity in the case of the CoFe/AlN/Py stack. The AlN (0002) reflection at $2\theta = 36.1°$ has a much higher intensity for the CoFe/AlN/Py stack.

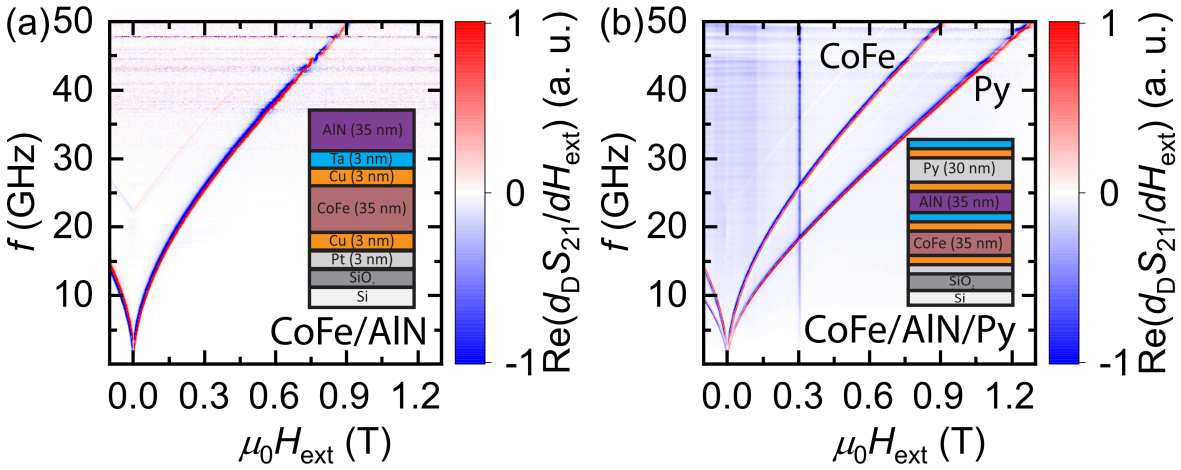

Figure 3.1.10: Real part of the background corrected S_{21} parameter for (a) the CoFe/AlN stack and (b) the CoFe/AlN/Py stack. The applied magnetic field H_{ext} is oriented in the thin film plane and the measurements were executed at room temperature. A higher order CoFe mode is visible for both samples and no apparent difference in linewidth has been found as confirmed by the extracted material parameters in Tab. 3.1.3.

Stack	α (10^{-3})	$\mu_0 M_{\text{eff}}$ (T)	g	$\mu_0 H_{\text{ani}}$ (mT)
CoFe/AlN	3.76±0.03	2.258±0.003	2.093±0.001	0.59±0.04
CoFe/AlN/Py (CoFe)	3.60±0.07	2.300±0.002	2.091±0.001	-1.32±0.02
CoFe/AlN/Py (Py)	7.30±0.04	0.961±0.001	2.109±0.001	0.2±0.03

Table 3.1.3: Material parameters of the CoFe/AlN and the CoFe/AlN/Py stack extracted from the in-plane bbFMR measurements shown in Fig. 3.1.10. In case of the CoFe/AlN/Py stack the corresponding FMR mode (CoFe or Py) is specified in the brackets. Compared to the samples in Secs. 3.1.1 and 3.1.2, no significant differences in the FMR parameters occur except for the damping parameter α of the Py mode of the CoFe/AlN/Py stack. The damping parameter is slightly larger than for the Py thin film on SiOx (cf. Tab. 3.1.2).

mental Py mode below the fundamental CoFe mode and a barely visible higher order Py mode. The material parameters are extracted from the measurement data in Fig. 3.1.10 and shown in Tab. 3.1.3. In the case of the CoFe/AlN/Py stack, the fundamental CoFe and Py mode are both fitted. The obtained values for the damping parameter α and effective magnetization M_{eff} show no significant change when compared to the values of the respective CoFe and Py thin film samples (cf. Tab. 3.1.1 and 3.1.2), with the exception of the damping parameter α of the Py layer in the CoFe/AlN/Py stack, which is slightly higher than the Py thin film value of $\alpha = 6.82 \cdot 10^{-3}$.
These results indicate that CoFe keeps its ultra low damping characteristics and large effective magnetization in a CoFe/AlN/NiFe stack, therefore making a SW propagation device with this stacking sequence worth pursuing.

3.2 Nanograting optimization

In the following, the process of developing a robust fabrication recipe for nanogratings is outlined. First, different resist recipes are used to fabricate nanogratings. In Sec. 3.2.1, these nanogratings are compared with each other by analyzing the corresponding microscope and atomic-force microscopy images. Second, the optimal resist recipe is then used to fabricate CoFe and Py nanogratings, whose magnetization dynamics are investigated by in-plane and out-of-plane bbFMR measurements discussed in Secs. 3.2.2 and 3.2.3.

3.2.1 Resist and dose optimization

All magnetic nanogratings discussed in this thesis are fabricated via electron-beam (e-beam) lithography, DC magnetron sputtering and a subsequent lift-off process. E-beam lithography (for details on the method see Appendix A.1.2) requires a resist that changes its solubility in an associated developer when exposed to an electron beam. A positive resist is removed by its developer in the areas that were exposed to the electron beam, thus allowing material to adhere to the substrates surface in these regions during sputtering. A negative resist uses the opposite working principle, by becoming insoluble to

the developer in the exposed regions. In this work only positive resists were considered for the fabrication, as negative resists would require extensive writing times and have shown to be highly susceptible to minor changes in handling [47].
There is a multitude of interdependent parameters to be considered during e-beam lithography, such as beam energy, electron dose, resist, substrate and development time [48]. To accelerate an otherwise complex optimization process, recipes that are already existing at the WMI are used and only adjusted in the electron dose. This is efficiently done by performing a dose test, where the desired pattern is written multiple times on a single chip, while varying the exposure dose for each pattern. After sputter deposition and the lift-off process, in the underexposed regions the pattern on the chip will be damaged by insufficient clearance of the resist, while in the overexposed areas excessive clearance damages the pattern [48]. By analyzing the topography of the sample via optical and atomic force microscopy (AFM, for details on the method see Appendix A.1.7), the area on the chip with the best pattern quality is found and therefore the optimal dose can be determined.
In the following, three different resist processing recipes (for details see Appendix A.1.5) are tested and the results are analyzed. To assess the performance of each recipe, a dose test is carried out with each resist stack. For this, nanograting structures with a wire width of 200 nm and edge-to-edge distances ranging from $a = 400\,\text{nm}$ to $a = 1200\,\text{nm}$ between neighboring nanowires are written on a thermally oxidized Si substrate with a wide range of doses. Subsequently, the optimized CoFe multilayer stack (see Sec. 3.1.1) is sputtered on the sample and a lift-off process (for details on the method see Appendix A.1.4) is performed to remove the remaining resist.

In Fig. 3.2.1, microscope images of the dose test performed with the resist AR-P 6200.09 (CSAR) are depicted. On the left image, each set of four rectangles represents nanogratings with spacings between the nanowires of 400 nm, 600 nm, 900 nm and 1200 nm structured with the same dose. The dose is gradually increased for each set of four nanogratings from the top right to the bottom left. In the top row the dose was not high enough to fully expose the resist, thus leaving large blank spots in the pattern after the lift-off process. In the bottom left corner at a much higher dose, parts of the CoFe metal were not removed from the valleys in between the nanowires during the lift-off process. Hereby, the exposure of the resist in between the nanowires can be traced back to significant beam broadening due to forward scattering of electrons within the resist and backscattering of electrons from the substrates surface. Both effects are more pronounced at higher doses [48]. The image on the right shows a magnified microscope picture of a nanograting with wire spacings of $a = 900\,\text{nm}$ and no visible defects, indicating that this pattern was written with a viable dose.

To study the topography of the sample fabricated with the CSAR single layer resist recipe in more detail, parts of the nanogratings are scanned with an AFM. Exemplarily, the AFM image of a nanograting with a nominal wire width of 200 nm and a nominal edge-to-edge distance of 900 nm written with the determined viable dose is shown together with a linecut of the scan in Fig. 3.2.2 (a) and (b). The nanowires exhibit an actual width of 350 nm at the base while the wire distance has shrunken to 700 nm. This

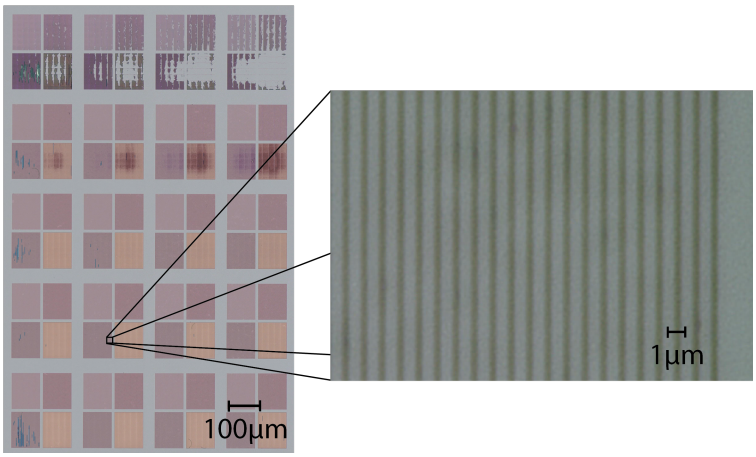

Figure 3.2.1: Microscope image of a dose test performed with the CSAR single layer resist recipe. On the left, only a section of the entire sample is shown. Each set of four rectangles represents nanogratings with a wire width of 200 nm and wire distances a of 400 nm, 600 nm, 900 nm, and 1200 nm (from top left to bottom right). The dose is increased for every set of four nanogratings from the top right to the bottom left of the total picture. On the right, a magnified image of a nanograting with $a = 900$ nm edge-to-edge distance between neighboring nanowires is shown.

widening of the nanowires in regards to the intended width of 200 nm can be explained by the already mentioned effects of electron-beam broadening and backscattering during the e-beam lithography process. Most nanowires exhibit a plateau at around 35 nm height relative to the substrate surface, which corresponds approximately to the thickness of the CoFe multilayer stack sputtered on the substrate (see Sec. 3.1.1). The sharp peaks visible at the edges of some nanowires reaching up to a relative height of 50 nm could be metal being tugged up from the resist during the lift-off process.
Additional to the sample fabricated using the single layer CSAR resist recipe, a sample is fabricated using a double layer stack of PMMA resists AR-P 669.04 and AR-P 679.02 for the e-beam lithography. An AFM scan for this sample is shown in Fig. 3.2.2 (c). A double layer recipe for the e-beam lithography step can be useful to achieve a larger undercut of the resist. This minimizes contact between the sputtered material on the substrates surface and the surrounding resist, thus making the lift-off process easier. The AFM image reveals CoFe nanowires of more than 400 nm width instead of the intended 200 nm and a height of approximately 35 nm. As visible in the linecut in Fig. 3.2.2 (d), the sharp peaks at the edges of the nanowires are less pronounced than when using the CSAR single layer resist recipe (cf. 3.2.2 (b)), which could be traced back to the larger undercut of the PMMA double layer recipe. The valleys between the nanowires are 700 nm wide and contain lots of residue which can be observed for almost all investigated doses. Therefore, even though the larger undercut of the PMMA double layer leads to less metal spikes on the nanowires, the lift-off process is not as clean as using the CSAR single layer resist recipe.
The third sample discussed here is fabricated using a double layer of the resist AR 6200.13

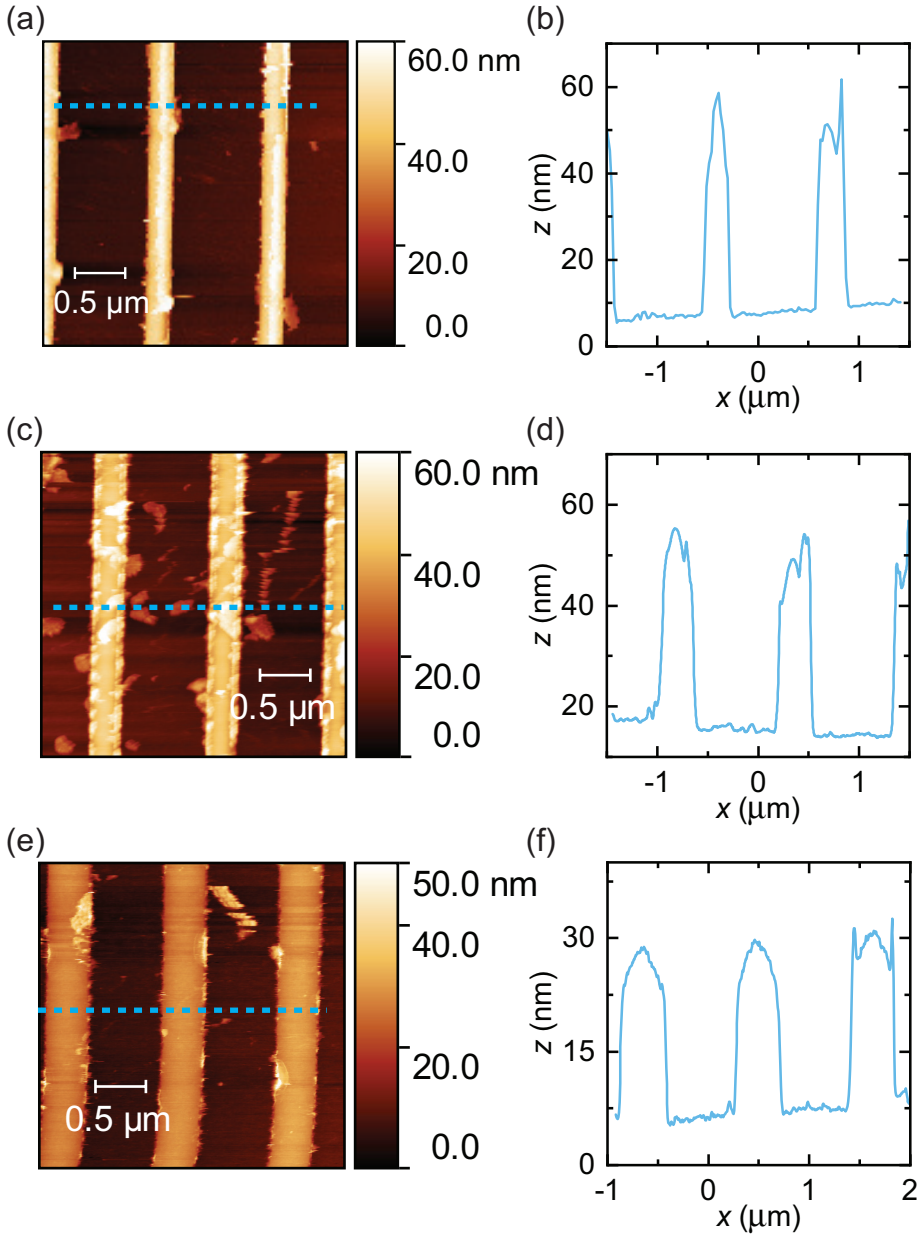

Figure 3.2.2: (a), (c), (e) AFM scans of CoFe nanogratings fabricated using different resist recipes for the e-beam lithography process: single-layer CSAR62 resist (top panels), double-layer PMMA600K/PMMA950K resists (middle panels), and double-layer CSAR62/PMMA950K resists (bottom panels). The nominal width of the nanowires is 200 nm and the nominal edge-to-edge distance between neighboring nanowires is 900 nm of all shown nanogratings. The horizontal blue dashed lines indicate linecuts as shown in (b), (d) and (f), respectively.

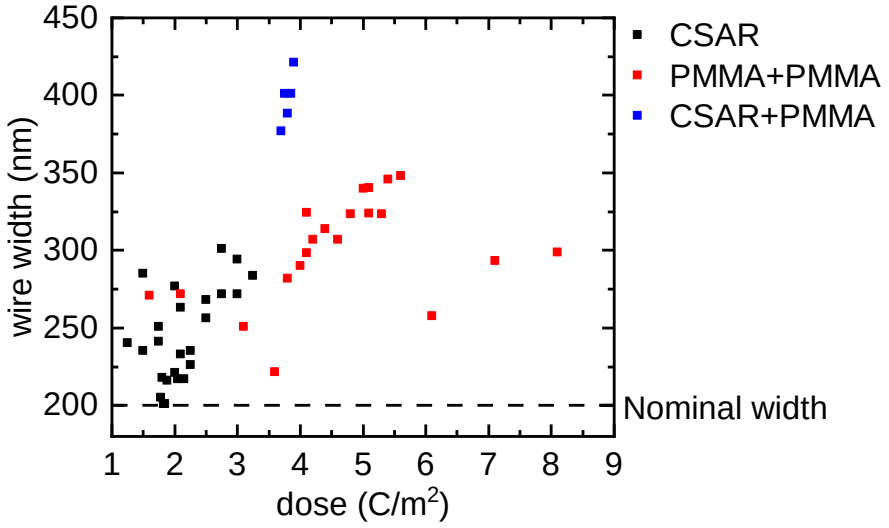

Figure 3.2.3: Width of the nanowires with respect to the applied base dose during the e-beam lithography using the three considered resist recipes: single-layer CSAR resist (black dots), double-layer PMMA/PMMA resists (red dots) and double-layer CSAR/PMMA resists (blue dots). The intended width of 200 nm is indicated as a horizontal black dashed line. For both double layer stacks, doses below 4 C/m^2 turned out to be insufficient to produce reliable results. For the considered resist recipes, the CSAR single layer recipe achieves the best pattern fidelity at a rather low dose of around 2 C/m^2.

(CSAR) and the PMMA resist AR-P 672.045 during the e-beam lithography step, which results in an even larger undercut compared to the previously discussed sample using a PMMA/PMMA double stack resist recipe. The AFM scan of a nanograting with a nominal edge-to-edge distance of 900 nm fabricated with the CSAR/PMMA double layer resist recipe is shown together with a linecut in Fig. 3.2.2 (e) and (f). The width of the nanowires is broadened to about 500 nm while the height is just below 25 nm relative to the substrate surface, which is significantly reduced in regards to the targeted height of 35 nm of the CoFe multilayer stack. For smaller wire distances the strong broadening resulted in a entirely metalized surface with no nanograting structure even at small doses. The profile of the nanowires exhibits less deformities than in case of the samples discussed before, while there is some residue from the lift-off process left between the nanowires.

For all three samples depicted in Fig. 3.2.2 the actual width of the nanowires in relation to the applied dose is measured and plotted in Fig. 3.2.3. The intended width of 200 nm is indicated as a horizontal dashed line. For the CSAR/PMMA double layer resist recipe (blue symbols), the range of doses that produces well defined nanogratings is very narrow. The PMMA/PMMA resist recipe (red symbols) requires relatively large doses to produce reliable results. The CSAR single layer resist recipe (black symbols) leads to the best pattern fidelity by reaching almost the intended wire width of 200 nm

at a relatively low dose of around $2\,\mathrm{C/m^2}$ during the e-beam lithography. Together with a cleaner lift-off process, less processing steps and well predictable broadening even at higher doses, the CSAR single layer resist recipe proves to be the most suitable resist for producing nanogratings. Therefore, all nanogratings discussed in the following are fabricated using the AR 6200.09 (CSAR) resist for the e-beam lithography.

3.2.2 Magnetization dynamics of CoFe nanogratings

For the study of their magnetization dynamics, CoFe nanogratings with a wire width of 200 nm and various edge-to-edge spacings a between the nanowires are fabricated on a thermally oxidized Si substrate using the single layer CSAR resist recipe for the e-beam lithography and the optimized, 35 nm thick Pt/Cu/CoFe/Cu/Ta multilayer stack (see Sec. 3.1.1). The 2 mm long nanowires are repeated over a distance of 4.8 mm taking advantage of almost the entire width of the substrate. The large surface area covered by the magnetic nanograting is necessary to enable an adequate positioning of the nanograting on the transmission line of the CPW as well as to maximize the volume of the investigated magnetic material and thus the FMR signal. BbFMR measurements with the external magnetic field directed in the sample plane parallel and perpendicular to the nanowires (in-plane bbFMR) as well as perpendicular to the sample plane (out-of-plane bbFMR) are performed at room temperature. The external magnetic field is always swept from positive to negative values. The real part of the background corrected S_{21} parameter is then plotted as a function of the external magnetic field $\mu_0 H_{\mathrm{ext}}$ and the microwave frequency f.

In Fig. 3.2.4, the results of the in-plane bbFMR measurements with the external magnetic field directed parallel to the nanowires are depicted for CoFe nanogratings with wire spacings a between 400 nm and 1200 nm. The nanograting with a wire distance of 400 nm (cf. . 3.2.4 (a)) exhibits a clearly visible mode located above 17 GHz. The mode persists under reversal of the external magnetic field down to about $\mu_0 H_{\mathrm{ext}} = -40\,\mathrm{mT}$, instead of being symmetric around $\mu_0 H_{\mathrm{ext}} = 0$ as observed for the planar CoFe thin films in Sec. 3.1.1. At $-40\,\mathrm{mT}$ a discontinuity is observed as the mode jumps back to the field symmetric behavior. This asymmetry can be explained by the shape anisotropy of the magnetic nanowires that leads to a much larger coercivity than in the case of a planar thin film sample with a sufficiently large in-plane expansion [43]. This mode is also visible for the other wire spacings a represented in Fig. 3.2.4 (b), (c) and (d). The CoFe nanograting mode slightly shifts to higher resonance fields with reduced signal amplitude with increasing wire distance, as the amount of magnetic material roughly halves from the nanograting with 400 nm spacing to the nanograting with 1200 nm spacing. The two antiferromagnetic modes which are faintly visible in all colormaps at zero field between 10 GHz and 20 GHz are caused by the CPW and are not related to the sample.
The location of the FMR mode and the coercivity of the nanograting are both relevant for SW propagation experiments. In previous experiments performed by Chen *et al.* [13], unidirectional SWs were excited by a cobalt nanograting at the FMR frequency of the nanograting. Hereby, a large coercivity of the nanograting enabled an antiparallel con-

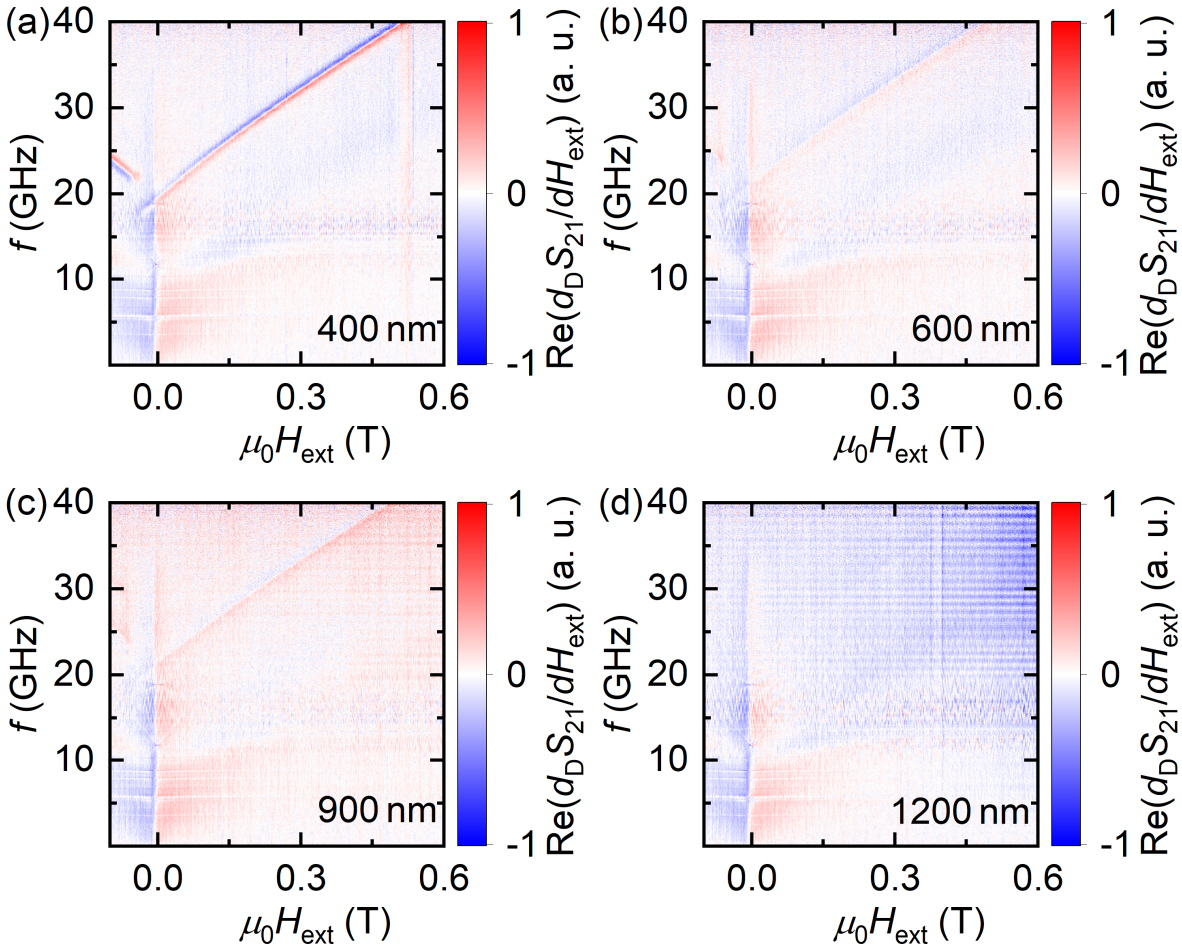

Figure 3.2.4: Room temperature, in-plane bbFMR data of CoFe nanogratings fabricated on a thermally oxidized Si substrate with wire spacings a ranging from (a) 400 nm to (d) 1200 nm. The external magnetic field is applied parallel to the nanowires and swept from positive to negative values. For all spacings the nanogratings exhibit a mode located above 17 GHz that gets weaker in signal amplitude for increasing wire distance. The mode has a coercivity of around 40 mT. The two, barely visible, antiferromagnetic modes at zero field between 10 GHz and 20 GHz are caused by the nickel coating of the microwave CPW used in the experiment.

figuration of the magnetizations of the nanograting and the SW medium over a fairly wide range of magnetic fields. This antiparallel configuration in turn resulted in the most pronounced unidirectional SW modes in the experiment. Therefore, based on the data in Fig. 3.2.4, for the SW propagation devices utilizing CoFe nanogratings in this work, the excitation of unidirectional SWs at frequencies starting at about 17 GHz would be expected.

In Fig. 3.2.5, in-plane bbFMR data with the external magnetic field applied perpendicular to the nanowires of the nanogratings are shown. Due to the shape anisotropy of the nanowires, the pronounced CoFe mode visible in panels (a)-(d) is shifted by approximately 0.26 T with respect to $\mu_0 H_{\text{ext}} = 0$. This shift can be interpreted as the external magnetic field that is necessary to rotate the nanograting magnetization perpendicular to the nanowires. In Fig. 3.2.5 (a) also several crossings of higher order modes appear. With increasing wire spacing a, the distance between these modes of higher order decreases and therefore only the envelope of multiple modes is visible in Fig. 3.2.5 (b)-(d). The observed behavior agrees well with the expected modulation of the SW wavevector k by the dipolar fields of the nanograting resulting in $k = n \cdot \pi/a$ (cf. Sec. 2.6.3). In Fig. 3.2.5 (a), (b) and (d), an additional mode appears at around $\mu_0 H_{\text{ext}} = 0\,\text{T}$ and coincides well with the thin film CoFe FMR mode observed in Fig. 3.1.1. The observation of two modes with different anisotropy contributions could be explained by distinguishing between so-called edge- and bulk-modes (or quasi-uniform modes) [49]. Bulk-modes appear in the center of the nanowires, whereas edge-modes are located near the wire surfaces and thus face a higher anisotropy. As the rotation of the magnetization in the center of a wire away from the long axis is associated with the formation of far smaller stray fields than in the case of the wire surface, the center of a wire behaves more like the bulk material [50]. This leads to the observation of a zero field symmetric mode. In contrast to that, the large demagnetizing field near the wire surface results in a much larger magnetic saturation field needed to align the magnetization along the external magnetic field near the wire surface [49].

Additionally to the in-plane measurements, out-of-plane bbFMR measurements are performed to investigate the influence of the wire spacing a on important material parameters that are extracted from the bbFMR data. The out-of-plane measurements can yield more accurate results, as two-magnon scattering events are entirely suppressed [51]. Figure 3.2.6 (a) and (b) show the effective magnetization and the g-factor for CoFe nanogratings with wire spacings a ranging from 100 nm to 1500 nm. Both plots indicate that a significant change in the magnetization dynamics of the nanograting takes place at $a = 300\,\text{nm}$. Both the effective magnetization M_{eff} and the g-factor are decreased for $a < 300\,\text{nm}$. This can be attributed to coupling between the nanowires, which becomes significant as a decreases. At small wire distances the interaction of the stray field of a single wire with the magnetization of a neighboring wire could lead to an antiferromagnetic coupling, reducing stray fields and thus the overall effective magnetization measured for the magnetic nanograting [43].
As a large effective magnetization and the efficient excitation of the Kittel mode is nec-

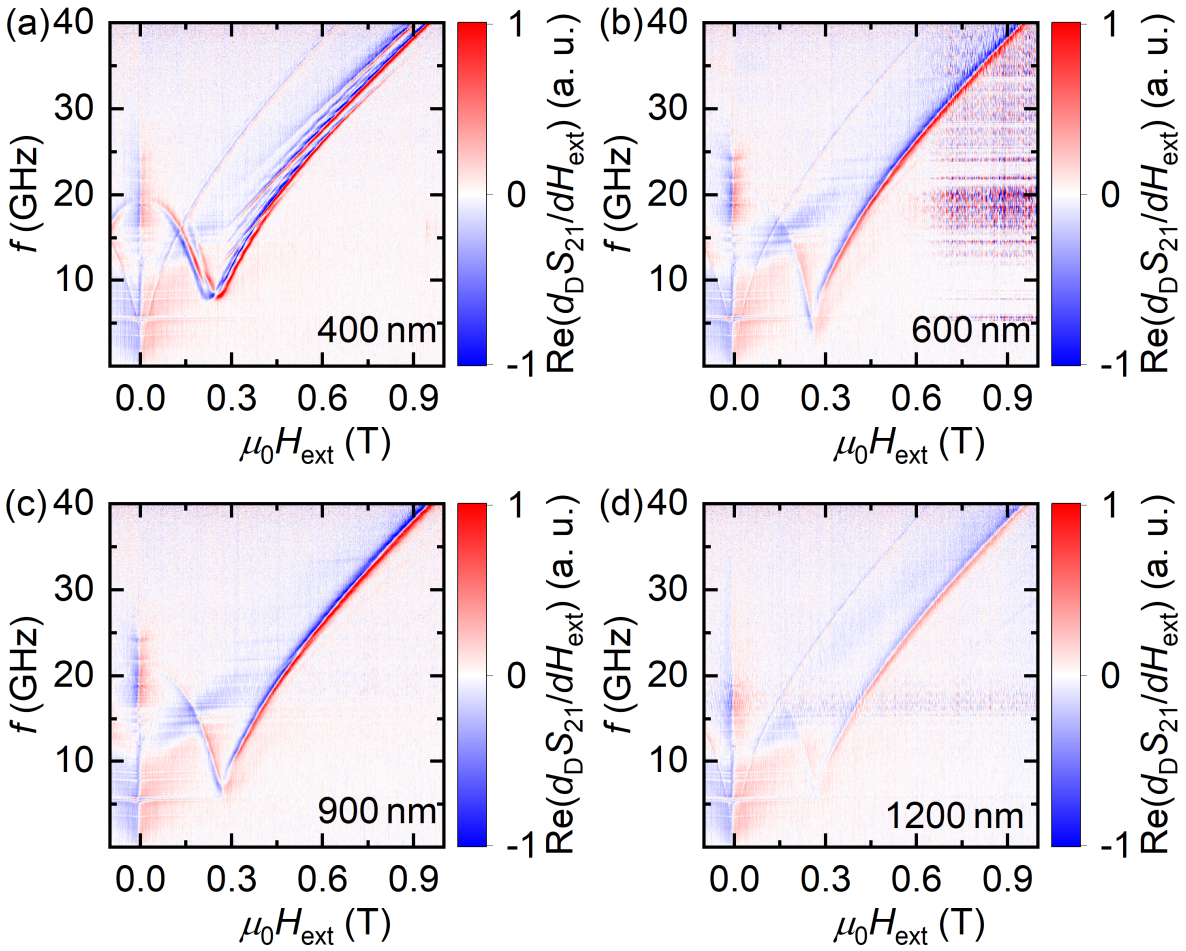

Figure 3.2.5: Room temperature, in-plane bbFMR data of CoFe nanogratings fabricated on a thermally oxidized Si substrate wire spacings a ranging from (a) 400 nm to (d) 1200 nm. The external magnetic field is applied perpendicular to the nanowires and swept from positive to negative values. The shape anisotropy of the nanowires leads to a shift of the most pronounced CoFe mode of approximately 0.26 T. Except for the 900 nm nanograting, all measurements also exhibit a fundamental CoFe mode around 0 T

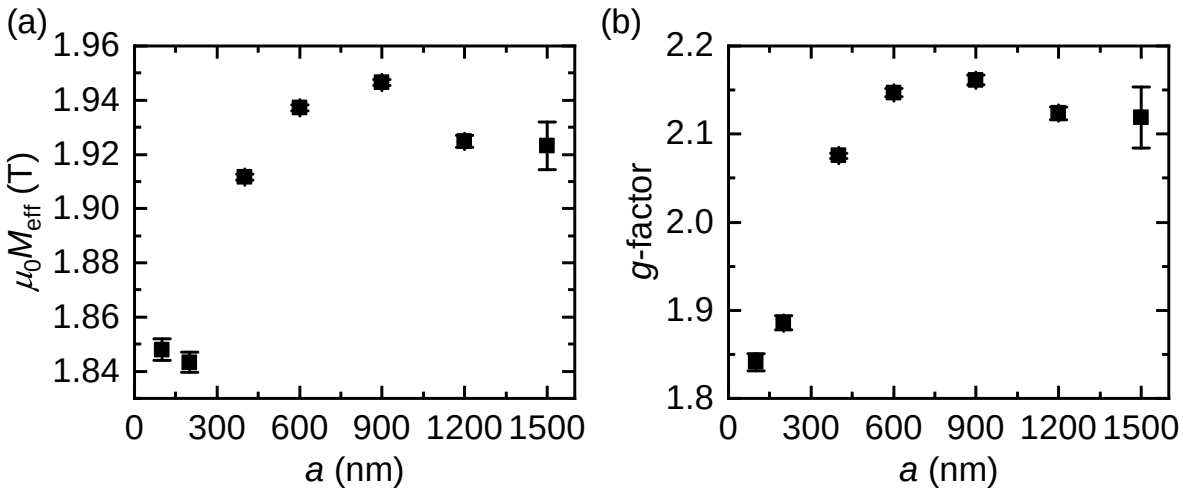

Figure 3.2.6: (a) Effective magnetization $\mu_0 M_{\mathrm{eff}}$ and (b) g-factor of the CoFe nanogratings as a function of the wire spacing a extracted from out-of-plane bbFMR measurements. Around $a = 300\,\mathrm{nm}$ the effective magnetization $\mu_0 M_{\mathrm{eff}}$ and g-factor drop, as the coupling between the nanowires becomes more prevalent.

essary for pumping chiral SWs, only nanogratings with wire spacings of $a = 400\,\mathrm{nm}$, 600 nm and 900 nm are considered for the SW propagation devices. These nanogratings showed strong FMR signals without its magnetic properties being impaired by a finite coupling between the nanowires.

3.2.3 Magnetization dynamics of $Ni_{80}Fe_{20}$ nanogratings

For the SW propagation devices with CoFe as the SW medium, $Ni_{80}Fe_{20}$ (Py) nanogratings are utilized. For the fabrication of the Py nanogratings, the same resist recipe as for the CoFe nanogratings is used. With the 30 nm thick Py multilayer stack discussed in Sec. 3.1.2 and the CSAR resist recipe from Sec. 3.2.1, Py nanogratings with wire spacings a ranging from 400 nm to 1200 nm are fabricated on a thermally oxidized Si substrate. As in Sec. 3.2.2, the 2 mm long nanowires are repeated over a length of 4.8 mm. The magnetization dynamics of the Py nanogratings are then analyzed by performing bbFMR measurements at room temperature with the external, static magnetic field $\mu_0 H_{\mathrm{ext}}$ applied in the thin film plane. Thereby, the magnetic field is again swept from positive to negative field values and the real part of the S_{21} transmission parameter is recorded. The background of S_{21} is reduced using the derivative divide method (for details see Sec. 2.4 and Ref. [29]). $\mathrm{Re}(d_{\mathrm{D}} S_{21}/dH_{\mathrm{ext}})$ is then plotted as a function of f and $\mu_0 H_{\mathrm{ext}}$.

Fig. 3.2.4 shows the corresponding measurement results of Py nanogratings with wire spacings a of 400 nm, 600 nm, 900 nm and 1200 nm, where the external magnetic field is directed parallel to the nanowires. The nanogratings with $a = 400\,\mathrm{nm}$ and 600 nm exhibit a clearly visible mode above 7.5 GHz (see Figs. 3.2.7 (a) and (b)). The mode is symmetrical around zero field indicating that the coercivity of the Py nanogratings

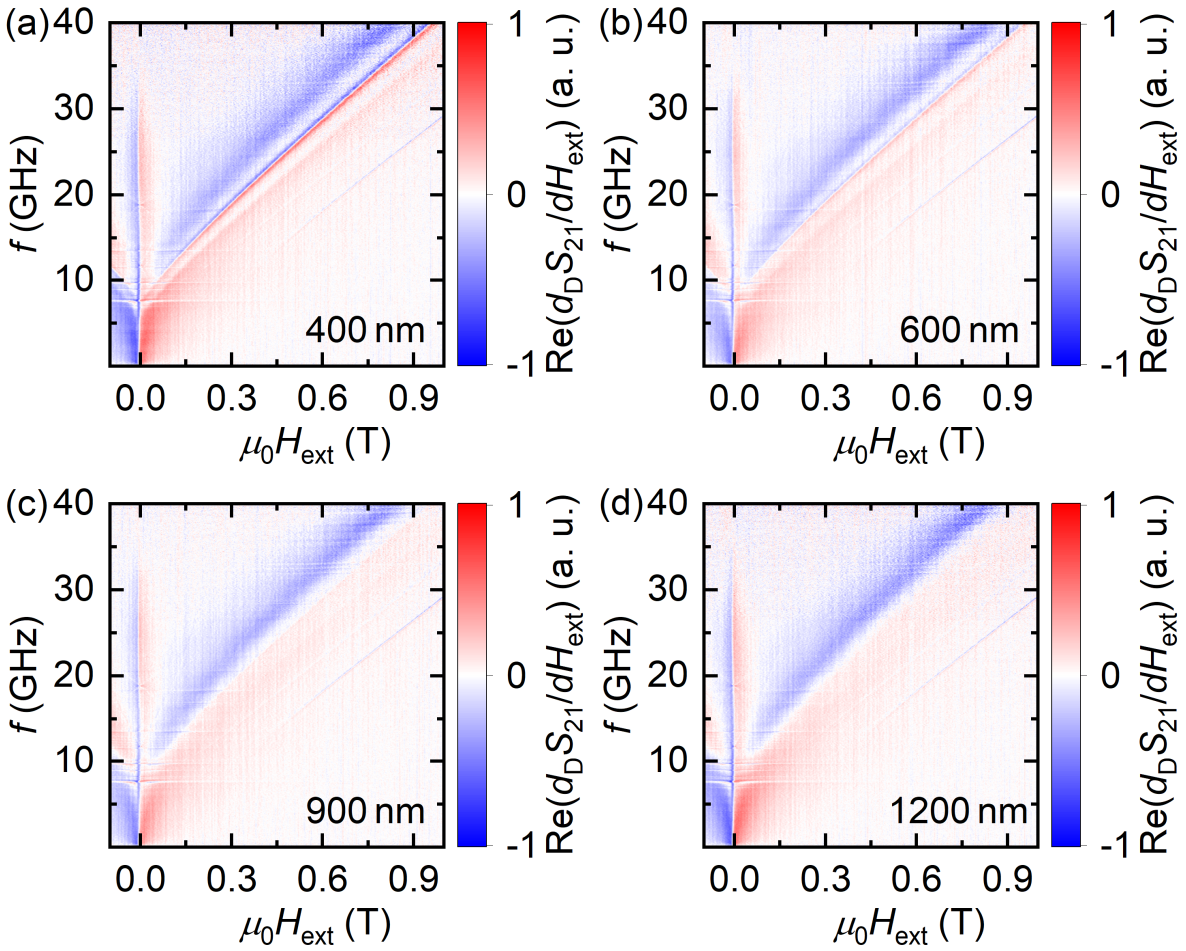

Figure 3.2.7: In-plane bbFMR data with the external magnetic field applied parallel to the Py nanowires with spacings a between 400 nm and 1200 nm. The plots in (a) and (b) exhibit a clearly visible nanograting mode starting at a much lower frequency than in the case of the CoFe nanogratings. All measurements show a faintly visible linear mode at around 15 GHz for a magnetic field of 0.6 T, which can be identified as the electron spin resonance mode (ESR) of the Si substrate.

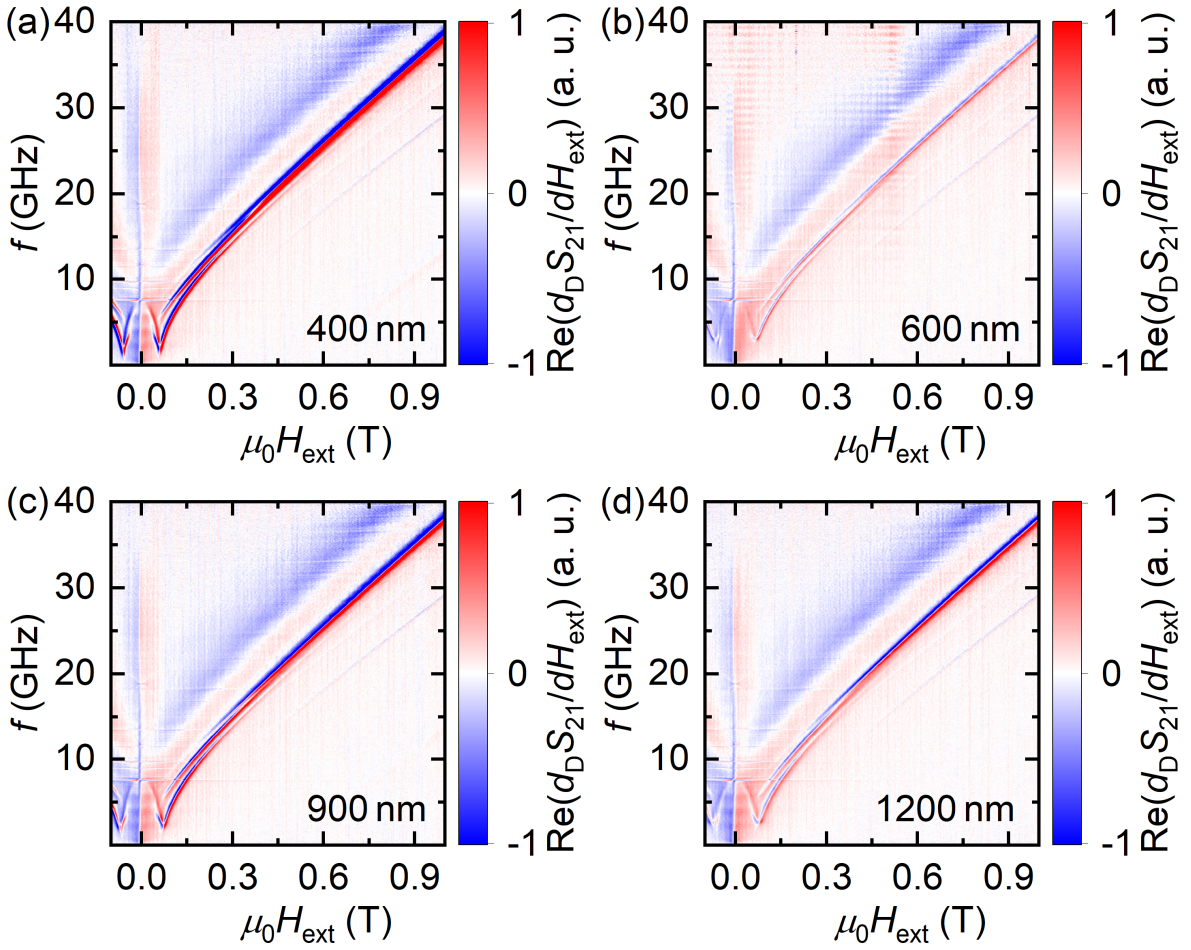

Figure 3.2.8: In-plane bbFMR data of the Py nanogratings with the external magnetic field applied perpendicular to the nanowires. The Py modes are shifted to 0.07 T, w.r.t. zero field due to the shape anisotropy of the nanowires. Two crossings of higher order modes can be spotted at 0.15 T and 0.3 T. The ESR mode of the Si substrate is also visible in all panels.

is much smaller than in the case of the CoFe nanogratings. The shift to a much lower resonance frequency compared to the CoFe nanogratings in Fig. 3.2.4 should allow for unidirectional modes to occur at lower, more accessible frequencies when used in a SW propagation device. The nanogratings with $a = 900\,\text{nm}$ and 1200 nm show a much less pronounced resonance. All colormaps additionally include a linear mode visible at around 15 GHz at an external magnetic field of 0.6 T. This mode can be identified as the paramagnetic electron spin resonance (ESR) mode of the Si substrate.

The results of in-plane bbFMR measurements with the external magnetic field applied perpendicular to the Py nanowires are depicted in Fig. 3.2.8. All colormaps show a pronounced nanograting mode shifted by approximately 0.07 T. There is no bulk-like mode starting at $\mu_0 H_{\text{ext}} = 0\,\text{T}$ as observed in the measurements of the CoFe nanogratings (cf.

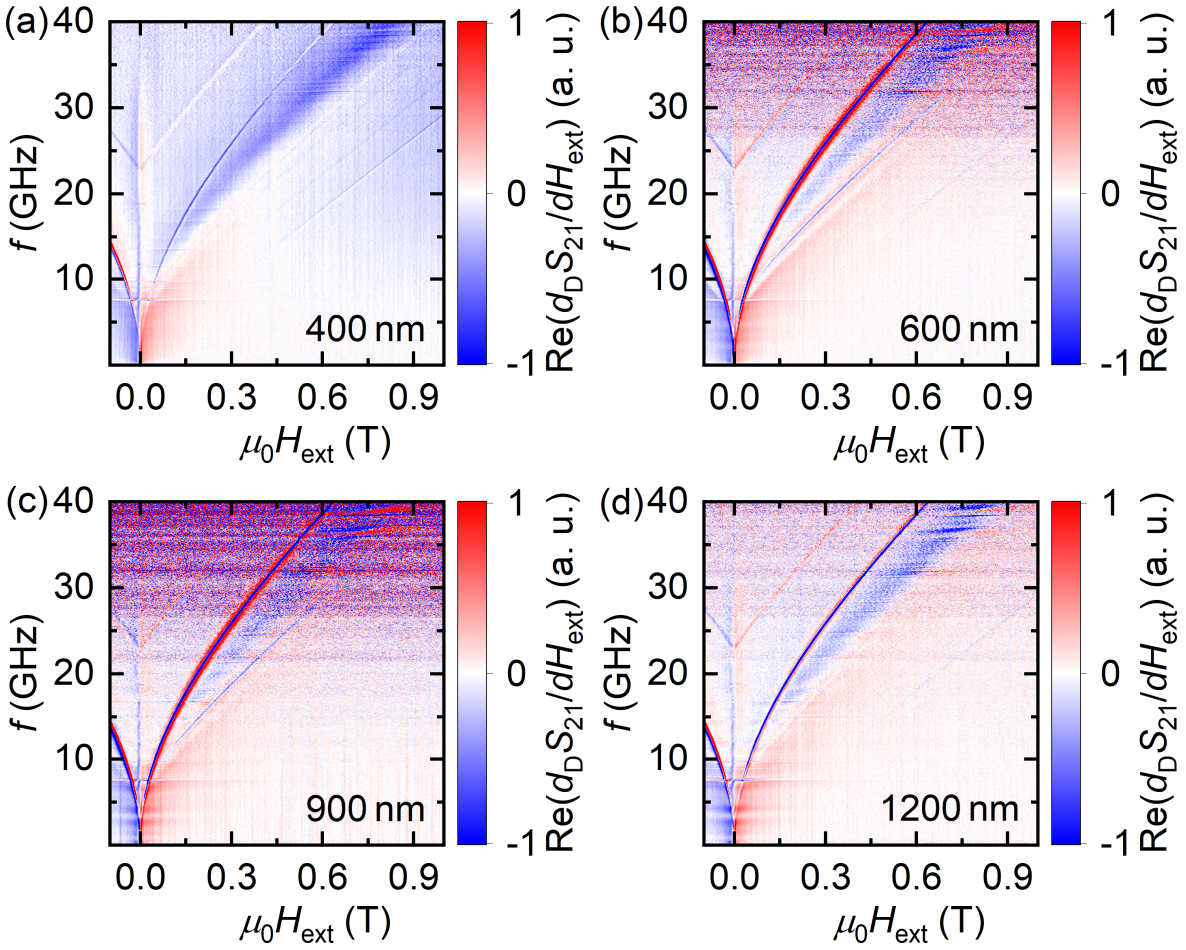

Figure 3.2.9: In-plane bbFMR data of Py nanogratings on a CoFe/AlN thin film stack with the external magnetic field directed parallel to the nanowires. Both the fundamental and a higher order CoFe mode are visible in all plots. The Py nanograting manifests in the linear mode originating at about 7.5 GHz in zero field. A faint ESR mode from the Si substrate can be spotted.

Fig. 3.2.5). Higher order modes cross the fundamental mode at about 0.15 T and 0.3 T. The linear ESR mode of the Si substrate can be spotted below the nanograting mode at frequencies of 15 GHz and above.

Additionally to the Py nanogratings fabricated on a Si substrate, Py nanogratings with the exact same layout are fabricated on top of a CoFe/AlN thin film stack. This enables a direct comparison between the FMR response of the CoFe thin film and the Py nanograting and verifies that the nanograting mode can also be efficiently driven on top of the SW propagation medium. In Fig. 3.2.9 the in-plane bbFMR measurements with the external magnetic field aligned parallel to the Py nanowires are displayed. All measurements show a distinct fundamental CoFe thin film mode starting at $\mu_0 H_{\mathrm{ext}} = 0\,\mathrm{T}$ as well as a higher order CoFe mode just below 25 GHz. The less pronounced linear mode

below the CoFe thin film mode can be identified as the Py nanograting mode. As in Figs. 3.2.7 and 3.2.8 above 15 GHz the ESR mode of the Si substrate becomes visible. The in-plane bbFMR measurement of the Py nanogratings on the CoFe/AlN stack with the magnetic field directed perpendicular to the nanowires can be found in the Appendix A.2.
With the low resonance frequency of the Kittel mode in Figs. 3.2.7 and 3.2.9 the Py nanogratings pose a good alternative to the CoFe nanogratings.

3.3 Summary

For spin wave (SW) propagation devices, magnetic materials with excellent magnetic properties such as a large effective magnetization and ultra-low spin wave damping are essential for the SW propagation medium as well as the nanograting material. To this end, the structural and magnetic properties of different CoFe multilayer stacks fabricated on thermally oxidized Si substrates by magnetron sputtering are compared using high resolution X-ray diffraction (HR-XRD) measurements and in-plane broadband ferromagnetic resonance (bbFMR) measurements, respectively. These studies revealed that a 3 nm thick Pt seed layer together with a 3 nm thick Cu buffer layer greatly enhance the structural and magnetic properties of the CoFe thin films proving that a Pt/Cu/CoFe/Cu/Ta multilayer stack is a promising material basis for SW propagation devices.
In addition to CoFe, $Ni_{80}Fe_{20}$ (Py) is used as nanograting material together with CoFe as SW propagation medium in the framework of this thesis. To achieve electrical insulation between these materials, an insulating AlN buffer layer is used. The characterization of a Py and AlN/Py multilayer hereby showed no significant difference in the structural and magnetic properties of the Py thin film in the two samples. This confirms that Py keeps its low spin wave damping and high effective magnetization when grown on AlN. Furthermore, investigations of a CoFe/AlN and a CoFe/AlN/Py multilayer stack by HR-XRD and in-plane bbFMR measurements showed that the structural and magnetic properties of the CoFe and Py are not affected when stacking them in this sequence. Therefore, a SW propagation device with CoFe as a SW medium, an AlN insulating layer and a Py nanograting was found to be a viable alternative to CoFe nanogratings on planar $Y_3Fe_5O_{12}$ (YIG) films.
To optimize the fabrication process of the magnetic nanogratings, which is based on e-beam lithography, magnetron sputtering and a subsequent lift-off process, nanogratings are fabricated with different resist recipes for the e-beam lithography step. The CSAR single layer resist recipe proved to be the most suitable recipe, with robust handling, the best pattern fidelity and minimal residue on the sample after the lift-off process.
The magnetization dynamics of CoFe nanogratings with various edge-to-edge spacings fabricated on a thermally oxidized Si substrate were investigated by in-plane and out-of-plane bbFMR measurements. With the external magnetic field directed along the wires in the sample plane, the Kittel mode of the nanogratings was found to be located above a frequency of 17 GHz and a coercivity of 40 mT was observed for the CoFe

nanogratings. The data of the in-plane measurement with the magnetic field oriented perpendicular to the wires revealed a shape anisotropy of 0.26 T. By performing out-of-plane bbFMR measurements of CoFe nanogratings with various edge-to-edge spacings between the wires, a critical wire spacing of 300 nm could be determined. Below this spacing, a stronger coupling between neighboring wires impairs the magnetic properties of the nanograting.
In-plane bbFMR data with the magnetic field applied parallel to Py wires fabricated on a thermally oxidized Si substrate with various edge-to-edge spacings showed a Kittel mode at a frequency of about 7.5 GHz with no visible coercivity, while a small anisotropy of 0.07 T is observed when the magnetic field was applied perpendicular to the wires.
Additionally, Py nanogratings were fabricated on a CoFe/AlN stack. The data of the in-plane bbFMR measurements with the magnetic field directed along the wires indicate, that the Kittel mode of the Py nanogratings can also be driven efficiently when fabricated on top of a CoFe/AlN thin film stack.
The fabrication optimization of CoFe and Py thin films as well as nanogratings discussed within this chapter enables us to investigate SW propagation devices based on CoFe and Py in the following chapters.

Chapter 4

Unidirectional Spin Wave Propagation in $Y_3Fe_5O_{12}$ Thin Films with $Co_{25}Fe_{75}$ Nanogratings

In this chapter, two spin wave (SW) propagation devices are investigated. Both devices use a $Y_3Fe_5O_{12}$ (YIG) thin film as the spin wave propagation medium and $Co_{25}Fe_{75}$ (CoFe) as the nanograting material. The devices mainly differ in the fabrication method employed for the YIG thin film. The first device is based on a 5 µm thick YIG film grown by liquid phase epitaxy (LPE) on a $Gd_3Ga_5O_{12}$ (GGG) substrate, a method that produces YIG thin films with the smallest number of impurities and thereby smallest magnetic loss [52]. The typical film thickness of YIG films grown by LPE is in the micrometer regime. This is especially relevant, as thick magnetic films can already exhibit non-reciprocal Damon-Eshbach surface SW on their own (see Sec. 2.6.1), making it more difficult to determine the origin of a possible non-reciprocity in devices with magnetic nanogratings. Thinner YIG films with a thickness of less than 100 nm and good crystalline quality can be fabricated by pulsed laser deposition (PLD). Therefore, a second device structured on a 25 nm thick YIG film grown by PLD on a GGG substrate is discussed in this chapter.
In the following, first, the magnetic properties of the YIG films grown by LPE and PLD are characterized with out-of-plane bbFMR measurements (Sec. 4.1). Afterwards, for the devices based on YIG thin films fabricated via LPE and PLD, SW propagation measurements (see Sec. 2.5 for details on the measurement method) are performed and the transmission spectra are investigated with respect to unidirectionality (Secs. 4.2 and 4.3).

4.1 Magnetic properties of $Y_3Fe_5O_{12}$ thin films fabricated by liquid phase epitaxy and pulsed laser deposition

Out-of-plane bbFMR measurements are performed at room temperature for YIG thin films deposited via LPE (LPE-YIG) and PLD (PLD-YIG) on GGG substrates before the fabrication of CoFe nanogratings. For these measurements the magnetic field is swept

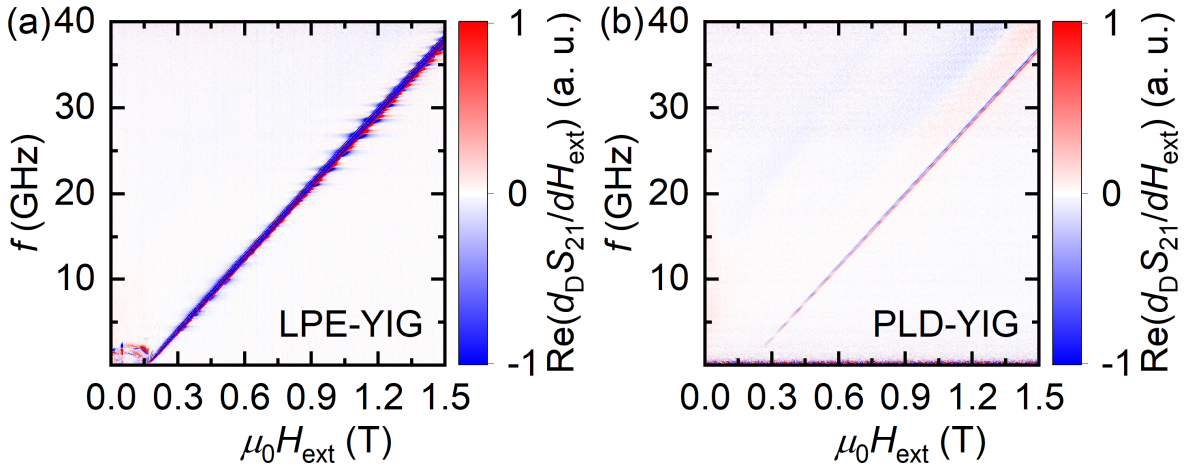

Figure 4.1.1: Out-of-plane bbFMR data recorded at room temperature for 5 µm and 25 nm thick YIG films fabricated using (a) LPE (LPE-YIG) and (b) PLD (PLD-YIG), respectively. In (a) multiple overlapping modes can be spotted that are offset from zero field by 0.15 T. In (b) a single mode, shifted by 0.2 T from zero field, is visible.

from positive to negative values and the real part of the S_{21} transmission parameter is recorded. Its background corrected value is plotted in Fig. 4.1.1. Important material parameters are extracted from the plots of both YIG thin films as discussed in Sec. 3.1.1 (see Tab. 4.1.1).

The transmission spectrum of the 5 µm thick LPE-YIG film in Fig. 4.1.1 (a) shows multiple overlapping modes exhibiting a strong FMR signal, that are offset from zero field by 0.15 T. In linecuts at a constant frequency f around the resonance field, five superimposed resonances can be identified. The dense mode spectrum inhibits the linewidth fitting procedure discussed in Sec. 3.1.1, thus preventing the extraction of the Gilbert damping α of the LPE-YIG film. However, the strong spin wave signal observed for the LPE-YIG film in Sec. 4.2 indicates that the Gilbert damping α of the thin film is sufficiently low. Previous work at WMI found $\alpha = 0.56 \cdot 10^{-3}$ for a 1 µm thick LPE-YIG film and values down to about $\alpha = 0.05 \cdot 10^{-3}$ can be found in other literature [52]. The values for $\mu_0 M_{\text{eff}}$ and g of the LPE-YIG film are comparable to previous results at WMI of $\mu_0 M_{\text{eff}} = 0.186\,\text{T}$ and $g = 2.003$ for LPE-YIG samples [45].

The transmission spectrum of the 25 nm thick PLD-YIG film in Fig. 4.1.1 (b) shows a single mode that is shifted by 0.2 T from zero field. The extracted Gilbert damping α of $2.75 \cdot 10^{-3}$ is comparable to previous results at WMI of $\alpha = 2.3 \cdot 10^{-3}$ for PLD-YIG samples [53]. However, considerably smaller values of $\alpha = 2 \cdot 10^{-4}$ were already reported in literature [52]. The effective magnetization and g-factor of the PLD-YIG film also show no significant difference to previous results [45].

Sample name	$\alpha\,(10^{-3})$	$\mu_0 M_{\mathrm{eff}}$ (T)	g
LPE-YIG	-	0.167±0.001	2.010±0.001
PLD-YIG	2.75±0.26	0.192±0.001	2.010±0.001

Table 4.1.1: Material parameters extracted from the out-of-plane bbFMR data of a 5 µm thick LPE-YIG film and a 25 nm thick PLD-YIG film (cf. Fig. 4.1.1). For the Gilbert damping α of the LPE-YIG film no value could be determined, as the dense mode spectrum prohibited reliable extraction of the linewidth as a function of the frequency.

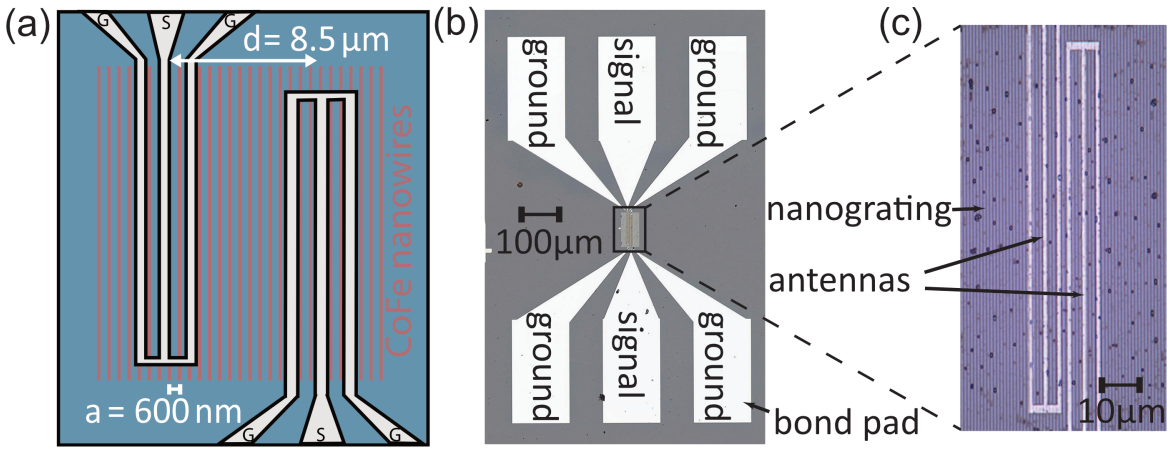

Figure 4.2.1: (a) Layout of the device patterned on a 5 µm thick LPE-YIG film. The YIG thin film is indicated as blue background on which a CoFe nanograting (red) and two aluminum antennas (white) with ground (G) and signal (S) lines are structured. The microscope image in (b) shows the three line antenna design together with bond pads. The center line (signal) is bonded to the signal line of a coplanar waveguide (CPW) and both outer lines (ground) are grounded. (c) Enlarged microscope image of the area marked by the black rectangle in (b). The dark spots on the CoFe nanograting in (c) is residue from the lift-off process.

4.2 $Co_{25}Fe_{75}$ nanogratings on YIG films fabricated by liquid-phase epitaxy

In the following, one SW propagation device structured on a 5 µm thick LPE-YIG film will be studied. Further devices on 5 µm thick LPE-YIG were investigated with similar findings. The sample design is displayed together with microscope images of the device in Fig. 4.2.1. The YIG thin film is indicated by the blue background, on which a CoFe nanograting with edge-to-edge distances between the wires of $a = 600$ nm is structured. The 200 nm wide CoFe nanowires are 100 µm long and repeated over a distance of 50 µm. For the fabrication of the nanograting the single layer CSAR resist recipe for the e-beam lithography step (see Sec. 3.2.1) is used as well as the optimized Pt/Cu/CoFe/Cu/Ta multilayer stack discussed in Sec. 3.1.1, resulting in a total height of the nanowires of about 35 nm. A second e-beam lithography step together with subsequent sputtering

and a lift-off process is carried out to define 60 nm thick aluminum antennas directly on top of the nanowires. The design of the antennas is based on the design used by Chen *et al.* in Ref. [13], where the center line of the antenna is connected to the microwave source and the outer lines are grounded. The lines of the antennas on the nanograting have a width of 1 µm. The two center lines of the antennas have an edge-to-edge distance of $d = 8.5$ µm. The microscope image in Fig. 4.2.1 (b) shows how the antennas lead to aluminum pads which are connected to a coplanar waveguide (CPW) by wire bonds. The CPW is in turn connected to a vector network analyzer (VNA).

For the SW propagation measurements, the external magnetic field is applied in the Damon-Eshbach geometry, i.e. in the sample plane parallel to the nanowires, to enable the excitation of unidirectional exchange SWs via the nanograting as described in Sec. 2.6.3. To fully saturate the magnetization of the sample, the magnetic field is first set to 1.2 T and then swept from positive to negative values. Therefore, the magnetization of the YIG film and the CoFe nanograting is aligned parallel for positive field values. As demonstrated by the bbFMR measurements in Sec. 3.2.2, the CoFe nanograting exhibits a much larger coercivity of about 40 mT than the magnetically softer YIG film due to the shape anisotropy of the nanowires. Thus, the system assumes an antiparallel configuration of the magnetization directions for negative magnetic fields down to about −40 mT. For magnetic field values below −40 mT the system returns to a parallel alignment of the magnetization directions. Furthermore, the bbFMR measurements of the CoFe nanogratings revealed that the Kittel mode of the nanowires is located at frequencies starting at around 17 GHz. Due to the dipolar coupling between the Kittel mode of the nanowires and the SWs in the YIG film, a strong enhancement of the YIG SW modes around the FMR frequency of the CoFe nanowires would be expected. Since the coupling between the nanowires and the magnetic film is chiral, an abrupt reversal of the preferred propagation direction of the enhanced YIG SW modes should be observed when the magnetization in the YIG film switches from the parallel to the antiparallel configuration. In the SW propagation measurements, the two opposing SW propagation directions are represented by the transmission spectra S_{12} and S_{21}, respectively. Hence, the YIG SW modes enhanced by the CoFe nanograting should be present in one of the transmission spectra exclusively for positive magnetic fields and in the other transmission spectrum exclusively for negative magnetic fields, as the magnetization in the YIG film switches near zero magnetic field. In the reflection spectra S_{11} and S_{22} the Kittel mode of the CoFe nanograting should be visible and exhibit discontinuities at the magnetic field values where the system switches its magnetic configuration [54].

The reflection spectra S_{11} and S_{22} as well as the transmission spectra S_{12} and S_{21} of the device structured on a 5 µm thick LPE-YIG are measured across a frequency range from 0 GHz to 30 GHz with the output level of the VNA set to +13 dBm. In Fig. 4.2.2 (a) and (b) the real part of the background corrected transmission spectra S_{12} and S_{21} are plotted. The plots show strong transmission signals starting at around 1 GHz as the antennas excite dipolar SWs in the YIG film. Both spectra also show a higher order YIG mode in the dipolar regime. The higher order YIG mode is more pronounced in S_{21} shown in Fig. 4.2.2 (b). The difference in intensity of the higher order YIG mode shows no magnetic field dependence and is also present in the reflection spectra S_{22} and

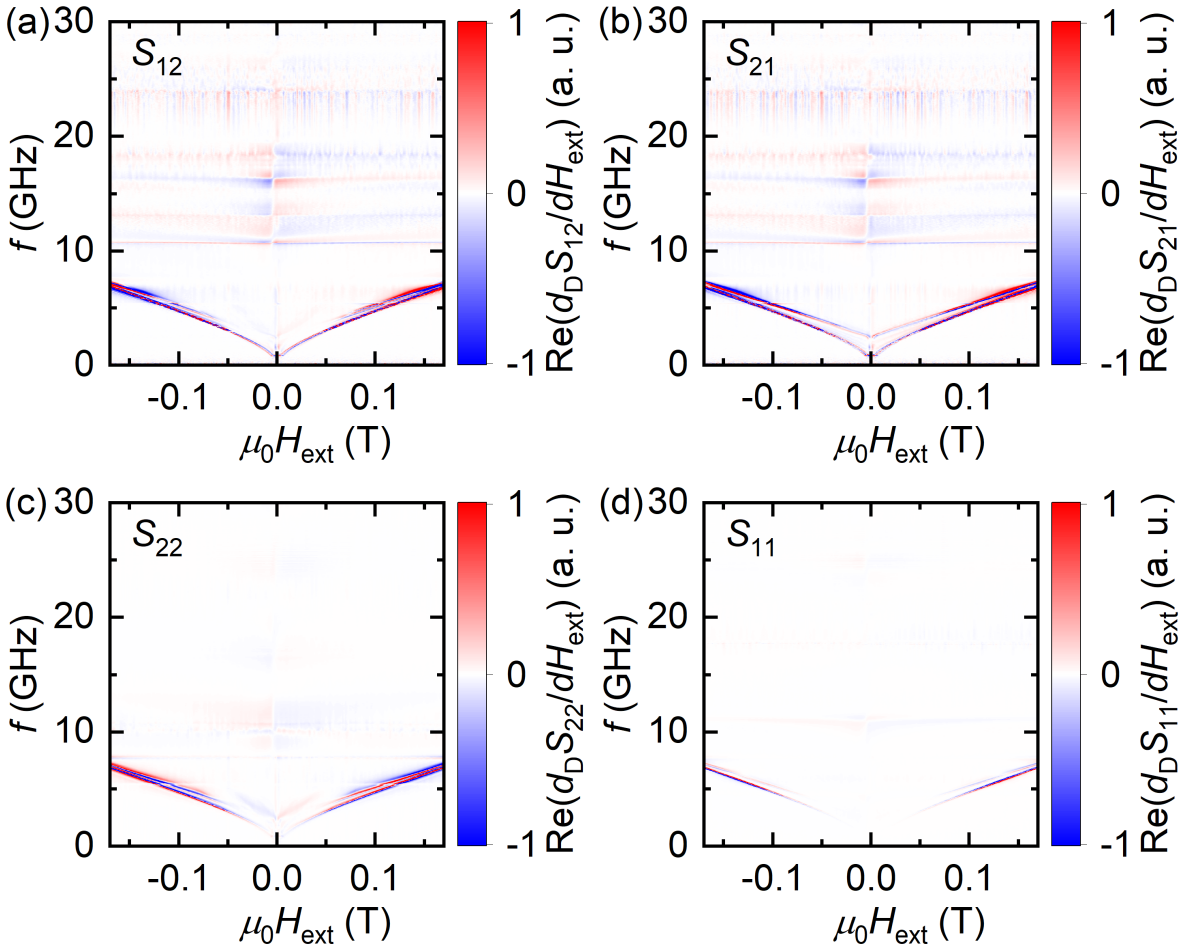

Figure 4.2.2: Background corrected transmission spectra S_{12} (a) and S_{21} (b) of a device structured on a 5 µm thick LPE-YIG thin film with an edge-to-edge spacing between the wires of $a = 600$ nm and an antenna distance of $d = 8.5$ µm. The plots show two dipolar SW modes of the YIG film being symmetric under reversal of the magnetic field direction, thus exhibiting no chirality. The difference in intensity of the higher order YIG mode when comparing both transmission spectra can be explained by a deviating excitation efficiency of the antennas, as the difference is also visible in the reflection spectra S_{22} (c) and S_{11} (d).

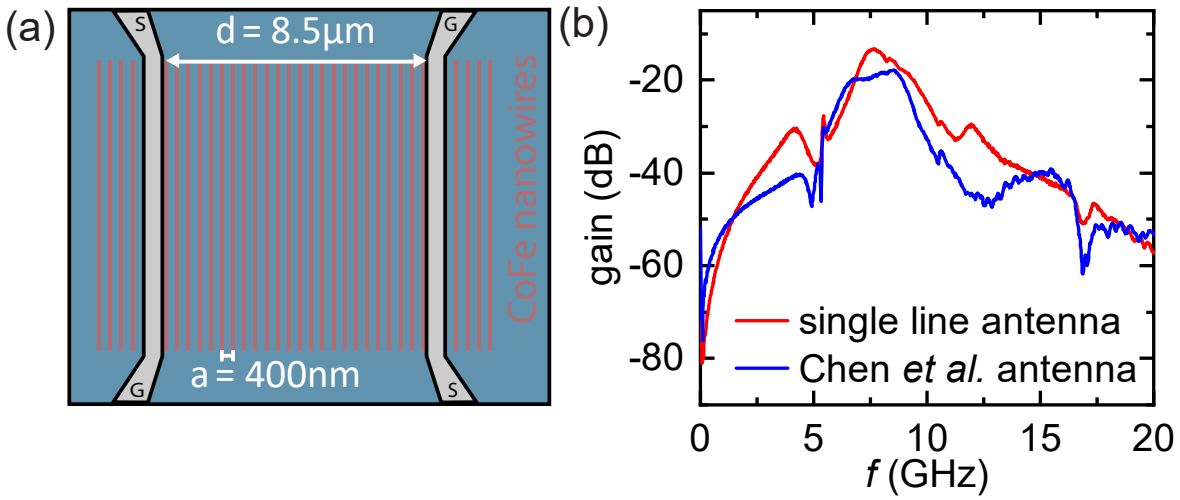

Figure 4.3.1: (a) Sample design of the device on a 25 nm PLD-YIG thin film. The device differs in the spacing between the wires ($a = 400$ nm) and the antenna design from the device on LPE-YIG. The antenna design consists of a single aluminum line with a width of 1 µm and a distance of $d = 8.5$ µm between the antennas. (b) Comparison in the power gain level as a function of frequency between the three line antenna design used by Chen *et al.* in [13] (cf. Fig. 4.2.1 (a)) and the single line antenna design shown in Fig. 4.3.1 (a).

S_{11} depicted in Fig. 4.2.2 (c) and (d), respectively. This points to a difference in the SW excitation efficiency of the two antennas, which is independent of the magnetic field and also affects the reflection spectra, since the ratio of microwave power being converted into SWs and reflected differs between the antennas.
An enhancement of the YIG mode through the coupling to the Kittel mode of the CoFe nanograting starting at around 17 GHz is not observed in the transmission spectra. The reflection spectra also show no indication of a mode associated with the CoFe nanograting.
The faint resonances above 10 GHz are related to the measurement setup and show no field dependency like SW modes. The measured signal in Fig. 4.2.2 is dominated by the YIG modes, since the magnetic volume of the 5 µm thick YIG film is much larger compared to the magnetic volume of the CoFe nanograting.

4.3 $Co_{25}Fe_{75}$ nanogratings on YIG films fabricated by pulsed-laser deposition

Figure 4.3.1 (a) shows the sample design of the device structured on a 25 nm thick PLD-YIG film grown by pulsed-laser deposition (PLD-YIG). The device studied here uses a CoFe nanograting with an edge-to-edge spacing between the wires of $a = 400$ nm and otherwise equal dimensions to the nanograting of the device discussed in Sec. 4.2. The 60 nm thick aluminum antennas consist of a single, 1 µm wide Al-line, which is less challenging in regards to impedance matching than the three line design from Chen *et*

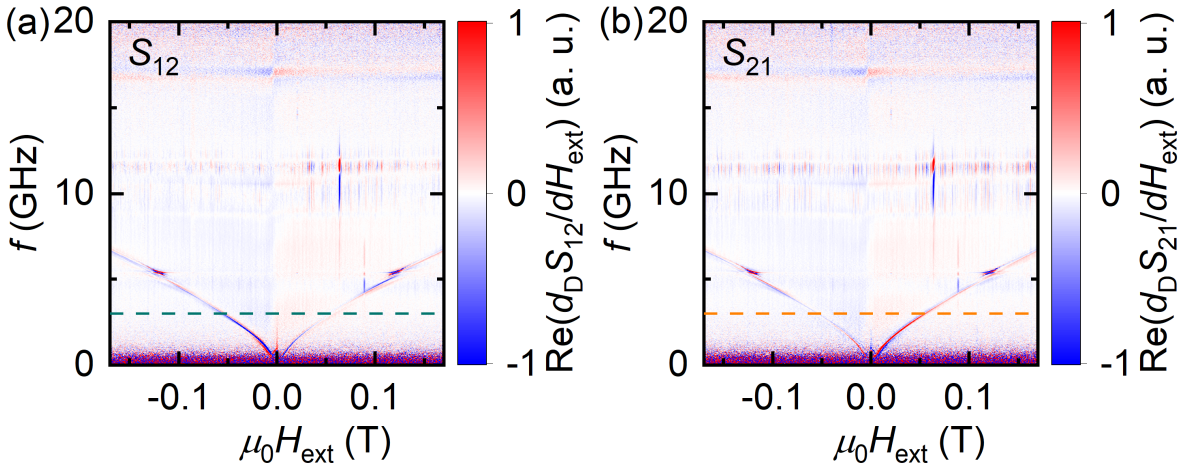

Figure 4.3.2: Background corrected transmission spectra S_{12} (a) and S_{21} (b) of a nanograting device structured on a 25 nm PLD-YIG thin film with a spacing between the wires of $a = 400$ nm and an edge-to-edge antenna distance of $d = 8.5$ µm. The plots show one dipolar spin wave mode of the YIG film and no indication of a high frequency mode being enhanced by the CoFe nanograting. The YIG mode exhibits a non-reciprocity below 5 GHz. The dashed lines indicate, where the linecuts depicted in Fig. 4.3.3 (a) are extracted.

al. used in Sec. 4.2 [55]. One end of each line is connected to the signal line of the CPW and the other end is grounded. In order to asses the performance of the new antenna design, the power gain level in decibel, i.e. $20 \log_{10}(S_{21})$, is plotted for both antennas in Fig. 4.3.1 (b) across the full frequency range at room temperature without an external magnetic field applied. The power gain level measures the output power of the device in relation to the input power and therefore how much a signal is attenuated by the device. The better impedance match of the single line antenna becomes evident by lower attenuation across large parts of the frequency band. In the SW propagation measurements the lower attenuation manifests in a better signal to noise ratio.

Fig. 4.3.2 shows the real part of the background corrected transmission spectra S_{12} (a) and S_{21} (b) of the nanograting device structured on the 25 nm PLD-YIG film for an output level of the VNA of +10 dBm. The magnetic field applied in-plane parallel to the nanowires is set to 1.2 T to fully saturate the magnetization of the sample and then swept from positive to negative values. Both plots show a low frequency dipolar spin wave mode of the YIG film and no higher order modes. As described in Sec. 2.6.3, an enhancement of the SW modes in the YIG film through the dipolar coupling to the Kittel mode of the CoFe nanograting would be expected for frequencies starting at around 17 GHz. However, there is no indication of a mode associated to the Kittel mode of the CoFe nanograting in the transmission spectra. The reflection spectra S_{11} and S_{22} included in the Appendix A.3.1 also only show the low frequency YIG mode.

The low frequency YIG mode, however, exhibits a visible non-reciprocity. Especially at frequencies below 5 GHz one of the k-vector directions is preferred for negative fields (S_{12}) and the opposing propagation direction for positive fields (S_{21}).

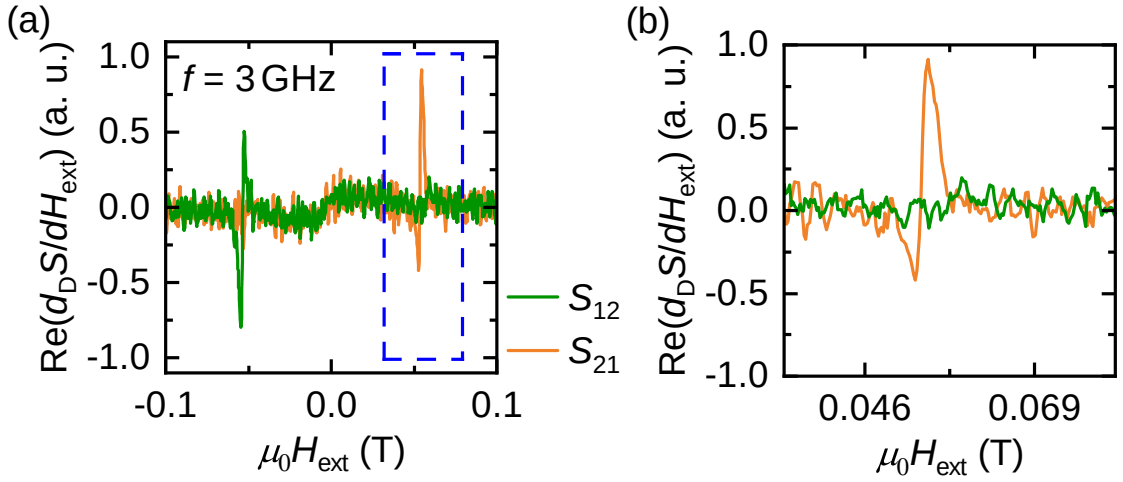

Figure 4.3.3: (a) Linecuts taken at $f = 3\,\mathrm{GHz}$ from the transmission spectra S_{12} and S_{21} of the device structured on the PLD-YIG thin film (see Fig. 4.3.2). The background corrected transmission parameters S_{12} and S_{21} show a signal at opposite field directions while otherwise remaining close to zero. Therefore, at this frequency the spin wave propagation direction depends on the direction of the external magnetic field. In (b), an enlarged view of the area circled with a dashed blue line in (a) is depicted.

In Fig. 4.3.3 (a), a linecut of S_{12} and S_{21} taken at a frequency of 3 GHz is depicted. S_{12} (S_{21}) exhibits a large signal at around $-0.05\,\mathrm{T}$ ($0.05\,\mathrm{T}$) and is otherwise close to zero amplitude. The linecut illustrates that the propagation direction of the spin waves depend on the direction of the magnetic field. Under reversal of the magnetic field the preferred k-vector direction is also reversed. The non-reciprocity present in the low frequency regime could be explained by the inherently unidirectional propagation of magnetostatic surface spin waves in the Damon-Eshbach geometry, as discussed in Sec. 2.6.1. This effect is more pronounced in thicker magnetic films, but evidence for a Damon-Eshbach induced non-reciprocity in magnetic films with a thickness of 20 nm exists [35]. Another possible origin of the observed non-reciprocity is an interfacial Dzyaloshinskii-Moriya interaction (iDMI, cf. Sec. 2.6.2) at the interface of the GGG substrate and the YIG thin film, as reported in Ref. [11]. However, in previous experiments at WMI a non-reciprocity in thin YIG films due to an iDMI at the GGG/YIG interface could not be confirmed.

4.4 Summary

The magnetic properties of a 5 µm thick $Y_3Fe_5O_{12}$ (YIG) film grown by liquid phase epitaxy (LPE-YIG) and a 25 nm thick YIG film grown via pulsed-laser deposition (PLD-YIG) were investigated with out-of-plane broadband ferromagnetic resonance (bbFMR) measurements. The material parameters of both thin films were extracted from the bbFMR data and were comparable to previous results obtained at WMI.

A spin wave (SW) propagation device structured on a 5 µm thick LPE-YIG film with an antenna distance of 8.5 µm and a $Co_{25}Fe_{75}$ (CoFe) nanograting with an edge-to-edge distance of 600 nm between the wires was studied by performing spin wave propagation measurements. In the transmission spectra two low frequency spin wave modes of the YIG film could be observed and no evidence for a high frequency mode enhanced by the nanograting was found.
For the device structured on the 25 nm thick PLD-YIG film a new single line antenna design was utilized and a nanograting with a smaller edge-to-edge distance of 400 nm between the wires. This design showed less attenuation than the antenna design by Chen *et al.* [13] used for the device on LPE-YIG. The transmission spectra of the spin wave propagation measurement for the device on PLD-YIG contained a single low frequency YIG mode and no mode associated with the CoFe nanograting. A non-reciprocity could be observed in the YIG mode for frequencies below 5 GHz and might be associated to unidirectional propagation of magnetostatic surface spin waves or to non-reciprocity in YIG films due to an interfacial Dzyaloshinskii-Moriya interaction at the interface to the GGG substrate. However, further measurements are needed to investigate this non-reciprocity in more detail.

Chapter 5

Unidirectional Spin Wave Propagation in $Co_{25}Fe_{75}$ Thin Films with $Ni_{80}Fe_{20}$ Nanogratings

In the following chapter, all-metallic spin wave (SW) propagation devices with $Co_{25}Fe_{75}$ (CoFe) as the spin wave medium are discussed. Therefore, two devices with $Ni_{80}Fe_{20}$ (Py) nanogratings are each compared to respective devices without nanogratings. Here, solely Py nanogratings with an edge-to-edge distance of 500 nm are used, as the nanogratings with larger spacings exhibit rather weak ferromagnetic resonance (FMR) signals (cf. Fig. 3.2.7). Devices with a distance between the antennas of 2 µm and 8.5 µm are investigated by SW propagation measurements. Thereby, the external magnetic field is applied in the Damon-Eshbach geometry, i.e. in the sample plane perpendicular to the SW propagation direction.
For devices with nanogratings this should enable the chiral pumping of SWs (cf. Sec. 2.6.3) by exciting the Kittel mode of the nanowires. The bbFMR measurements of the Py nanogratings in Sec. 3.2.3 revealed that the Kittel mode of the nanowires is located at frequencies above 7.5 GHz. Hence, an enhanced non-reciprocity of the CoFe SW modes starting at around 7.5 GHz would be expected for the devices with a Py nanograting. Furthermore, a very small coercivity of the Py nanogratings was found as the magnetization of the nanowires switched near zero field. Thus, the magnetizations of the Py nanograting and the underlying CoFe thin film remain aligned in parallel during the SW propagation measurements.
For the SW propagation measurements, the magnetization of the sample is first fully saturated by applying a magnetic field of 1.2 T. The magnetic field is then swept from positive to negative values and the transmission spectra S_{12} (S_{21}) and reflection spectra S_{11} (S_{22}) are measured with a vector network analyzer (VNA) at an output level of 10 dBm. The data is background corrected with the derivative divide method (see Sec. 2.4 and Ref. [29]) and the real part of the complex S parameters is plotted as a function of the frequency f and the external magnetic field $\mu_0 H_{\text{ext}}$. The transmission spectra are studied in detail by taking linecuts from the colormaps at constant frequencies and extracting chirality ratios between the two field directions (cf. Sec. 5.1). Finally, the most important results are summarized in Sec. 5.2.

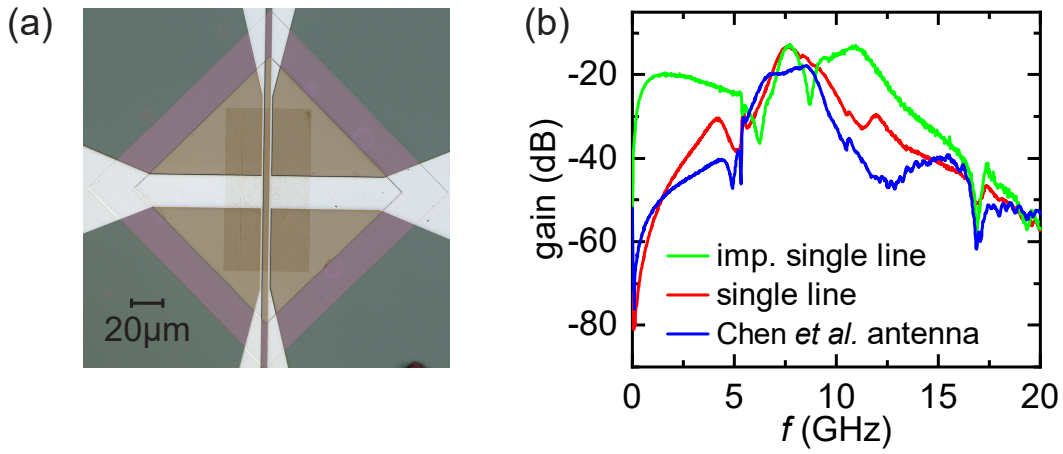

Figure 5.1.1: (a) Microscope image depicting the sample layout of an all-metallic spin wave propagation device. The CoFe waveguide (brown) is covered with an AlN layer (violet). The faint darker brown rectangle in the center of the image is a Py nanograting structured on top of the AlN. The aluminum antennas depicted in white are connected at the top and bottom leads for the measurements in this chapter. (b) Power gain level as a function of frequency for the original three-line antenna design of Chen *et al.* in Ref. [13] (blue), the single-line antenna design used in Sec. 4.3 (red) and the improved single line antenna design (green) as shown in (a).

5.1 All-metallic spin wave propagation devices

Figure 5.1.1 (a) shows a microscope image illustrating the sample design employed for all devices discussed in this chapter. The thermally oxidized Si substrate on which the devices are structured, is depicted as the olive background in the picture. The 35 nm thick Pt/Cu/CoFe/Cu/Ta multilayer stack (cf. Sec. 3.1.1) used as the SW medium of the devices is structured into a waveguide, visible as a brown diamond in the center of the image. The waveguide predefines the propagation direction of the SWs, improving the efficiency of the devices [56]. To avoid reflection of SWs at the edges of the CoFe waveguide, two of the waveguide corners are aligned along the SW propagation direction [57]. The latter is defined as the propagation of SWs from the left to the right antenna (and vice versa) depicted in white in Fig. 5.1.1 (a).
As mentioned in Sec. 3.1.2, the CoFe is covered with an 35 nm thick AlN insulating layer to avoid electrical shorts with the metallic Py nanograting as well as between the Al antennas. With a side length of 150 µm the diamond-shaped AlN cover is larger than the underlying CoFe waveguide with a side length of 110 µm, which manifests in the violet edge in the image in Fig. 5.1.1 (a), where there is no CoFe below the AlN. This guarantees electrical insulation even at the edges of the CoFe waveguide and provides support for the 60 nm thick aluminum antennas to cover the 70 nm height difference from the substrate onto the device.
In the center of the image a Py nanograting can be seen as a faint darker brown rectangle.

The Py nanowires have a length of 100 µm and are repeated over a length of 50 µm. The width of the Py wires in the sample layout is reduced to 150 nm in comparison to the 200 nm wide CoFe wires in Chap. 4. This counteracts the more prominent broadening effects due to a higher base dose of 2.4 C/m^2 being used during the lithography step of the Py nanogratings instead of 2 C/m^2 that were used for the CoFe nanogratings in Chap. 4. The higher base dose leads to a cleaner lift-off process with less residue left on the sample from insufficiently exposed resist. The resist recipe used for the fabrication of the Py nanogratings is still the single-layer CSAR resist recipe discussed in Sec. 3.2.1. For devices without a nanograting on top of the AlN layer, the fabrication of the nanograting is omitted while the rest of the sample design remains unaltered.
The aluminum antennas, pictured in white in Fig. 5.1.1 (a), are an improved version of the Al single line antenna design previously used in Sec. 4.3. Immediately noticeable is a third connection with a width of 20 µm added at a 90° angle midway along the 1 µm wide single line. This third connection however only serves as a backup in case of a damaged antenna and is not used here. For the measurements shown in this chapter the antennas are connected either at the top or at the bottom end to the signal line of the CPW and grounded at the opposing end. More importantly, the new Al antenna design differs on how the 1 µm single line antennas are connected to the bond pads at the top and bottom end of the image. In contrast to the previous design, the connection to the bond pads is not angled but is achieved by a steady broadening of the aluminum line leading towards the pads. This further reduces the attenuation of the antennas as illustrated by the graph of the power gain level ($20 \log_{10}(S_{21})$) as a function of frequency in Fig. 5.1.1 (b). The graph of the new, improved design, depicted in green, surpasses both the three line design used by Chen *et al.* in Ref. [13] (blue, for details on the design cf. Sec. 4.2) as well as the single line design (red) used in S ec. 4.3 across most of the frequency band.
In the following, devices with an edge-to-edge distance of 2 µm and 8.5 µm between the antennas are discussed by comparing a device with a Py nanograting to the respective device without a nanograting.

5.1.1 All-metallic spin wave devices with 2 µm antenna distance

Figure 5.1.2 shows the transmission spectra of a device without a nanograting in (a)-(b) and with a Py nanograting in (c)-(d). Hereby, the edge-to-edge distance between the respective antennas is $d = 2$ µm and the edge-to-edge distance between the wires of the device with a Py nanograting is $a = 500$ nm. Three faint CoFe spin wave modes are visible in the transmission spectra of the device without a nanograting. The modes exhibit a weak non-reciprocity, especially above frequencies of 15 GHz where the amplitude of S_{12} is enhanced at positive fields and the amplitude of S_{21} at negative fields. In (c) and (d), for the device with a Py nanograting, the same three CoFe SW modes appear with a higher intensity. Likewise, the CoFe modes are slightly non-reciprocal above frequencies of 15 GHz. Additionally, a very faint mode with a flatter dispersion emerges at a frequency of 12 GHz, highlighted with arrows in the plot. This mode can be identified as the Kittel mode of the Py nanograting as it matches the dispersion of the Py nanograt-

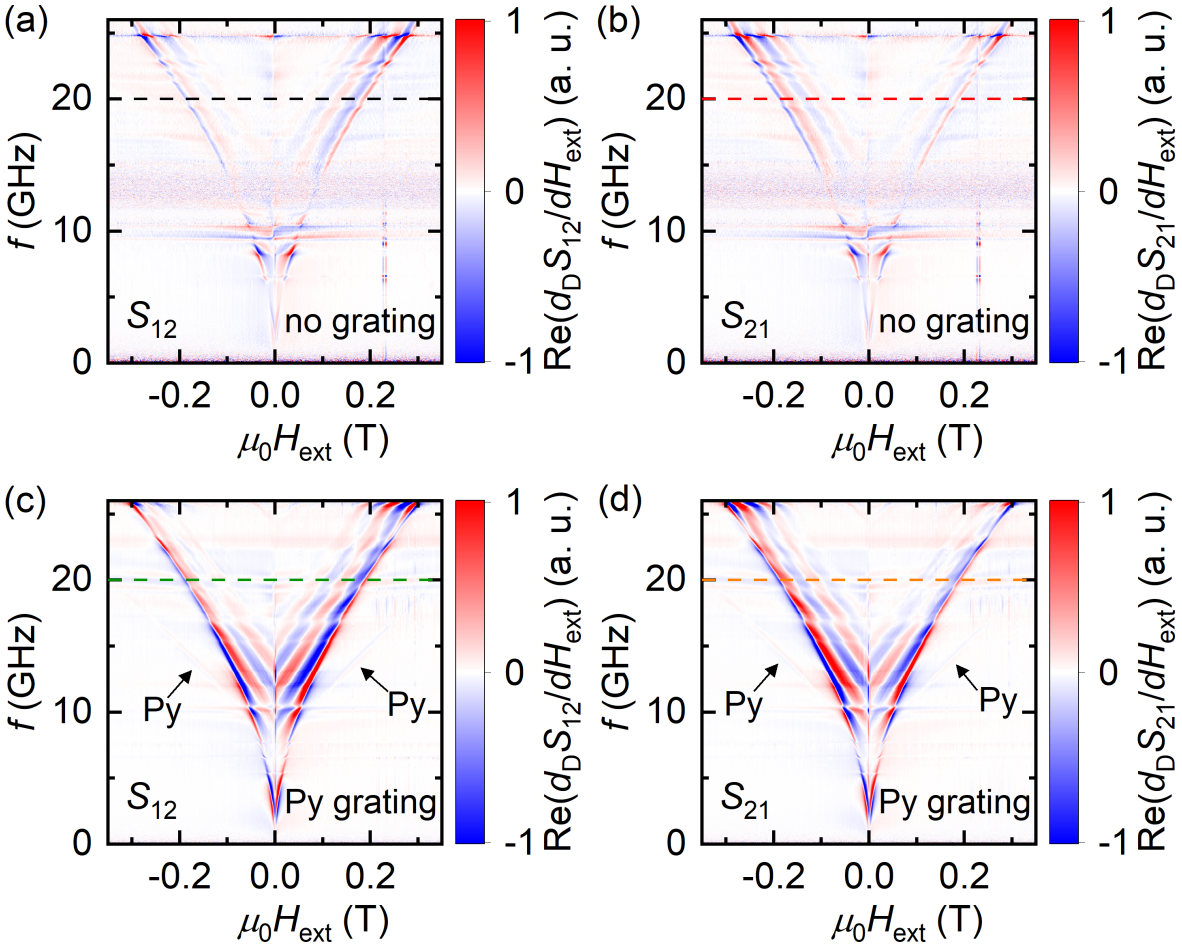

Figure 5.1.2: Transmission spectra (background corrected S_{12} and S_{21}) of the all-metallic CoFe/Py SW propagation devices with an edge-to-edge distance of 2 µm between the Al antennas. The plots of the device without a nanograting in (a)-(b) show three CoFe spin wave modes that exhibit a weak non-reciprocity above approx. 15 GHz. The colormaps of the device with a Py nanograting (c)-(d) show the same CoFe modes with a higher amplitude. Additionally, a faint mode of the Py nanograting is visible (highlighted by black arrows). The dashed lines indicate, where the linecuts depicted in Fig. 5.1.3 are extracted.

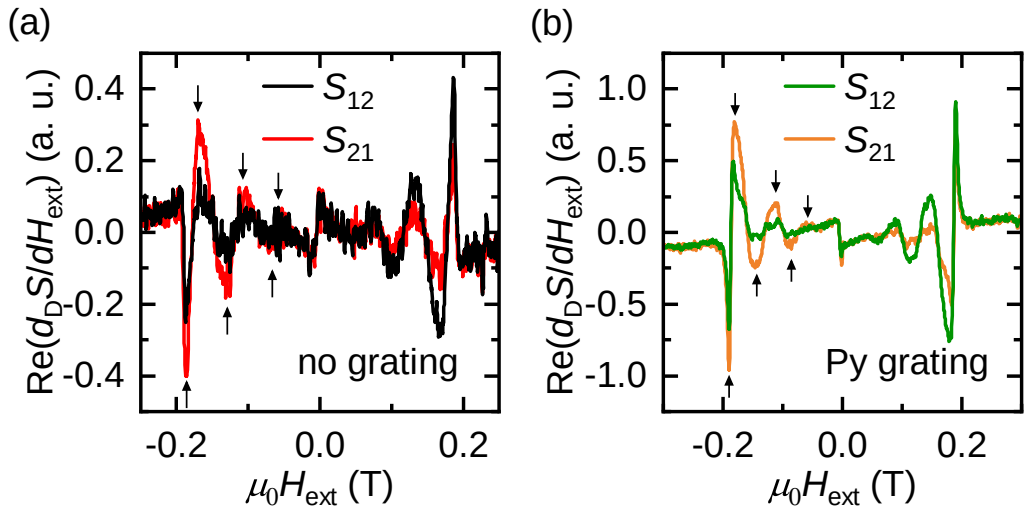

Figure 5.1.3: Linecuts taken from the transmission spectra in Fig. 5.1.2 at a frequency of 20 GHz of the sample (a) without a nanograting and (b) with a Py nanograting. The three CoFe modes visible in the transmission spectra can be seen as three adjacent maxima and minima (highlighted by the black arrows) in the linecuts in both field directions. The slight non-reciprocity visible in the transmission spectra of both samples manifests as a difference in amplitude of the background corrected S_{12} and S_{21} at negative and positive magnetic fields.

ing mode observed in the bbFMR measurements in Sec. 3.2.3. The noticeable difference in the intensity of the CoFe SW modes between the two devices can not be ascribed to the Py nanograting, as the device with a Py nanograting exhibits a larger signal even at frequencies below 7.5 GHz, where the Kittel mode of the Py nanograting is not excited. Instead, the larger signal to noise ratio of the data from the device with a Py nanograting is likely due to deviations in the material characteristics. For the reflection spectra S_{11} and S_{22} of both devices it is referred to the Appendix A.3.2.
In (a)-(d), there are crossings visible in the lowest order CoFe SW mode for frequencies between 5 GHz and 12 GHz. Therefore, the crossings in (c)-(d) are not necessarily associated with the intersection of the Py nanograting mode with the CoFe SW mode. At $f < 10$ GHz, where the CoFe SW modes and the Py nanograting mode ought to lie on top of each other, there is also no apparent effect on the dispersion of the CoFe mode visible for the device with an additional Py nanograting. In summary, there is no clear evidence found in the transmission spectra for an interaction between the Py nanograting mode and the CoFe SW modes.

In order to compare the non-reciprocal behavior observed in both samples, a linecut of the transmission spectra in Fig. 5.1.2 at a frequency of 20 GHz is taken and depicted in Fig. 5.1.3. The transmission parameters of the sample without a nanograting in Fig. 5.1.3 (a) and with a Py nanograting in Fig. 5.1.3 (b) show three CoFe modes for both field directions, as already seen in the colormaps in Fig. 5.1.2. The larger amplitude in the transmission spectra of the sample with a nanograting manifests in a better signal to

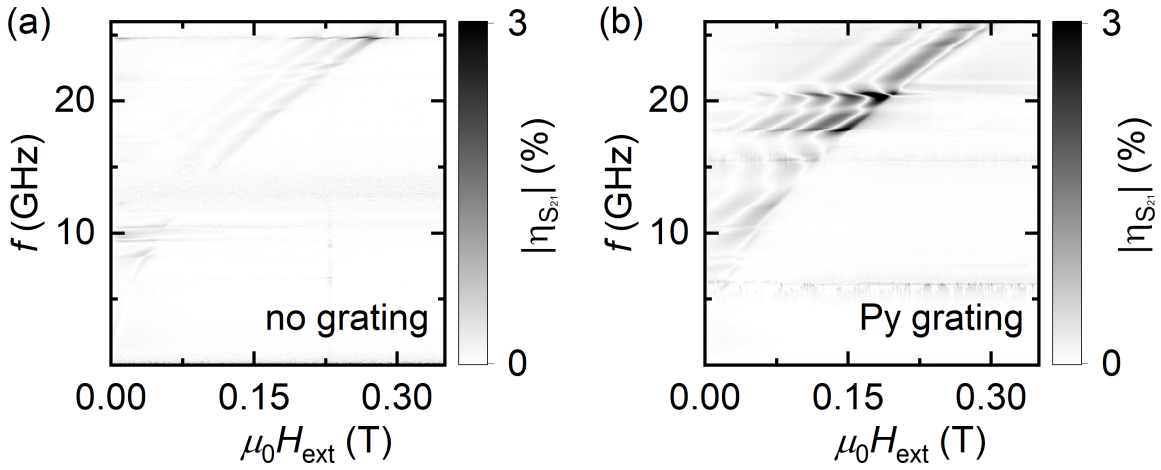

Figure 5.1.4: Non-reciprocity ratio $|\eta_{S_{21}}|$ as a function of the frequency f and external magnetic field $\mu_0 H_{\text{ext}}$ for devices with an antenna distance of 2 µm. $|\eta_{S_{21}}|$ is extracted from the transmission spectra depicted in Fig. 5.1.4 (b) and (d) (see Eq. (5.1)). (a) The device without a nanograting exhibits three CoFe SW modes that are faintly visible, underlining the presence of a weak non-reciprocity in all three modes. (b) The device with a Py nanograting reveals more pronounced CoFe SW modes, indicating that their non-reciprocity is slightly stronger with a maximum value of about $|\eta_{S_{21}}| = 3\%$.

noise ratio in (b). The non-reciprocity of the CoFe modes becomes apparent in both graphs as a difference in the amplitude of the S-parameters. The S-parameter and therefore SW propagation direction exhibiting a larger signal depends on the orientation of the external magnetic field. The relative difference in amplitude between S_{12} and S_{21} in (a) and (b) is similar, indicating that the non-reciprocity is not greatly affected by the Py nanograting.

As already mentioned above, the magnetizations of the Py nanograting and the CoFe thin film both switch directions near zero magnetic field due to their small coercivities. Hence, the reversal of the magnetic field is geometrically equivalent to the reversal of the SW propagation direction for the devices studied in this chapter. By investigating the non-reciprocity of the transmission spectrum under reversal of the magnetic field rather than under reversal of the SW propagation direction, any contribution stemming from a difference of the Al antennas is eliminated. Therefore, the non-reciprocity of the SW modes in Fig. 5.1.2 can be quantified by the ratio

$$\eta_{S_{21}} = \frac{S_{21}(H_{\text{ext}}) - S_{21}(-H_{\text{ext}})}{S_{21}(H_{\text{ext}}) + S_{21}(-H_{\text{ext}})}. \tag{5.1}$$

An equivalent formula can be defined for S_{12}. For perfectly unidirectional transport the ratio assumes the value $|\eta| = 1$. By plotting $|\eta|$ as a function of the frequency and the external magnetic field, the non-reciprocity of the transmission spectra can be visualized. This is shown in Fig. 5.1.4 for the S_{21} transmission spectrum of the device without a nanograting (a) and with a Py nanograting (b). The equivalent plots for S_{12} are not

shown here, as there are no significant differences in $|\eta|$ of S_{12} and S_{21} for both devices. The plots in Fig. 5.1.4 clearly reflect the increase in chirality for frequencies above 15 GHz. The three CoFe spin wave modes can be distinguished in the plot, indicating that all of the modes exhibit a slight non-reciprocity with a maximum value of about $|\eta_{S_{21}}| = 3\%$.
The weak non-reciprocity observed for both devices might be due to the inherently non-reciprocal propagation found in magnetostatic surface spin waves (MSSWs), as discussed in Sec. 2.6.1. The effect scales down with decreasing layer thickness, but is well documented for Py films even with a smaller thickness than the CoFe film used here [58, 59]. A strong enhancement of the unidirectionality in the frequency range of the nanograting mode as reported in Ref. [13] can not be observed.

5.1.2 All-metallic spin wave devices with 8.5 µm antenna distance

In Fig. 5.1.5 the transmission spectra of the devices with an edge-to-edge distance between the antennas of $d = 8.5\,\mu m$ are shown. The plots of the device without a nanograting in (a)-(b) show eight CoFe spin wave modes that are especially pronounced at frequencies between 8 GHz and 17 GHz. In this frequency range a weak non-reciprocity is visible, as the CoFe modes exhibit a slightly larger amplitude for positive magnetic fields in S_{12} (see Fig. 5.1.5 (a)) and for negative magnetic fields in S_{21} (see Fig. 5.1.5 (b)).
The transmission spectra in (c)-(d) of the device with a Py nanograting also reveal eight distinct CoFe modes. Hereby, the edge-to-edge distance between the wires is $a = 500\,nm$. Taking into account the measurements of devices with an antenna distance of $d = 2\,\mu m$ (cf. Sec. 5.1.1) and $d = 1\,\mu m$ (see Appendix A.3.4), the number of possible SW modes in the CoFe waveguide roughly scales with d. The transmission spectra in Fig. 5.1.5 (c)-(d) show a clearly visible non-reciprocity with S_{12} being preferred for positive field values and S_{21} for negative values. The non-reciprocity persists across the entire frequency range. A faint mode related to the Py nanograting is highlighted in both transmission spectra. The Py nanograting mode intersects the lowest order CoFe mode at approximately 9 GHz leading to a slight deviation of the CoFe mode from the dispersion observed in (a)-(b) for the device without a Py nanograting. In the frequency range below 9 GHz, where the Py nanograting mode and CoFe SW modes lie on top of each other, no significant effect of the Py nanograting mode becomes apparent. For the reflection spectra S_{11} and S_{22} of both devices it is referred to the Appendix A.3.3.

The large amplitude across the entire frequency range in Fig. 5.1.5 (c)-(d) allows for a precise extraction of the SW resonance frequency as a function of the external magnetic field. By subsequently fitting the Kalinikos-Slavin equation (see Sec. 2.5 Eq. (2.31)) to the data, the k-vector and thereby the wavelength λ associated with the respective SW mode can be determined. As the terms related to the exchange interaction in the Kalinikos-Slavin equation are negligibly small here, they are omitted. In the Damon–Eshbach geometry (see Sec. 2.5 Fig. 2.5.2) the spin wave dispersion can then be

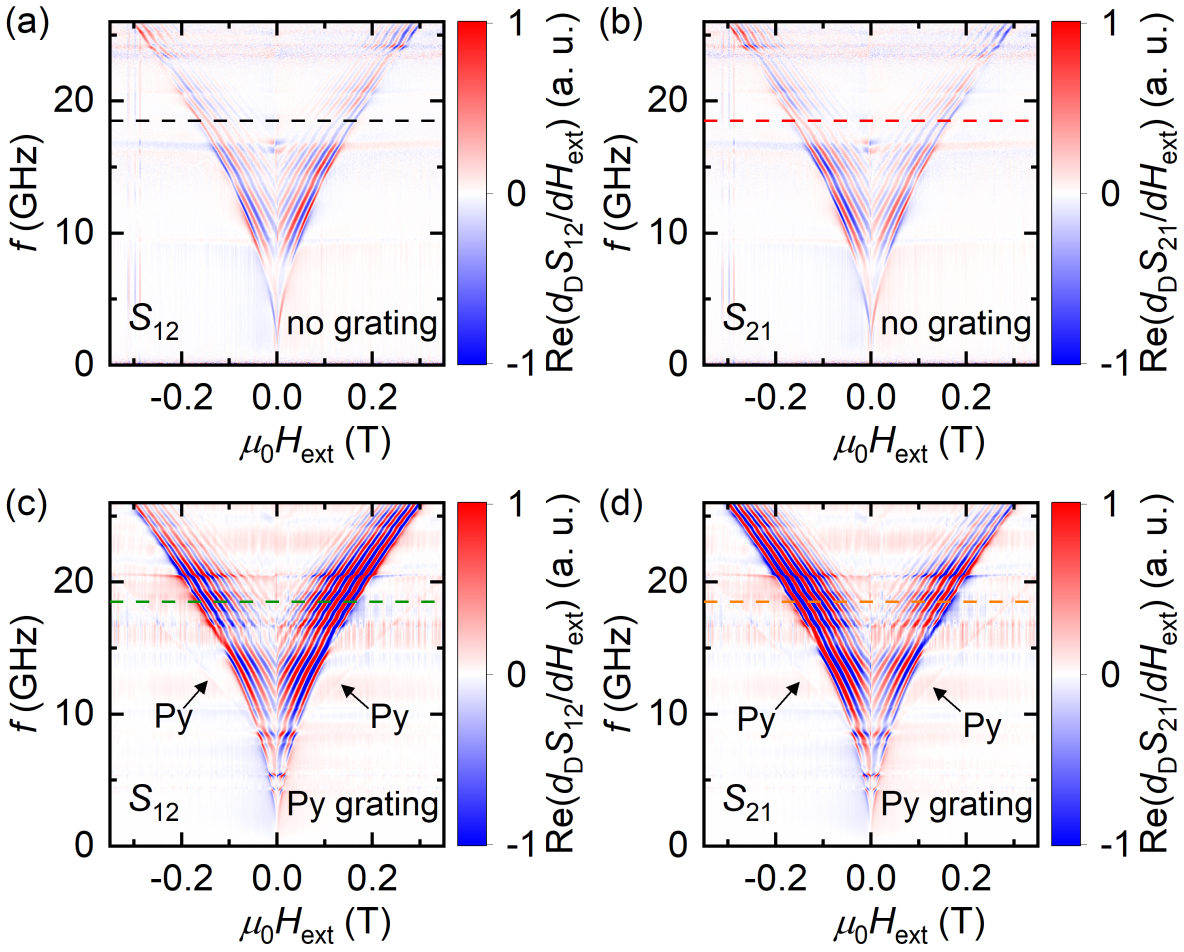

Figure 5.1.5: Background-corrected transmission spectra from SW propagation measurements of devices with an edge-to-edge distance d of 8.5 µm between the antennas. The spectra of the device without a nanograting in (a)-(b) show a weak non-reciprocal behavior in the CoFe SW modes between around 8 GHz and 17 GHz. The graphs of the device with a Py nanograting in (c)-(d) feature similar CoFe SW modes with a larger amplitude and stronger non-reciprocity. Additionally, a mode related to the Py nanograting is observed and highlighted in the spectra. The dashed lines indicate, where the linecuts depicted in Fig. 5.1.7 are extracted.

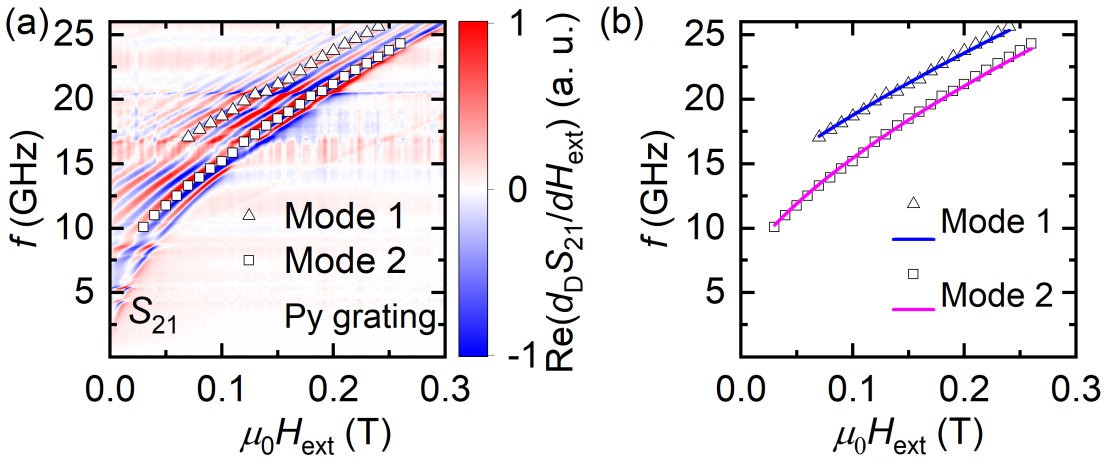

Figure 5.1.6: (a) Background-corrected transmission spectrum of S_{21} of the device with a Py nanograting for positive magnetic fields. Exemplarily, at the points indicated by the white symbols, the SW resonance frequency is extracted together with the corresponding resonance field. (b) The obtained data points for the two modes (open symbols) are fitted with Eq. (5.2) as shown by the solid lines.

described by [35]

$$\omega = |\gamma|\mu_0\sqrt{H_{\mathrm{ext}}(H_{\mathrm{ext}}+M_{\mathrm{S}})+M_{\mathrm{S}}^2(1-e^{-2|k_y|t_{\mathrm{FM}}})/4}, \tag{5.2}$$

where k_y denotes the component of the in-plane wavevector perpendicular to the magnetization and t_{FM} the thickness of the SW medium. Figure 5.1.6 (a) shows exemplary data sets extracted from two of the SW modes in the S_{21} transmission spectrum in Fig. 5.1.5 (d). For the fits depicted in Fig. 5.1.6 (b), the parameters $t_{\mathrm{FM}} = 35\,\mathrm{nm}$ and $\mu_0 M_{\mathrm{S}} = 2.3\,\mathrm{T}$ are used. The fit of the first mode (green) yields a wavelength of $\lambda_1 = (2.56 \pm 0.03)\,\mu\mathrm{m}$ whereas fit of the second mode (orange) gives a wavelength of $\lambda_2 = (8.94 \pm 0.24)\,\mu\mathrm{m}$. The wavelengths of the other modes observed in the transmission spectra range from $\lambda \approx 17\,\mu\mathrm{m}$ for the lowest frequency mode to $\lambda \approx 1.3\,\mu\mathrm{m}$ for the highest frequency mode. Since the transmission spectra of the device without a nanograting in Fig. 5.1.5 (a)-(b) exhibit the same CoFe SW modes, there is no significant difference in the wavelength of the modes of the devices with or without a Py nanograting. With the smallest wavelength well above $1\,\mu\mathrm{m}$, the SWs excited in the devices are all in a regime where the dispersion is dominated by the dipolar field of the SW.

To further investigate the non-reciprocity of the CoFe modes, linecuts are taken from the transmission spectra shown in Fig. 5.1.5 at a frequency of 18.5 GHz and depicted in Fig. 5.1.7 (a) for the device without a nanograting and in (b) for the device with a Py nanograting. The plots show seven CoFe modes for both orientations of the external magnetic field. The weak non-reciprocity observed for the device without a nanograting manifests in a very small difference between the amplitude of the background-corrected S_{12} and S_{21} in (a). The graph in (b) visualizes the larger amplitude and stronger non-

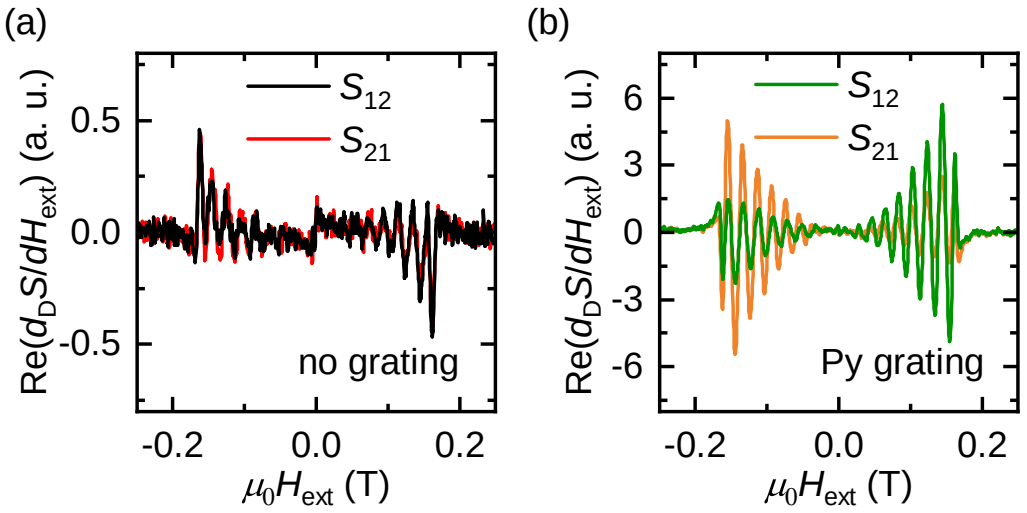

Figure 5.1.7: Linecuts taken at a frequency of 18.5 GHz from the transmission spectra shown in Fig. 5.1.5. Seven distinct CoFe modes are visible. The device without a nanograting exhibits a weak non-reciprocity in the transmission spectra with only small differences between the amplitudes of the background-corrected S-parameters (a). The more pronounced non-reciprocity observed for the device with a Py nanograting is reflected by the strong asymmetry of the amplitudes of the background-corrected S-parameters (b).

reciprocity observed for the CoFe modes of the device with a Py nanograting.

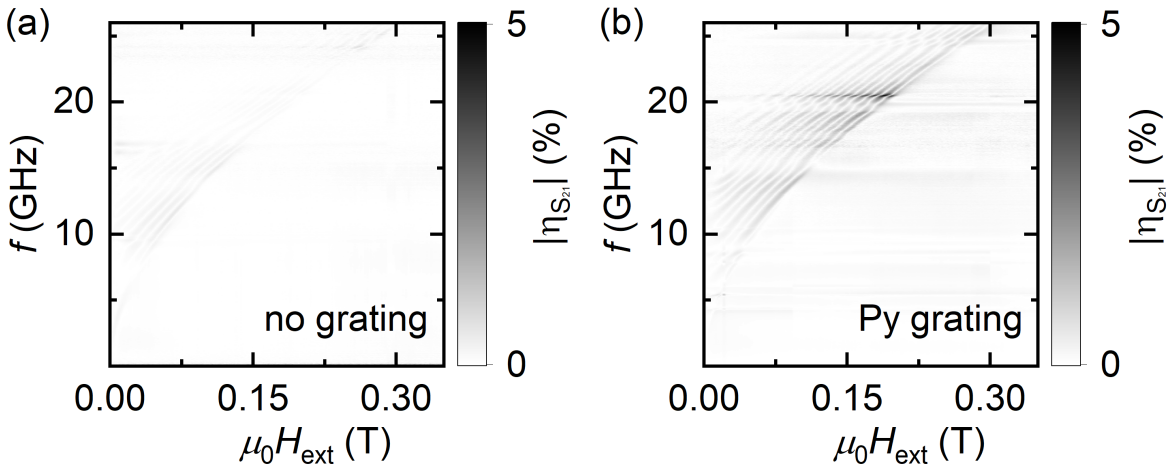

Figure 5.1.8: Absolute value of the ratio $\eta_{S_{21}}$ as a function of the frequency f and external magnetic field $\mu_0 H_{ext}$ for the background corrected S_{21} transmission spectra of the devices with a distance of 8.5 µm between the antennas. (a) The device without a nanograting exhibits weak non-reciprocity of the CoFe modes in a frequency range between 10 GHz and 17 GHz. (b) The stronger non-reciprocity observed in the device with a Py nanograting manifests in the clearly visible CoFe modes across the measured frequency range.

Furthermore, with Eq. (5.1), the non-reciprocity ratio $|\eta_{S_{21}}|$ is calculated and plotted as a function of frequency and external magnetic field for the device without a nanograting in Fig. 5.1.8 (a) and for the device with a Py nanograting in (b). In (a), the CoFe modes are faintly visible between 8 GHz and 17 GHz, indicating the presence of a slight non-reciprocity. In (b), all of the CoFe modes seen in the colormaps of the device with a Py nanograting are continuously mapped out, underlining that the non-reciprocal behavior is not limited to a small frequency band but present across the entire measurement range. However, with a maximum ratio of $|\eta_{S_{21}}| = 5\%$ the effect is still rather small.
As already discussed in Sec. 5.1.1, the weak non-reciprocal behavior of the devices can be traced back to the inherently unidirectional propagation of magnetostatic surface spin waves (see Sec. 2.6.1). Although the device with a Py nanograting showed a slightly more pronounced non-reciprocity there was no evidence found for a strong enhancement of the non-reciprocity in the frequency range of the Py nanograting mode.

5.2 Summary

All-metallic spin wave (SW) propagation devices utilizing $Co_{25}Fe_{75}$ (CoFe) as a SW medium and $Ni_{75}Fe_{25}$ (Py) as nanograting material were studied by travelling SW spectroscopy. The impact of Py nanogratings on top of the CoFe films on the transmission spectra S_{21} and S_{12} were analyzed by comparing the devices with Py nanogratings to those without nanogratings. The sample design consists of a diamond-shaped CoFe waveguide, an aluminum nitride (AlN) insulating interlayer, a Py nanograting and Al antennas with an improved design. The improved single line antenna design showed less attenuation across a wide frequency range in comparison to previous designs.
In the transmission spectra of the devices with an antenna distance of 2 µm, three distinct CoFe SW modes were observed exhibiting a small non-reciprocity. The additional Py nanograting lead to a faintly visible Py nanograting mode above 7.5 GHz that had no impact on the dispersion of the CoFe SW modes. The slight non-reciprocity in the transmission spectra of both devices was visualized with a linecut through the transmission spectra and a map of the non-reciprocity ratio $|\eta_{S_{21}}|$.
The transmission spectra of the devices with an antenna distance of 8.5 µm showed eight CoFe SW modes with a clearly visible non-reciprocity in case of the device with a Py nanograting. Again, a Py nanograting mode could be identified in the respective device. The non-reciprocity was studied by the means of linecuts and maps of the non-reciprocity ratio $|\eta_{S_{21}}|$, which underlined the more pronounced unidirectional propagation observed for the device with a Py nanograting.
The small non-reciprocity with a maximum value of about 5% of the all-metallic devices discussed in this chapter can be explained by the inherently unidirectional propagation of magnetostatic surface spin waves (MSSWs) [34]. However, similar to YIG/CoFe spin wave devices discussed in Ch. 4, a finite chiral pumping (see Sec. 2.6.3) due to a dipolar coupling between the Py nanograting and the CoFe spin wave modes could not be observed.

Chapter 6

Summary and Outlook

In the following chapter, the key findings of this thesis are summarized in Sec. 6.1 and an outlook on possible future research is given in Sec. 6.2.

6.1 Summary

In this thesis, spin wave (SW) propagation devices consisting of magnetic nanogratings on top of planar magnetic thin films are investigated for unidirectional SW transport. In theory, a finite dipolar coupling between the nanowires of the nanograting and the underlying film can strongly enhance the excitation of short-wavelength, unidirectional SW modes (chiral pumping) [13]. To this end, devices with $Y_3Fe_5O_{12}$ (YIG) as the SW medium and nanogratings fabricated with $Co_{25}Fe_{75}$ (CoFe) as well as all-metallic devices with CoFe as the SW medium and $Ni_{75}Fe_{25}$ (Py) nanogratings are studied.

The SW propagation devices require magnetic materials with excellent magnetic properties such as a large effective magnetization and ultra-low SW damping. Therefore, the fabrication of these materials needs to be optimized in regards to their magnetic properties.
High resolution X-ray diffraction (HR-XRD) and in-plane broadband ferromagnetic resonance (bbFMR) measurements are used to compare the structural and magnetic properties of various CoFe multilayer stacks that are fabricated on thermally oxidized Si substrates using magnetron sputtering (cf. Sec. 3.1.1). The results show that a low Gilbert damping parameter of $\alpha = 3.58 \times 10^{-3}$ is achieved with a 3 nm thick Pt seed layer and a 3 nm thick Cu buffer layer, indicating that these layers greatly improve the properties of the CoFe thin films. Therefore, a Pt/Cu/CoFe/Cu/Ta multilayer stack is considered to be a promising material basis for SW propagation devices.
In contrast to the insulating YIG layer in YIG/CoFe SW propagation devices, an electrical insulating buffer layer between the magnetic thin film and the metallic nanograting is needed in the all-metallic CoFe/Py devices to avoid electrical shorts. Therefore, an insulating aluminum nitride (AlN) buffer layer is introduced. The structural and magnetic characterization of a Py thin film and a AlN/Py multilayer hereby shows no significant difference in the structural and magnetic properties of the Py film of the two samples (cf. Sec. 3.1.2). When grown on AlN, Py maintains its low Gilbert damping of $\alpha = 6.78 \times 10^{-3}$ and high effective magnetization of $\mu_0 M_{\text{eff}} = 0.958\,\text{T}$. High res-

olution X-ray diffraction (HR-XRD) and in-plane broadband ferromagnetic resonance (bbFMR) measurements were conducted on a CoFe/AlN and a CoFe/AlN/Py multilayer stack, which revealed that the structural and magnetic properties of CoFe and Py remain unaffected when stacked in this sequence (cf. Sec. 3.1.3). Therefore, it is concluded that an all-metallic SW propagation device comprising CoFe as the SW medium, an AlN insulating buffer layer and a Py nanograting is a viable alternative to CoFe nanogratings on planar YIG films.
For the excitation of unidirectional SWs through the dipolar coupling to a magnetic nanograting, the Kittel mode of the nanowires needs to be excited efficiently. Therefore, nanogratings with excellent structural and magnetic properties need to be fabricated.
The fabrication process of the magnetic nanogratings, which is based on electron-beam (e-beam) lithography, magnetron sputtering and a subsequent lift-off process, is optimized by fabricating nanogratings with different resist recipes for the e-beam lithography step. The CSAR single-layer resist recipe is found to be the most suitable recipe due to its robust handling, minimal residue, and best pattern fidelity after the lift-off process (cf. Sec. 3.2.1).
To characterize the nanogratings, the magnetization dynamics of CoFe nanogratings with various edge-to-edge spacings fabricated on a thermally oxidized Si substrate are investigated by in-plane and out-of-plane bbFMR measurements. The Kittel mode of the nanogratings is found to be located above a frequency of 17 GHz with a coercivity of 40 mT for the CoFe nanogratings when the external magnetic field is directed along the nanowires in the sample plane (cf. Sec. 3.2.2). A shape anisotropy of 0.26 T is observed in the in-plane bbFMR measurement with the magnetic field oriented perpendicular to the nanowires. Out-of-plane bbFMR measurements of CoFe nanogratings with different edge-to-edge spacings reveal a critical wire spacing of 300 nm, below which a stronger coupling between neighboring nanowires impairs the magnetic properties of the nanograting.
In-plane bbFMR measurements with the magnetic field applied parallel to the nanowires conducted for Py nanowires fabricated on a Si substrate reveal that the Kittel mode of the Py nanogratings is located at a frequency of around 7.5 GHz (cf. Sec. 3.2.3). No visible coercivity was observed in this magnetic field configuration. When the magnetic field is applied perpendicular to the nanowires, a small anisotropy of 0.07 T is detected. Furthermore, Py nanogratings are fabricated on a CoFe/AlN stack. The data from the in-plane bbFMR measurement with the magnetic field aligned along the nanowires indicate that the Kittel mode of the Py nanogratings can be efficiently excited when fabricated on top of a CoFe/AlN thin film stack.
The optimized CoFe and Py thin films as well as the respective nanogratings enable the fabrication of SW propagation devices with a strong Kittel resonance of the nanograting and low SW damping in the SW medium.

To investigate unidirectional SW propagation, first, devices with YIG as the SW medium and nanogratings consisting of CoFe are studied. Prior to the structuring of CoFe nanogratings on top of the YIG films, out-of-plane bbFMR measurements are performed to study the magnetic properties of a 5 µm thick YIG film grown via liquid phase epitaxy

(LPE-YIG) and a 25 nm thick YIG film grown using pulsed-laser deposition (PLD-YIG). The extracted material parameters from the bbFMR data for both thin films are found to be comparable to previous findings reported at WMI [45, 53].
A SW propagation device structured on the 5 µm thick LPE-YIG sample with a CoFe nanograting with an edge-to-edge distance between the nanowires of 600 nm is investigated by performing SW propagation measurements. To this end, two aluminium (Al) antennas with a distance of 8.5 µm are fabricated on top of the CoFe nanogratings. Two low frequency SW modes of the YIG film are detected in the transmission spectra, but no high frequency mode enhanced by the nanograting is observed (cf. Sec. 4.2).
Furthermore, for a device fabricated on a 25 nm thick PLD-YIG sample with an edge-to-edge distance of 400 nm between the CoFe nanowires a new stripline antenna design is utilized. This antenna design results in less microwave attenuation than the design used for the LPE-YIG SW device. The transmission spectra for this device showed only a single low frequency YIG mode, and no mode associated with the CoFe nanograting (cf. Sec. 4.3). A non-reciprocity was detected in the YIG mode at frequencies below 5 GHz, which might be linked to either unidirectional propagation of magnetostatic surface SWs (MSSWs) or to non-reciprocity stemming from an interfacial Dzyaloshinskii-Moriya interaction at the interface of the YIG film and the $Gd_3Ga_5O_{12}$ (GGG) substrate, which was found previously [11].

Second, all-metallic SW propagation devices utilizing CoFe as the SW medium and antenna distances of 2 µm and 8.5 µm are studied by traveling SW spectroscopy. The effect of Py nanogratings on the transmission spectra of CoFe films is investigated by comparing devices with and without Py nanogratings. The sample design includes a diamond-shaped CoFe waveguide, an AlN insulating interlayer, a Py nanograting, and optimized Al antennas. The new antenna design exhibits less microwave attenuation across a wide frequency range in comparison to previous designs.
Spin wave propagation measurements on devices with an antenna distance of 2 µm reveal three distinct CoFe SW modes in the transmission spectra, with a small non-reciprocity observed for both the device with and without a Py nanograting (cf. Sec. 5.1.1). A weakly visible Py nanograting mode above 7.5 GHz is visible in the data of the respective device, but does not affect the dispersion of the CoFe SW modes. The non-reciprocity in the transmission spectra of both devices is characterized by a non-reciprocity ratio, which reaches a maximum of 3% in case of the device with a Py nanograting.
The devices with an antenna distance of 8.5 µm exhibit eight CoFe SW modes in their transmission spectra (cf. Sec. 5.1.2), where the device with a Py nanograting shows a noticeable non-reciprocity. As before, the Py nanograting mode is also present for the respective device, but no coupling to the CoFe SW modes is observed. The non-reciprocity ratio exhibits a maximum value of 5% for the device with a Py nanograting. The non-reciprocity observed for the all-metallic devices might be due to the inherently unidirectional propagation of MSSWs [34].
Unfortunately, no clear unidirectional SW propagation due to dipolar coupling between the nanograting and the SW medium could be observed, which needs further research.

6.2 Outlook

The results of this work provide multiple starting points for further investigations.
First, the observed non-reciprocity of the fundamental SW mode for the device utilizing a PLD-YIG thin film sample as the SW medium and CoFe nanogratings needs to be clarified. Since the non-reciprocity of MSSWs is more pronounced in thicker films, devices with varying YIG film thicknesses and reference devices without a CoFe nanograting could provide further evidence if the non-reciprocity is due to the excitation of MSSWs. Additionally, utilizing YIG waveguides instead of planar thin films could allow for the observation of CoFe nanograting modes in the SW propagation measurements, as the magnetic volume of the SW medium and the nanograting would be similar. The YIG waveguide could also result in an enhanced SW amplitude and therefore better signal-to-noise ratio (SNR), as a preferred SW propagation direction is defined. The presence of CoFe nanograting modes together with the better SNR of the YIG waveguide modes could then reveal a possible chiral pumping effect.
As a next step, nanogratings made from materials other than CoFe could be first fabricated on a Silicon substrate and characterized by bbFMR measurements. Subsequent patterning of a SW propagation device with the new nanograting material could reveal, if the frequency of the chiral pumping effect can be adjusted by the selection of a nanograting material with a suitable FMR frequency. This would enable the frequency engineering of the effect to adapt the non-reciprocal device to the optimal operating frequency needed in a specific application. New nanograting materials together with an adjustment of the dimensions of the nanograting could also result in an increase of its magnetic anisotropy. This would allow for an antiparallel configuration of the magnetization in the YIG film and the nanograting across a larger magnetic field interval. For this configuration, a particularly strong non-reciprocity was observed in Ref. [13].

The non-reciprocity observed for the all-metallic system utilizing CoFe as SW medium and a Py nanograting could be further investigated by adjusting the thickness of the AlN insulating layer. Decreasing the thickness of the AlN interlayer enhances the dipolar coupling between the Py nanowires and the CoFe waveguide. This could be verified by a reference device without a Py nanograting. The minimal thickness of the AlN layer is however limited, since a robust insulation of the CoFe waveguide needs to be ensured. As already discussed above, the exploration of new nanograting materials with different FMR frequencies and larger magnetic anisotropies than the Py nanogratings could enable the tuning of the chiral pumping effect in all-metallic systems.

Regardless of the material system used, measurements at cryogenic temperatures would give insight on the performance of the respective non-reciprocal device at low temperatures for applications such as quantum computers with superconducting qubits. Thereby, superconducting antennas could be utilized, to improve the impedance at low temperatures.

Finally, functionalities of magnetic nanogratings other than enhancing unidirectional

SW modes could be explored. A magnonic-based memory device was recently demonstrated by using a similar sample design as used in Sec. 4.2 [60]. For the magnonic memory device, two small arrays of Py nanowires were structured on a YIG thin film exclusively underneath the two microwave antennas of the device. In this device, the parallel and antiparallel alignment of the magnetization of a Py nanowire with respect to the magnetization in the YIG film was used as a magnetic bit. The state of the magnetic bit could then be controlled by SWs that were excited at the opposing antenna, enabling reading as well as writing. This again shows that SW propagation devices are promising for future unidirectional microwave devices.

Appendix A

Appendix

A.1 Methods

The following section provides details on the fabrication methods, processing recipes and experimental analysis methods. The three main fabrication steps - electron-beam lithography, magnetron sputter deposition and lift-off process - are discussed in Secs. A.1.2, A.1.4 and A.1.4. The three different resist recipes that were compared in Sec. 3.2.1 are listed in Sec. A.1.5. The utilized experimental methods - high-resolution X-ray diffraction and atomic force microscopy - are described in Secs. A.1.6 and A.1.7.

A.1.1 Fabrication process of nanowires

In Fig. A.1.1 the fabrication process of the nanowires is illustrated step by step. In (a) the spin coated sample is exposed to the electron beam to write the desired pattern into the resist. The exposed resist is stripped with a developing chemical in (b) to yield the partially uncovered substrate in (c). Hereby, the developer is washed off with isopropyl to interrupt the developing process. Afterwards the desired material is sputtered onto the sample as shown in (d). The lift-off process is performed in (e), where the sample with the deposited material is immersed into a remover chemical. The remover strips the resist with the deposited material on top from the substrate to reveal the desired pattern in (f).

A.1.2 Electron-beam lithography

Electron-beam (e-beam) lithography utilizes a focused beam of electrons to expose an electron-sensitive resist film. This allows for the patterning of custom structures down to sub 10 nm dimensions without the need of lithography masks [48].
Before applying the resist layer, the surface of the sample is cleaned in beaker glasses with acetone and isopropyl in an ultrasonic bath. Persisting solvent leftovers are removed by heating up the sample on a hotplate at 200 °C. Subsequently, the electron sensitive resist and a conductive resist layer are spin coated on the sample. The conductive resist layer prevents the formation of electrostatic charges that would impair the writing process. When exposed to a sufficient dose of electrons, the e-beam resist changes its solubility in its associated developing chemical. Due to the small surface area of the

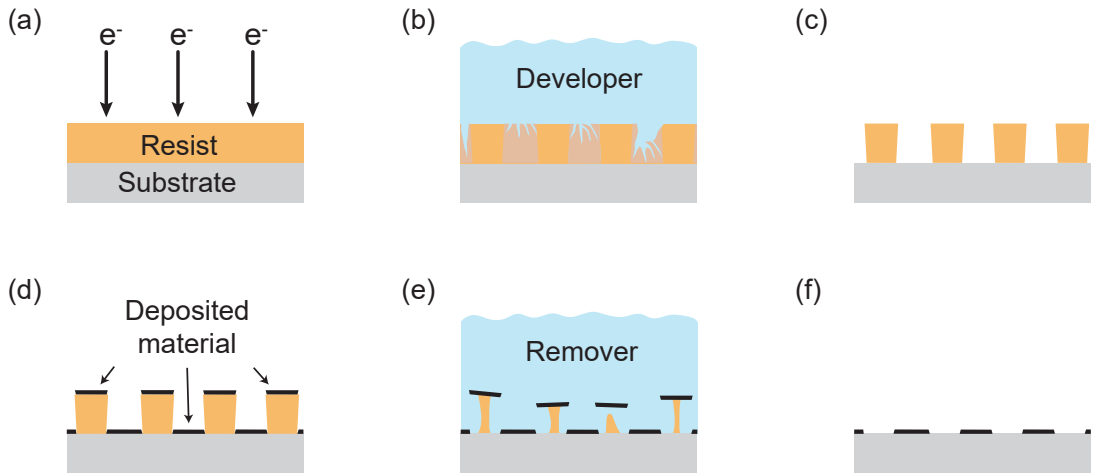

Figure A.1.1: (a) Resist is spin coated on the sample and exposed by the electron beam of the lithography setup. (b) The sample is immersed into the developing chemical that removes the resist in the exposed areas as shown in (c). (d) The desired material is sputtered onto the sample and adheres to the substrate in the exposed areas. (e) The sample is immersed into a chemical that removes the unexposed resist together with the deposited material on top. (f) Finally, the pattern is cleaned.

structures being written here, only positive resists are used, which are removed by the developer in the exposed areas. To focus the electron beam on the sample surface, either gold nanoparticles or platinum markers placed in the corners of the sample are utilized. During exposure, the electron beam scans across the surface to draw the predefined pattern in the resist. Thereby, the electron dose per unit area ought to be constant across the exposed area. This is an involved task as not only the electrons coming directly from the beam need to be taken into account but also forward and backward scattered electrons. The amount of forward and backward scattered electrons, adding to the base dose coming from the beam, depend on the shape and density of patterns in the respective area. To keep the net dose per area constant across the entire pattern, the dose coming from the beam needs to be varied depending on the local pattern geometry. For this, the scattering events present for the respective pattern are simulated with the software Beamer. This software is developed by GenISys and utilizes Monte Carlo methods. This dose correction process is especially important for nanometer scale structures with a high pattern density, such as the nanogratings fabricated in this work. After writing, the sample is immersed into a developer chemical that removes the resist in the exposed areas, enabling the adhesion of material onto the surface of the sample

A.1.3 Magnetron sputtering

All thin film materials in this work excluding the $Y_3Fe_5O_{12}$ thin film samples are deposited by magnetron sputtering using the SUPERBOWL ultra-high vacuum sputter deposition cluster. Hereby, an inert gas (e.g Argon) is injected into the sputtering chamber to create a plasma. The positively charged ions are accelerated towards a tar-

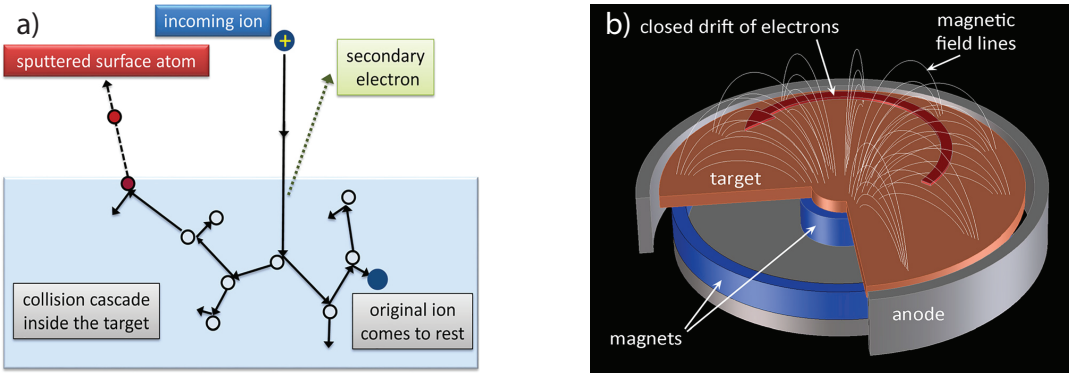

Figure A.1.2: (a) Schematic representation of the collision cascade inside the target upon collision of an accelerated ion. Target material as well as secondary electrons leave the target. (b) Magnetron with the target, anode ring and permanent magnets, which generate a magnetic field illustrated by the white lines. Electrons are trapped above the target on circularly trajectories as indicated by the red arrow. Figures taken from Ref. [61].

get consisting of the desired sputtering material by applying a voltage of a few hundred volts between the target and an anode ring. When reaching the target, the ions trigger a collision cascade (cf. Fig. A.1.2 (a)) that leads to the ejection of target material towards the sample, where it is adsorbed. During the collision cascade, also secondary electrons leave the target. The electrons are trapped by a magnetic field on a circular trajectory to prevent them from immediately reaching the anode ring as shown in Fig. A.1.2 (b). This increases the collision probability between the electrons and the gas atoms to create a plasma of ions and further electrons. Therefore, only a relatively low density of sputter gas atoms is necessary to generate enough ions during deposition, which yields a long enough mean free path for the target material to reach the sample. The deposition pressures is usually in the range of a few 10^{-3} mbar.

A.1.4 Lift-off process

For the samples fabricated in this work, the lift-off process for structuring the nanogratings proved to be especially challenging. Therefore, the samples were immersed into the remover for at least 24 hours on a hotplate at 40 °C, so that the remover had time to clear the valleys in between the nanowires from all the resist. Also, rather intense cleaning in the ultrasonic bath was employed to remove any remaining residue. Together with a slight increase in the base dose during the e-beam lithography, this yielded a significantly improved end result.

A.1.5 Processing recipes

In the following, the three resist processing recipes for the fabrication of magnetic nanogratings discussed in Sec. 3.2.1 are (Single-layer CSAR recipe, double-layer PMMA recipe, double-layer CSAR/PMMA recipe) listed.

CSAR single layer recipe

Cleaning	- Acetone 120 s, level 9 - IPA 120s, level 9 - Hotplate 200 °C (1 min)
Spin coating	- 20 µL resist AR-P 6200.09 - Spin coating: 4000 RPM (1 min) - Bake at 150 °C (1 min) - Gold nanoparticles - 30 µL resist AR-PC 5090.02 (Electra 92) - Spin coating: 4000 RPM (1 min) - Bake at 90 °C (2 min)
E-beam writing	- Proximity error correction with Beamer - Base dose 2.4 C/m^2 - Beam current 2.1 nA
Developing	- Remove electra with water - AR-600-546 constant movement (60 s) - IPA (dip) - IPA cleaning
Sputter deposition	
Lift-off	- AR 600-71 40 °C hotplate (24 h) - Rinse with pipet inside beaker - Ultrasonic bath up to level 4 (10 s) - IPA cleaning

PMMA double layer recipe

Cleaning	- Acetone 120 s, level 9 - IPA 120s, level 9 - Hotplate 200 °C (1 min)
Spin coating	- 20 µL resist AR-P 669.04 - Spin coating: 4000 RPM (1 min) - Bake at 170 °C (5 min) - 20 µL resist AR-P 679.02 - Spin coating: 4000 RPM (1 min) - Bake at 90 °C (2 min) - Gold nanoparticles - 30 µL resist AR-PC 5090.02 (Electra 92) - Spin coating: 4000 RPM (1 min) - Bake at 90 °C (2 min)
E-beam writing	- Proximity error correction with Beamer - Base dose 4.5 C/m^2 - Beam current 2.1 nA
Developing	- Remove electra with water - AR600-56 constant movement (120 s) - IPA (dip) - IPA cleaning
Sputter deposition	
Lift-off	- Acetone 70 °C hotplate (20 min) - Rinse with pipet inside beaker - Ultrasonic bath if necessary - IPA cleaning

CSAR/PMMA double layer recipe

Cleaning	- Acetone 120 s, level 9 - IPA 120s, level 9 - Hotplate 200 °C (1 min)
Spin coating	- 20 µL resist AR 6200.13 - Spin coating: 1500 RPM (2 min) - Bake at 150 °C (1 min) - 20 µL resist AR-P 672.045 - Spin coating: 1600 RPM (105 s) - Bake at 150 °C (3 min) - Gold nanoparticles - 30 µL resist AR-PC 5090.02 (Electra 92) - Spin coating: 4000 RPM (1 min) - Bake at 90 °C (2 min)
E-beam writing	- Proximity error correction with Beamer - Base dose 4 C/m^2 - Beam current 2.1 nA
Developing	- Remove electra with water - AR600-56 constant movement (180 s) - Stop in IPA (30 s) - AR600-546 constant movement (120 s) - Stop in IPA (30 s) - IPA cleaning
Sputter deposition	
Lift-off	- AR 600-71 40 °C hotplate (4 h) - Rinse with pipet inside beaker - Ultrasonic bath if necessary - IPA cleaning

A.1.6 High-resolution X-ray diffraction

The structural properties of the thin films in this work are investigated by high-resolution X-ray diffraction (HR-XRD) measurements. The HR-XRD setup is schematically depicted in Fig. A.1.3 (a). A monochromatic Cu-$K_{\alpha 1}$ X-ray beam with a wavelength of $\lambda = 1.5406$ Å is scattered at the sample under the incident angle ω. The X-ray detector is positioned at the total deflection angle 2θ in respect to the incident beam. The X-ray beam is diffracted at the lattice planes of a crystalline sample as shown in Fig. A.1.3 (b). Depending on the optical path difference between the X-rays scattered at different lattice planes, the outgoing X-rays interfere constructively or destructively. Bragg's law describes the condition for constructive interference depending on the angle θ with [63]

$$2d_{hkl}\sin(\theta) = \lambda, \tag{A.1}$$

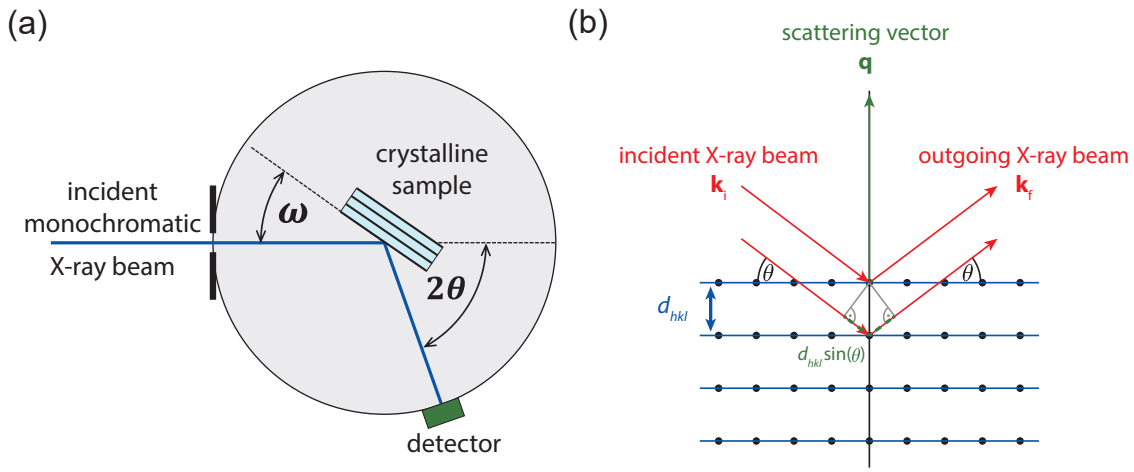

Figure A.1.3: (a) Schematic depiction of the high-resolution X-ray diffraction setup with the incident angle ω and the total deflection angle θ. Figure taken from Ref. [15]. (b) Elastic scattering of the incident X-ray beam at adjacent lattice planes. When the optical path difference $2d_{hkl}\sin(\theta)$ between X-rays scattered at different depths is a multiple of the wavelength λ, the waves interfere constructively. The scattering process can be described with the scattering vector $\mathbf{q} = \mathbf{k}_\mathrm{i} - \mathbf{k}_\mathrm{f}$, where $\mathbf{k}_\mathrm{i}$ and $\mathbf{k}_\mathrm{f}$ are the wavevectors of the incident and outgoing beam, respectively. Figure taken from Ref. [62].

where d_{hkl} is the distance between adjacent lattice planes with the same Miller indices (hkl). In 2θ-ω-scans an intensity spectrum is recorded as a function of the angle θ, where characteristic reflections can be observed when the Bragg condition is fulfilled. Thereby, the direction of the scattering vector $\mathbf{q} \parallel (hkl)$ remains unchanged. This is achieved by keeping a fixed relation of $2\theta = 2(\omega - \omega_\mathrm{offset})$, where the offset angle ω_offset accounts for a possible miscut of the crystal surface. 2θ-ω-scans provide information about the crystalline symmetry, the lattice constants and possible crystalline impurity phases. To increase the incident flux of the X-ray beam, additional measurements are carried out without the X-ray monochromator in the framework of this thesis.

A.1.7 Atomic force microscopy

The surface topography of the nanograting samples is probed with an atomic force microscope (AFM). The basic working principle of an AFM is depicted in Fig. A.1.4. A microscopic tip attached to a cantilever is used to scan across the surface of the sample. The distance of the tip to the surface can be manipulated by a piezoelectric element on which the cantilever is mounted. A laser is focused on the back of the tip from where it is reflected onto a photo detector. The movement of the tip leads to a displacement of the reflected laser light and can therefore be measured with the photodetector. The AFM can be used in different topographic modes that are distinguished by the regime

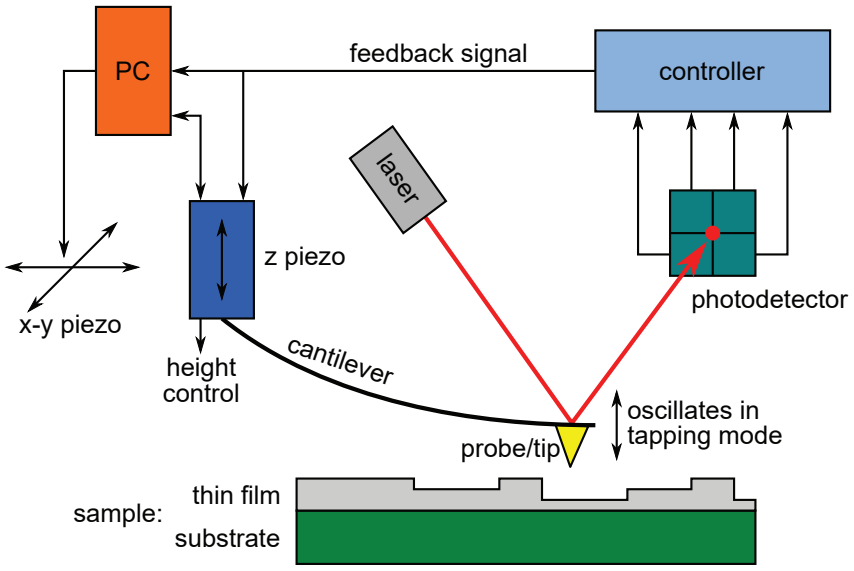

Figure A.1.4: Schematic depiction of an atomic force microscope (AFM). The sample is placed on a stage movable in x-y-direction and scanned with a tip mounted on a cantilever. A laser is focused on the back of the tip and reflected onto a photodetector. The photodetector measures the deflection of the laser light and a feedback signal is sent to a piezo element, controlling the height of the tip. Figure taken from Ref. [64].

of the force distance curve the tip is operated in. In the non-contact mode and tapping mode, the tip is oscillating above the sample, whereby changes in the oscillating motion reveal height differences on the sample.
The AFM scans presented in this work are recorded in the contact mode. Here, the tip dragged along the surface of the sample from where it is repelled depending on the surface topography below the tip. This operating mode allowed for a precise scanning of the valleys in between the nanowires even for the smallest wire spacings.

A.2 Broadband ferromagnetic resonance measurements

Figure A.2.1 shows the real part of the background corrected S_{21}-parameter recorded at in-plane bbFMR measurements of Py nanogratings on a CoFe/AlN multilayer stack. The spacings a between the nanowires range from 400 nm to 1200 nm. The magnetic field is applied perpendicular to the nanowires in the sample plane.

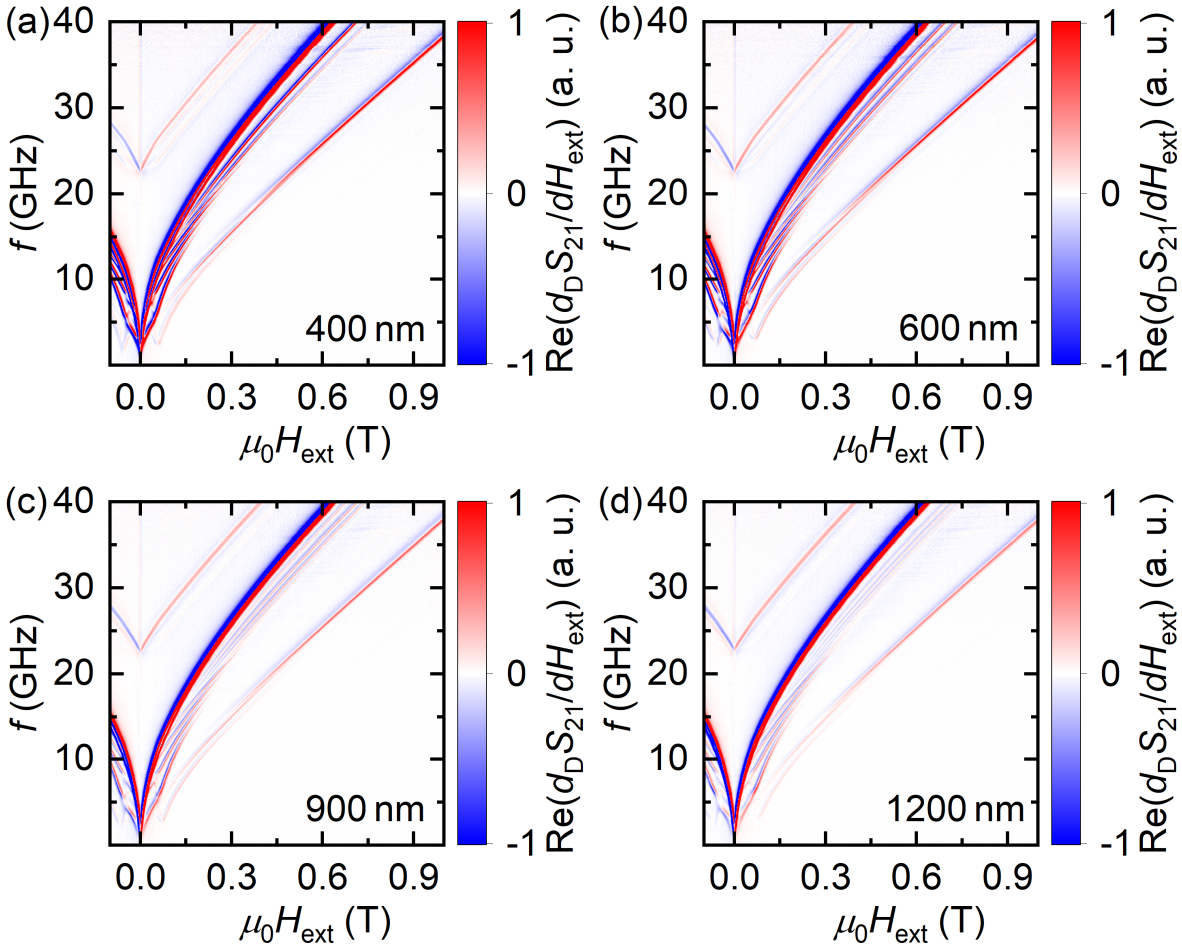

Figure A.2.1: Room temperature, in-plane bbFMR data of Py nanogratings fabricated on a CoFe/AlN multilayer stack with wire spacings a ranging from (a) 400 nm to (d) 1200 nm. The external magnetic field is applied perpendicular to the nanowires and swept from positive to negative values. A mode stemming from the CoFe thin film starting at $\mu_0 H_{ext} = 0$ T and a mode exhibiting a finite anisotropy stemming from the Py nanograting can be identified in all plots.

A.3 Spin wave propagation measurements

This section provides additional spin wave spectroscopy data.

A.3.1 Reflection spectra of spin wave propagation device structured on PLD-YIG

Figure A.3.1 shows the real part of the background corrected reflection spectra S_{11} (a) and S_{22} (b) of the CoFe nanograting device structured on the 25 nm PLD-YIG film.

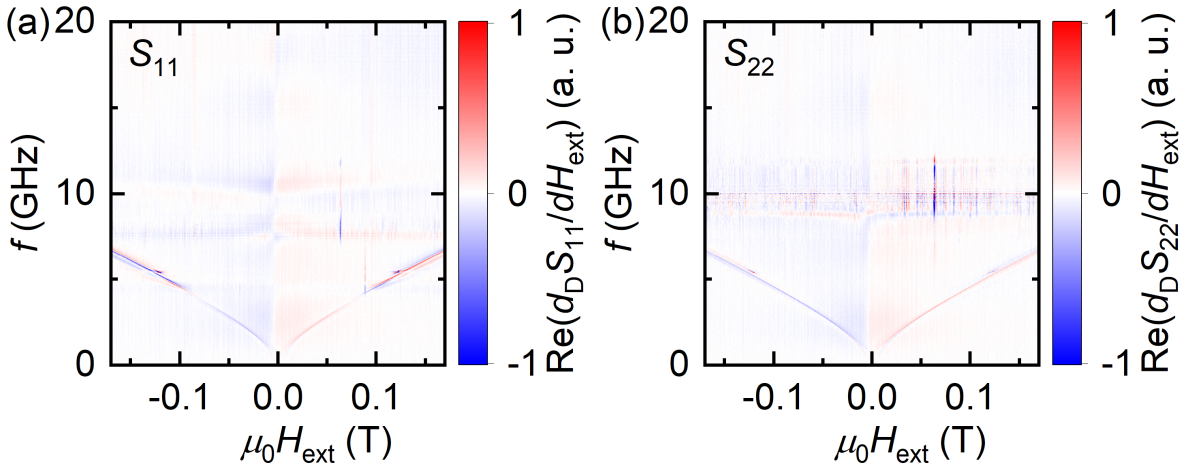

Figure A.3.1: Background corrected reflection spectra S_{11} (a) and S_{22} (b) of a nanograting device structured on a 25 nm PLD-YIG thin film with a spacing between the wires of $a = 400$ nm and an edge-to-edge antenna distance of $d = 8.5$ µm. The plots show one dipolar spin wave mode of the YIG film and no mode associated with the CoFe nanograting.

A.3.2 Reflection spectra of all-metallic spin wave propagation devices with 2 µm antenna distance

Figure A.3.2 shows the reflection spectra of a device without a nanograting in (a)-(b) and with a Py nanograting in (c)-(d). Hereby, the edge-to-edge distance between the respective antennas is $d = 2$ µm and the edge-to-edge distance between the wires of the device with a Py nanograting is $a = 500$ nm.

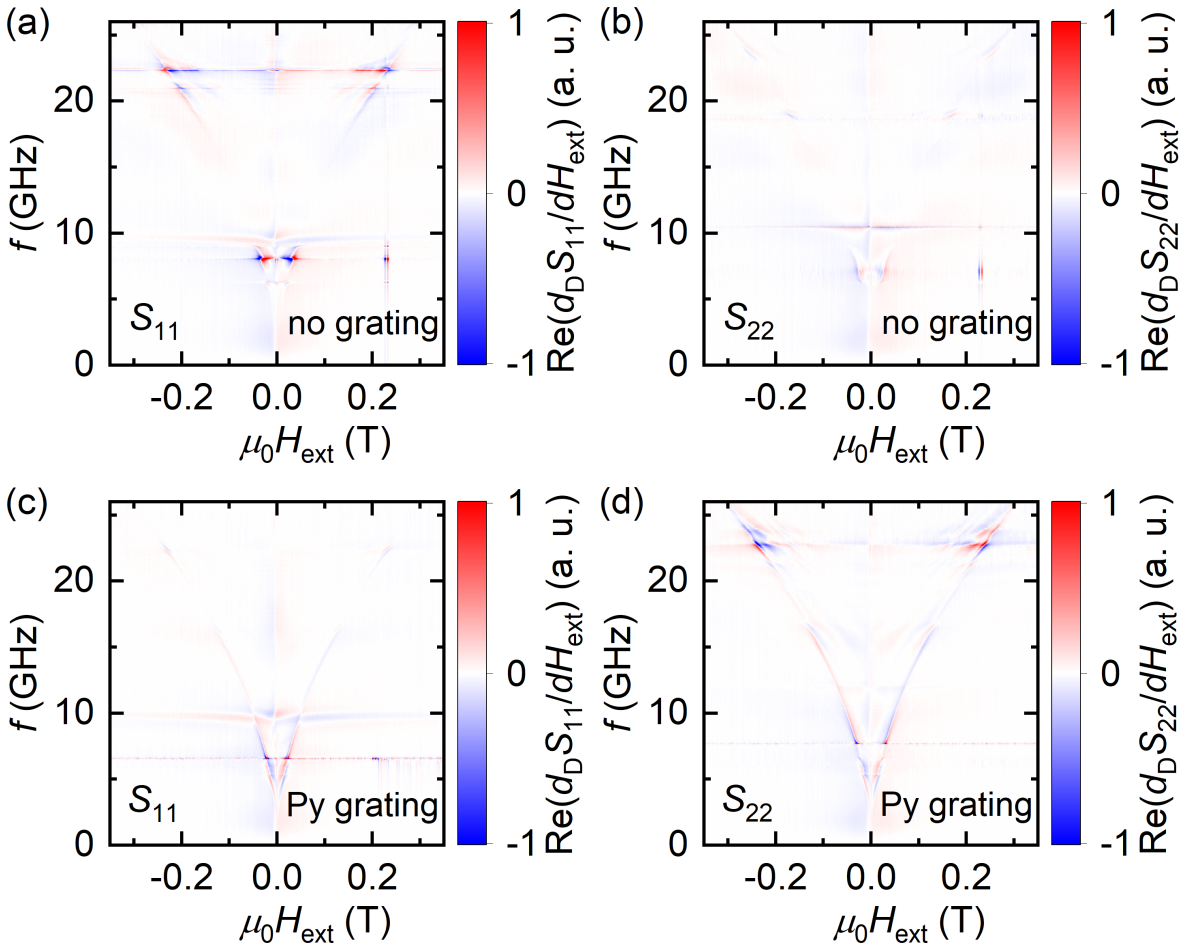

Figure A.3.2: Reflection spectra (background corrected S_{11} and S_{22}) of the all-metallic SW propagation devices with an edge-to-edge distance of $d = 2\,\mu m$ between the Al antennas. (a)-(b) Spectra of the device without a nanograting and (c)-(d) spectra of the device with a Py nanograting with edge-to-edge spacings of $a = 500\,nm$ between the Py nanowires.

A.3.3 Reflection spectra of all-metallic spin wave propagation devices with 8.5 µm antenna distance

In Fig. A.3.3 the reflection spectra of the all-metallic devices with an edge-to-edge distance between the antennas of $d = 8.5\,\mu m$ are shown.

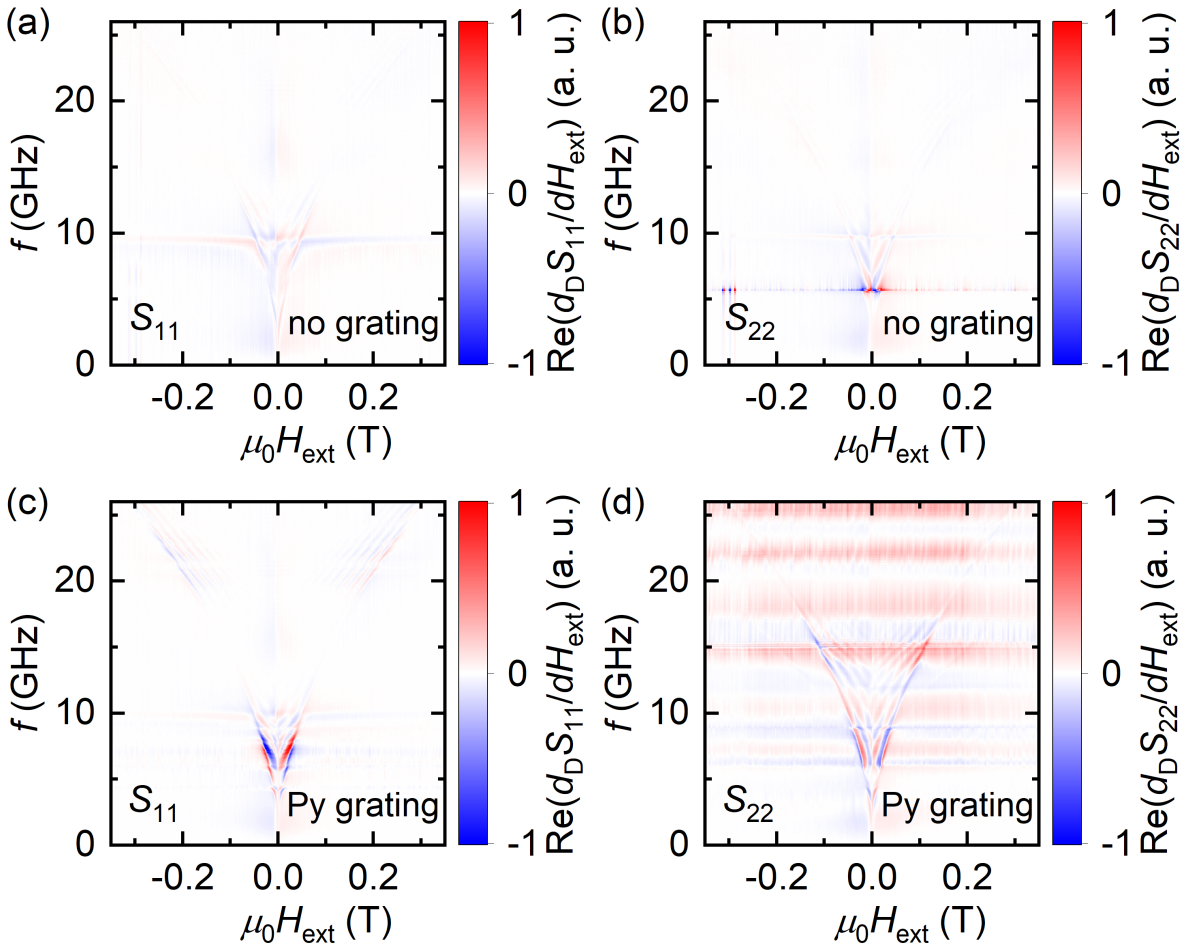

Figure A.3.3: Background-corrected transmission spectra from SW propagation measurements of devices with a edge-to-edge distance d of 8.5 µm between the antennas. (a)-(b) The reflection spectra of the device without a nanograting and (c)-(d) reflection spectra of the device with a Py nanograting with edge-to-edge spacings of $a = 500$ nm between the Py nanowires.

A.3.4 Spin wave propagation measurements of an all-metallic device with 1 µm antenna distance

Figure A.3.4 depicts (a)-(b) the transmission spectra S_{12} and S_{21} and (c)-(d) reflection spectra S_{22} and S_{11} of an all-metallic device with an edge-to-edge antenna distance of $d = 1$ µm. The SW proagation device is fabricated without a nanograting on top of the CoFe waveguide.

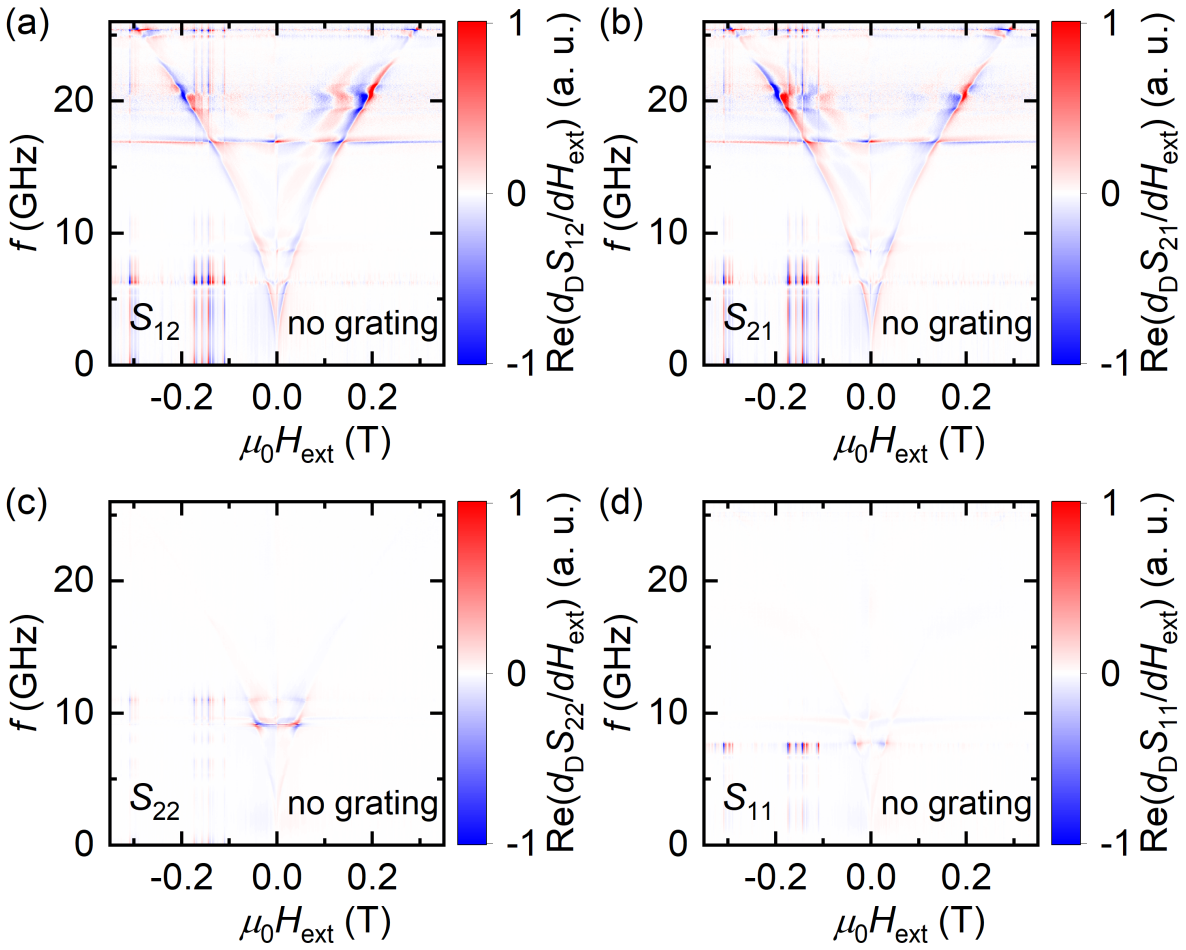

Figure A.3.4: Background-corrected (a)-(b) transmission S_{12} and S_{21} and (c)-(d) reflection spectra S_{22} and S_{11} of an all-metallic device without a nanograting and an edge-to-edge antenna distance of $d = 1\,\mu\text{m}$.

Bibliography

[1] E. Verhagen and A. Alù, *Optomechanical Nonreciprocity*, Nature Physics **13**, 922 (2017).

[2] W. Palmer, D. Kirkwood, S. Gross, M. Steer, H. S. Newman, and S. Johnson, *A Bright Future for Integrated Magnetics: Magnetic Components Used in Microwave and Mm-Wave Systems, Useful Materials, and Unique Functionalities*, IEEE Microwave Magazine **20**, 36 (2019).

[3] A. M. Song, M. Missous, P. Omling, A. R. Peaker, L. Samuelson, and W. Seifert, *Unidirectional Electron Flow in a Nanometer-Scale Semiconductor Channel: A Self-Switching Device*, Applied Physics Letters **83**, 1881 (2003).

[4] M. Hafezi and P. Rabl, *Optomechanically Induced Non-Reciprocity in Microring Resonators*, Optics Express **20**, 7672 (2012).

[5] C. L. Hogan, *The Ferromagnetic Faraday Effect at Microwave Frequencies and Its Applications*, Reviews of Modern Physics **25**, 253 (1953).

[6] V. G. Harris, *Modern Microwave Ferrites*, IEEE Transactions on Magnetics **48**, 1075 (2012).

[7] A. V. Chumak, V. I. Vasyuchka, A. A. Serga, and B. Hillebrands, *Magnon Spintronics*, Nature Physics **11**, 453 (2015).

[8] P. R. Emtage, *Generation of Magnetostatic Surface Waves by a Microstrip*, Journal of Applied Physics **53**, 5122 (1982).

[9] A. Ganguly and D. Webb, *Microstrip Excitation of Magnetostatic Surface Waves: Theory and Experiment*, IEEE Transactions on Microwave Theory and Techniques **23**, 998 (1975).

[10] K. Di, V. L. Zhang, H. S. Lim, S. C. Ng, M. H. Kuok, J. Yu, J. Yoon, X. Qiu, and H. Yang, *Direct Observation of the Dzyaloshinskii-Moriya Interaction in a Pt/Co/Ni Film*, Physical Review Letters **114**, 047201 (2015).

[11] H. Wang, J. Chen, T. Liu, J. Zhang, K. Baumgaertl, C. Guo, Y. Li, C. Liu, P. Che, S. Tu, S. Liu, P. Gao, X. Han, D. Yu, M. Wu, D. Grundler, and H. Yu, *Chiral Spin-Wave Velocities Induced by All-Garnet Interfacial Dzyaloshinskii-Moriya Interaction in Ultrathin Yttrium Iron Garnet Films*, Physical Review Letters **124**, 027203 (2020).

[12] T. Yu, Y. M. Blanter, and G. E. W. Bauer, *Chiral Pumping of Spin Waves*, Physical Review Letters **123**, 247202 (2019).

[13] J. Chen, T. Yu, C. Liu, T. Liu, M. Madami, K. Shen, J. Zhang, S. Tu, M. S. Alam, K. Xia, M. Wu, G. Gubbiotti, Y. M. Blanter, G. E. W. Bauer, and H. Yu, *Excitation of Unidirectional Exchange Spin Waves by a Nanoscale Magnetic Grating*, Physical Review B **100**, 104427 (2019).

[14] M. Jamali, J. H. Kwon, S.-M. Seo, K.-J. Lee, and H. Yang, *Spin Wave Nonreciprocity for Logic Device Applications*, Scientific Reports **3**, 3160 (2013).

[15] R. Gross and A. Marx, *Festkörperphysik* (De Gruyter Oldenbourg, 2014).

[16] J. M. D. Coey, *Magnetism and Magnetic Materials* (Cambridge University Press, Cambridge, 2010).

[17] L. Liensberger, *Magnon Hybrid Dynamics*, Ph.D. thesis, Technische Universität München, München (2021).

[18] L. Landau and E. Lifshitz, in *Perspectives in Theoretical Physics*, edited by L. P. Pitaevski (Pergamon, Amsterdam, 1992) pp. 51–65.

[19] J. M. Lock, *Eddy Current Damping in Thin Metallic Ferromagnetic Films*, British Journal of Applied Physics **17**, 1645 (1966).

[20] T. Gilbert, *A Phenomenological Theory of Damping in Ferromagnetic Materials*, IEEE Transactions on Magnetics **40**, 3443 (2004).

[21] D. Polder, *VIII. On the Theory of Ferromagnetic Resonance*, The London, Edinburgh, and Dublin Philosophical Magazine and Journal of Science **40**, 99 (1949).

[22] C. Kittel, *On the Theory of Ferromagnetic Resonance Absorption*, Physical Review **73**, 155 (1948).

[23] L. Flacke, L. Liensberger, M. Althammer, H. Huebl, S. Geprägs, K. Schultheiss, A. Buzdakov, T. Hula, H. Schultheiss, E. R. J. Edwards, H. T. Nembach, J. M. Shaw, R. Gross, and M. Weiler, *High Spin-Wave Propagation Length Consistent with Low Damping in a Metallic Ferromagnet*, Applied Physics Letters **115**, 122402 (2019).

[24] J.-M. Beaujour, D. Ravelosona, I. Tudosa, E. E. Fullerton, and A. D. Kent, *Ferromagnetic Resonance Linewidth in Ultrathin Films with Perpendicular Magnetic Anisotropy*, Physical Review B **80**, 180415 (2009).

[25] L. Liensberger, *Spin-Orbit Torques and Magnetization Dynamics in Non-collinear Magnets*, Master's thesis, Technische Universität München, München (2017).

[26] P. D. L. Louis, *Broadband-Spectroscopy of Magnetic Materials at Low Temperatures*, Master's thesis, Technische Universität München, München (2016).

[27] O. Karlqvist, *Calculation of the Magnetic Field in Ferromagnetic Layer of a Magnetic Drum*, (1954).

[28] H. T. Nembach, T. J. Silva, J. M. Shaw, M. L. Schneider, M. J. Carey, S. Maat, and J. R. Childress, *Perpendicular Ferromagnetic Resonance Measurements of Damping and Lande G- Factor in Sputtered (Co2Mn)1-xGex Thin Films*, Physical Review B **84**, 054424 (2011).

[29] H. Maier-Flaig, S. T. B. Goennenwein, R. Ohshima, M. Shiraishi, R. Gross, H. Huebl, and M. Weiler, *Note: Derivative Divide, a Method for the Analysis of Broadband Ferromagnetic Resonance in the Frequency Domain*, Review of Scientific Instruments **89**, 076101 (2018).

[30] V. V. Kruglyak, S. O. Demokritov, and D. Grundler, *Magnonics*, Journal of Physics D: Applied Physics **43**, 264001 (2010).

[31] A. Prabhakar and D. Stancil, *Spin Waves: Theory and Applications* (Springer US, Boston, MA, 2009).

[32] B. A. Kalinikos and A. N. Slavin, *Theory of Dipole-Exchange Spin Wave Spectrum for Ferromagnetic Films with Mixed Exchange Boundary Conditions*, Journal of Physics C: Solid State Physics **19**, 7013 (1986).

[33] O. Gladii, M. Haidar, Y. Henry, M. Kostylev, and M. Bailleul, *Frequency Nonreciprocity of Surface Spin Wave in Permalloy Thin Films*, Physical Review B **93**, 054430 (2016).

[34] R. E. Camley, *Nonreciprocal Surface Waves*, Surface Science Reports **7**, 103 (1987).

[35] K. L. Wong, L. Bi, M. Bao, Q. Wen, J. P. Chatelon, Y.-T. Lin, C. A. Ross, H. Zhang, and K. L. Wang, *Unidirectional Propagation of Magnetostatic Surface Spin Waves at a Magnetic Film Surface*, Applied Physics Letters **105**, 232403 (2014).

[36] T. Yu, S. Sharma, Y. M. Blanter, and G. E. W. Bauer, *Surface Dynamics of Rough Magnetic Films*, Physical Review B **99**, 174402 (2019).

[37] T. Moriya, *Anisotropic Superexchange Interaction and Weak Ferromagnetism*, Physical Review **120**, 91 (1960).

[38] A. Fert, V. Cros, and J. Sampaio, *Skyrmions on the Track*, Nature Nanotechnology **8**, 152 (2013).

[39] J.-H. Moon, S.-M. Seo, K.-J. Lee, K.-W. Kim, J. Ryu, H.-W. Lee, R. D. McMichael, and M. D. Stiles, *Spin-Wave Propagation in the Presence of Interfacial Dzyaloshinskii-Moriya Interaction*, Physical Review B **88**, 184404 (2013).

[40] S. Tacchi, R. E. Troncoso, M. Ahlberg, G. Gubbiotti, M. Madami, J. Åkerman, and P. Landeros, *Interfacial Dzyaloshinskii-Moriya Interaction in Pt / CoFeB Films: Effect of the Heavy-Metal Thickness*, Physical Review Letters **118**, 147201 (2017).

[41] J. Chen, H. Yu, and G. Gubbiotti, *Unidirectional Spin-Wave Propagation and Devices*, Journal of Physics D: Applied Physics **55**, 123001 (2022).

[42] T. Yu, C. Liu, H. Yu, Y. M. Blanter, and G. E. W. Bauer, *Chiral Excitation of Spin Waves in Ferromagnetic Films by Magnetic Nanowire Gratings*, Physical Review B **99**, 134424 (2019).

[43] J. Ding, M. Kostylev, and A. O. Adeyeye, *Magnetic Hysteresis of Dynamic Response of One-Dimensional Magnonic Crystals Consisting of Homogenous and Alternating Width Nanowires Observed with Broadband Ferromagnetic Resonance*, Physical Review B **84**, 054425 (2011).

[44] K. Zhu, C. Jin, Z. Klencsár, A. S. Ganeshraja, and J. Wang, *Cobalt-Iron Oxide, Alloy and Nitride: Synthesis, Characterization and Application in Catalytic Peroxymonosulfate Activation for Orange II Degradation*, Catalysts **7**, 138 (2017).

[45] V. Haueise, *Superconducting Spintronics with Magnetic Insulators*, Bachelor's thesis, Technische Universität München, München (2021).

[46] G. Terrasanta, M. Müller, T. Sommer, S. Geprägs, R. Gross, M. Althammer, and M. Poot, *Growth of Aluminum Nitride on a Silicon Nitride Substrate for Hybrid Photonic Circuits*, Materials for Quantum Technology **1**, 021002 (2021).

[47] T. Luschmann, *Coupling Strings, String Networks and Magnon-Phonon Interaction*, Master's thesis, Technische Universität München, München (2018).

[48] M. A. Mohammad, M. Muhammad, S. K. Dew, and M. Stepanova, in *Nanofabrication: Techniques and Principles*, edited by M. Stepanova and S. Dew (Springer, Vienna, 2012) pp. 11–41.

[49] C. Bayer, S. O. Demokritov, and B. Hillebrands, *Spin-Wave Wells with Multiple States Created in Small Magnetic Elements*, .

[50] Z. Duan, I. N. Krivorotov, R. E. Arias, N. Reckers, S. Stienen, and J. Lindner, *Spin Wave Eigenmodes in Transversely Magnetized Thin Film Ferromagnetic Wires*, Physical Review B **92**, 104424 (2015).

[51] G. Woltersdorf, *Spin-Pumping and Two-Magnon Scattering in Magnetic Multilayers*, Master's thesis, Martin-Luther-Universität Halle-Wittenberg (2004).

[52] A. V. Chumak, *Fundamentals of Magnon-Based Computing*, .

[53] P. Schwenke, *Schnelles Thermisches Tempern von Pt/Y3Fe5O12 Heterostrukturen*, Bachelor's thesis, Technische Universität München, München (2019).

[54] C. Liu, J. Chen, T. Liu, F. Heimbach, H. Yu, Y. Xiao, J. Hu, M. Liu, H. Chang, T. Stueckler, S. Tu, Y. Zhang, Y. Zhang, P. Gao, Z. Liao, D. Yu, K. Xia, N. Lei, W. Zhao, and M. Wu, *Long-Distance Propagation of Short-Wavelength Spin Waves*, Nature Communications **9**, 738 (2018).

[55] Y. Rao, D. Zhang, L. Jin, Z. Zhong, Q. Yang, M. Li, J. Li, Y. Yang, G. Wang, G. Gan, and H. Zhang, *Antenna Design for Ferromagnetic Resonance and Spin Wave Spectroscopy*, Journal of Magnetism and Magnetic Materials **490**, 165442 (2019).

[56] S. R. Lake, B. Divinskiy, G. Schmidt, S. O. Demokritov, and V. E. Demidov, *Efficient Geometrical Control of Spin Waves in Microscopic YIG Waveguides*, Applied Physics Letters **119**, 182401 (2021).

[57] H. Yu, O. d'Allivy Kelly, V. Cros, R. Bernard, P. Bortolotti, A. Anane, F. Brandl, R. Huber, I. Stasinopoulos, and D. Grundler, *Magnetic Thin-Film Insulator with Ultra-Low Spin Wave Damping for Coherent Nanomagnonics*, Scientific Reports **4**, 6848 (2014).

[58] M. Nakayama, K. Yamanoi, S. Kasai, S. Mitani, and T. Manago, *Thickness Dependence of Spin Wave Nonreciprocity in Permalloy Film*, Japanese Journal of Applied Physics **54**, 083002 (2015).

[59] M. Bailleul, D. Olligs, and C. Fermon, *Propagating Spin Wave Spectroscopy in a Permalloy Film: A Quantitative Analysis*, Applied Physics Letters **83**, 972 (2003).

[60] K. Baumgaertl and D. Grundler, *Reversal of Nanomagnets by Propagating Magnons in Ferrimagnetic Yttrium Iron Garnet Enabling Nonvolatile Magnon Memory* (2022), arXiv:2208.10923 .

[61] L. Flacke, *Spin-Pumping and Spin Wave Damping in Co25Fe75 Thin-Film Heterostructures*, Master's thesis, Technische Universität München (2018).

[62] K.-W. Nielsen, *Ursache Der Magnetischen Kopplung in Kobalt-dotiertem ZnO*, Ph.D. thesis, Technische Universität München, München (2007).

[63] W. L. Bragg, *The Diffraction of Short Electromagnetic Waves by a Crystal*, Scientia **23**, 153 (1929).

[64] F. M. Schade, *Fabrication and Characterization of Y3Fe5O12/Pt/Y3Fe5O12 Trilayers for Spin Current Based Experiments*, Bachelor's thesis, Technische Universität München, München (2013).

Acknowledgements/Danksagungen

Im Folgenden möchte ich einigen Personen danken, ohne die diese Arbeit nicht möglich gewesen wäre:

- **Prof. Dr. Rudolf Gross** für die Möglichkeit am WMI meine Masterarbeit schreiben zu dürfen.
- **Monika Scheufele** für die viele Zeit die du in meine Betreuung investiert hast. Für deine unfassbare Ausdauer, Geduld, Aufmerksamkeit, Expertise, Frustrationstoleranz, Genauigkeit und Zuversicht, die du während meiner Zeit bewiesen hast.
- **Dr. Stephan Geprägs** für den guten Rat, wenn es mal nicht weiter ging, die neuen Ideen, die viele Mühe bei der Korrektur und Zeit die du aller Umstände zum Trotz immer für mich gefunden hast.
- **Manuel Müller** für die fortwährende experimentelle Unterstützung. Ohne deine Expertise wären viele Messungen nicht möglich gewesen.
- **Johannes Weber** für die Anfertigung von zahlreichen Layouts sowie Durchführung und Auswertung von AFM Messungen.
- **Vincent Haueise** für die Unterstützung bei der Durchführung und Auswertung von FMR Messungen.
- Vielen Dank auch an meine Masterkollegen. Danke für die vielen gemeinsamen Mittagessen Franz, für die gute Stimmung Julian, für die angenehme Arbeitsatmosphäre Alex und Lukas und dass du mich ausgehalten hast Maria.